

Simultaneous Measurement of Oscillation Parameters in Beam and Atmospheric Neutrino Data from Tokai-to-Kamioka and Super-Kamiokande Experiments

Daniel Robert Clement Barrow

Magdalen College, Oxford University

¹⁰ A Dissertation Submitted to Oxford University

¹¹ for the Degree of Doctor of Philosophy

¹²

13 **Simultaneous Measurement of**

14 **Oscillation Parameters in Beam and**

15 **Atmospheric Neutrino Data from**

16 **Tokai-to-Kamioka and**

17 **Super-Kamiokande Experiments**

18 *Abstract*

19 Lorem ipsum dolor sit amet, consectetur adipiscing elit, sed do eiusmod tempor incididunt ut labore et dolore magna aliqua. Nulla aliquet porttitor lacus luctus accumsan tortor posuere. Pulvinar neque laoreet suspendisse interdum. Sem viverra aliquet eget sit. Nunc sed velit dignissim sodales ut eu sem integer vitae. At erat pellentesque adipiscing commodo elit at imperdiet dui accumsan. Fames ac turpis egestas integer eget aliquet nibh. Scelerisque eu ultrices vitae auctor eu augue. Purus non enim praesent elementum facilisis leo vel. Sollicitudin nibh sit amet commodo. Vitae auctor eu augue ut. Vel quam elementum pulvinar etiam. A condimentum vitae sapien pellentesque habitant morbi tristique senectus. Viverra accumsan in nisl nisi scelerisque eu ultrices. Sed viverra ipsum nunc aliquet bibendum enim. Sit amet purus gravida quis. In vitae turpis massa

³² sed elementum tempus egestas sed sed. Vivamus arcu felis bibendum
³³ ut tristique et egestas. Senectus et netus et malesuada fames ac turpis.
³⁴ Ac auctor augue mauris augue.

35 Declaration

36 This dissertation is the result of my own work, except where ex-
37 plicit reference is made to the work of others, and has not been sub-
38 mitted for another qualification to this or any other university. This
39 dissertation does not exceed the word limit for the respective Degree
40 Committee.

41 Daniel Robert Clement Barrow

42 ©The copyright of this thesis rests with the author and is made available under a Creative
43 Commons Attribution Non-Commercial No Derivatives licence. Researchers are free to copy,
44 distribute or transmit the thesis on the condition that they attribute it, that they do not use
45 it for commercial purposes and that they do not alter, transform or build upon it. For any
46 reuse or redistribution, researchers must make clear to others the licence terms of this work.

47

Acknowledgements

48 at pretium nibh ipsum. Eget nunc scelerisque viverra mauris in aliquam. Arcu vitae
49 elementum curabitur vitae nunc sed velit dignissim. Sed arcu non odio euismod lacinia
50 at quis risus sed. Vitae tempus quam pellentesque nec nam aliquam sem et tortor.
51 Viverra aliquet eget sit amet tellus cras adipiscing. Purus sit amet luctus venenatis
52 lectus magna. In aliquam sem fringilla ut morbi tincidunt augue. Fermentum dui
53 faucibus in ornare. Aliquam malesuada bibendum arcu vitae elementum curabitur
54 vitae nunc sed.

55 Ultricies leo integer malesuada nunc vel risus commodo. Tellus cras adipiscing
56 enim eu turpis egestas pretium. Dictumst quisque sagittis purus sit amet volutpat
57 consequat mauris nunc. Vitae congue mauris rhoncus aenean vel elit scelerisque
58 mauris pellentesque. Vel facilisis volutpat est velit egestas dui id ornare. Suscipit
59 adipiscing bibendum est ultricies. At in tellus integer feugiat scelerisque varius
60 morbi enim. Cras semper auctor neque vitae tempus. Commodo sed egestas egestas
61 fringilla phasellus faucibus. Cras pulvinar mattis nunc sed blandit. Pretium viverra
62 suspendisse potenti nullam ac tortor vitae. Purus sit amet volutpat consequat. Orci
63 sagittis eu volutpat odio facilisis mauris. Sit amet massa vitae tortor condimentum
64 lacinia quis. Commodo sed egestas egestas fringilla phasellus. Sed libero enim sed
65 faucibus turpis. Vitae tempus quam pellentesque nec.

66 Blandit massa enim nec dui. Viverra tellus in hac habitasse platea dictumst vestibulu-
67 lum. Bibendum enim facilisis gravida neque convallis. Sagittis nisl rhoncus mattis
68 rhoncus urna neque. Nisl rhoncus mattis rhoncus urna neque. Ac tortor vitae purus
69 faucibus ornare. Aenean sed adipiscing diam donec adipiscing tristique risus. Sapien
70 nec sagittis aliquam malesuada bibendum. Et leo duis ut diam quam nulla. Tellus
71 rutrum tellus pellentesque eu tincidunt tortor aliquam nulla facilisi. Fermentum leo

⁷² vel orci porta non pulvinar neque. Eget sit amet tellus cras adipiscing enim eu. Sed
⁷³ viverra tellus in hac habitasse platea dictumst vestibulum.

⁷⁴ Sit amet consectetur adipiscing elit. At varius vel pharetra vel turpis nunc eget
⁷⁵ lorem. Elit scelerisque mauris pellentesque pulvinar pellentesque habitant morbi
⁷⁶ tristique senectus. Odio euismod lacinia at quis risus sed vulputate odio. Vitae suscipit
⁷⁷ tellus mauris a diam maecenas sed enim ut. Dignissim convallis aenean et tortor at
⁷⁸ risus viverra. Diam sollicitudin tempor id eu. Erat velit scelerisque in dictum. Blandit
⁷⁹ cursus risus at ultrices. Ac tortor vitae purus faucibus ornare suspendisse sed.

Contents

81	1 Neutrino Oscillation Physics	1
82	1.1 Discovery of Neutrinos	1
83	1.2 Theory of Neutrino Oscillation	3
84	1.2.1 Three Flavour Oscillations	3
85	1.2.2 The MSW Effect	7
86	1.3 Neutrino Oscillation Measurements	8
87	1.3.1 Solar Neutrinos	9
88	1.3.2 Atmospheric Neutrinos	11
89	1.3.3 Accelerator Neutrinos	14
90	1.3.4 Reactor Neutrinos	17
91	2 T2K and SK Experiment Overview	20
92	2.1 The Super-Kamiokande Experiment	20
93	2.1.1 The SK Detector	21
94	2.1.2 Calibration	25
95	2.1.3 Data Acquisition and Triggering	28
96	2.1.4 Cherenkov Radiation	30
97	2.2 The Tokai to Kamioka Experiment	32
98	2.2.1 The Neutrino Beam	34
99	2.2.2 The Near Detector at 280m	37
100	2.2.2.1 Fine Grained Detectors	40
101	2.2.2.2 Time Projection Chambers	41
102	2.2.2.3 π^0 Detector	43
103	2.2.2.4 Electromagnetic Calorimeter	43
104	2.2.2.5 Side Muon Range Detector	45

105	2.2.3 The Interactive Neutrino GRID	45
106	3 Bayesian Statistics and Markov Chain Monte Carlo Techniques	47
107	3.1 Bayesian Statistics	48
108	3.2 Monte Carlo Simulation	49
109	3.2.1 Markov Chain Monte Carlo	51
110	3.2.2 Metropolis-Hastings Algorithm	54
111	3.2.3 MCMC Optimisation	55
112	3.3 Understanding the MCMC Results	59
113	3.3.1 Marginalisation	59
114	3.3.2 Parameter Estimation and Credible Intervals	60
115	3.3.3 Application of Bayes' Theorem	62
116	3.3.4 Comparison of MCMC Output to Expectation	63
117	4 Simulation, Reconstruction and Event Selections	65
118	4.1 Simulation	65
119	4.2 Event Reconstruction at SK	70
120	4.3 Event Selection at SK	80
121	5 Oscillation Probability Calculation	85
122	5.1 Overview	86
123	5.2 Treatment of Fast Oscillations	93
124	5.3 Calculation Engine	102
125	5.4 Matter Density Profile	103
126	5.5 Production Height Averaging	110
127	Bibliography	114
128	List of Figures	125

129 List of Tables**133**

¹³¹ **Chapter 1**

¹³² **Neutrino Oscillation Physics**

¹³³ When first proposed, neutrinos were expected to be massless fermions that only in-
¹³⁴ teract through weak and gravitational forces. This meant they were very difficult to
¹³⁵ detect as they can pass through significant amounts of matter without interacting. De-
¹³⁶ spite this, experimental neutrino physics has developed with many different detection
¹³⁷ techniques and neutrino sources being used today. In direct tension with the standard
¹³⁸ model physics, neutrinos have been determined to oscillate between different lepton
¹³⁹ flavours requiring them to have mass.

¹⁴⁰ section 1.1 describes the observation techniques and discovery of neutrinos. The
¹⁴¹ theory underpinning neutrino oscillation is described in section 1.2. This section
¹⁴² includes the approximations which can be made to simplify the understanding of
¹⁴³ neutrino oscillation in a two-flavour approximation as well as how the medium
¹⁴⁴ in which neutrinos propagate can manipulate the oscillation probability. The past,
¹⁴⁵ current, and future neutrino experiments are detailed in section 1.3 including the
¹⁴⁶ reactor, atmospheric, and long-baseline accelerator neutrino sources that have been
¹⁴⁷ used to successfully constrain oscillation parameter determination.

¹⁴⁸ **1.1 Discovery of Neutrinos**

¹⁴⁹ At the start of the 20th century, the electrons emitted from the β -decay of the nucleus
¹⁵⁰ were found to have a continuous energy spectrum [1,2]. This observation seemingly
¹⁵¹ broke the energy conservation invoked within that period's nuclear models. Postulated

in 1930 by Pauli as the solution to this problem, the neutrino (originally termed “neutron”) was theorized to be an electrically neutral spin-1/2 fermion with a mass of the same order of magnitude as the electron [3]. This neutrino was to be emitted with the electron in β -decay to alleviate the apparent breaking of energy conservation. As a predecessor of the weak interaction model, Fermi’s theory of β -decay developed the understanding by coupling the four constituent particles; electron, proton, neutron, and neutrino, into a consistent model [4].

Whilst Pauli was not convinced of the ability to detect neutrinos. The first observations of the particle were made in the mid-1950s when neutrinos from a reactor were observed via the inverse β -decay (IBD) process, $\bar{\nu}_e + p \rightarrow n + e^+$ [5, 6]. The detector consisted of two parts; a neutrino interaction medium and a liquid scintillator. The interaction medium was built from two water tanks. These were loaded with cadmium chloride to allow increased efficiency of neutron capture. The positron emitted from IBD annihilates, $e^+ + e^- \rightarrow 2\gamma$, generating a prompt signal and the neutron is captured on the cadmium via $n + {}^{108}Cd \rightarrow {}^{109}Cd \rightarrow {}^{109}Cd + \gamma$, producing a delayed signal. The experiment observed an increase in the neutrino event rate when the reactor was operating compared to when it was switched off, in much the same way as modern reactor neutrino experiments operate.

After the discovery of the ν_e , the natural question of how many flavours of neutrino exist was asked. In 1962, a measurement of the ν_μ was conducted at the Brookhaven National Laboratory [7]. A proton beam was directed at a beryllium target, generating a π -dominated beam which then decayed via $\pi^\pm \rightarrow \mu^\pm + (\nu_\mu, \bar{\nu}_\mu)$, and the subsequent interactions of the ν_μ were observed. The final observation to be made was that of the ν_τ from the DONUT experiment [8]. Three neutrinos seem the obvious solution as it mirrors the known number of charged lepton (as they form weak isospin doublets) but there could be evidence of more. Several neutrino experiments have found anomalous

₁₇₈ results [9, 10] which could be attributed to sterile neutrinos however cosmological
₁₇₉ observations indicate the number of neutrino species $N_{eff} = 3.15 \pm 0.23$ [11].

₁₈₀ 1.2 Theory of Neutrino Oscillation

₁₈₁ As direct evidence of beyond Standard Model physics, a neutrino generated with
₁₈₂ lepton flavour α can change into a different lepton flavour β after propagating some
₁₈₃ distance. This phenomenon is called neutrino oscillation and requires that neutrinos
₁₈₄ must have a non-zero mass (as seen in subsection 1.2.1). This is direct evidence
₁₈₅ of beyond standard model physics. This behaviour has been characterised by the
₁₈₆ Pontecorvo-Maki-Nakagawa-Sakata (PMNS) [12–14] mixing matrix which describes
₁₈₇ how the flavour and mass of neutrinos are associated. This is analogous to the Cabibbo-
₁₈₈ Kobayashi-Maskawa (CKM) [15] matrix measured in quark physics.

₁₈₉ 1.2.1 Three Flavour Oscillations

₁₉₀ The PMNS parameterisation defines three flavour eigenstates, ν_e , ν_μ and ν_τ (indexed
₁₉₁ ν_α), which are assigned based upon the weak interaction flavour states and three mass
₁₉₂ eigenstates, ν_1 , ν_2 and ν_3 (indexed ν_i). Each mass eigenstate is the superposition of all
₁₉₃ three flavour states,

$$|\nu_i\rangle = \sum_\alpha U_{\alpha i} |\nu_\alpha\rangle. \quad (1.1)$$

₁₉₄ U is the PMNS matrix which correlates the mass and flavour eigenstates. Neutrinos
₁₉₅ interact with leptons of the same weak flavour eigenstate rather than mass eigenstate.

¹⁹⁶ The propagation of a neutrino flavour eigenstate, in a vacuum, can be re-written as a
¹⁹⁷ plane-wave solution to the time-dependent Schrödinger equation,

$$|\nu_\alpha(t)\rangle = \sum_i U_{\alpha i}^* |\nu_i\rangle e^{-i\phi_i}. \quad (1.2)$$

¹⁹⁸ The probability of observing a neutrino of flavour eigenstate β from one which
¹⁹⁹ originated as flavour α can be calculated as,

$$P(\nu_\alpha \rightarrow \nu_\beta) = |\langle \nu_\beta | \nu_\alpha(t) \rangle|^2 = \sum_{i,j} U_{\alpha i}^* U_{\beta i} U_{\alpha j} U_{\beta j}^* e^{-i(\phi_j - \phi_i)} \quad (1.3)$$

²⁰⁰ The ϕ_i term can be expressed in terms of the energy, E_i , and magnitude of the
²⁰¹ three momenta, p_i , of the neutrino, $\phi_i = E_i t - p_i x$ (t and x being time and position
²⁰² coordinates). Therefore,

$$\phi_j - \phi_i = E_j t - E_i t - p_j x + p_i x. \quad (1.4)$$

²⁰³ For a relativistic particle, $E_i \gg m_i$,

$$p_i = \sqrt{E_i^2 - m_i^2} \approx E_i - \frac{m_i^2}{2E_i}. \quad (1.5)$$

²⁰⁴ Making the approximations that neutrinos are relativistic, the mass eigenstates
²⁰⁵ were created with the same energy and that $x = L$, where L is the distance traveled by
²⁰⁶ the neutrino, Equation 1.4 then becomes

$$\phi_j - \phi_i = \frac{\Delta m_{ij}^2 L}{2E}, \quad (1.6)$$

²⁰⁷ where $\Delta m_{ij}^2 = m_i^2 - m_j^2$. This, teamed with further use of unitarity relations results
²⁰⁸ in Equation 1.3 becoming

$$P(\nu_\alpha \rightarrow \nu_\beta) = \delta_{\alpha\beta} - 4 \sum_{i>j} \Re \left(U_{\alpha i}^* U_{\beta i} U_{\alpha j} U_{\beta j}^* \right) \sin^2 \left(\frac{\Delta m_{ij}^2 L}{4E} \right) + (-) 2 \sum_{i>j} \Im \left(U_{\alpha i}^* U_{\beta i} U_{\alpha j} U_{\beta j}^* \right) \sin \left(\frac{\Delta m_{ij}^2 L}{2E} \right). \quad (1.7)$$

²⁰⁹ Where $\delta_{\alpha\beta}$ is the Kronecker delta function and the negative sign is included for the
²¹⁰ oscillation probability of antineutrinos.

²¹¹ Typically, the PMNS matrix is parameterised into three mixing angles, a charge
²¹² parity (CP) violating phase δ_{CP} , and two Majorana phases $\alpha_{1,2}$,

$$U = \underbrace{\begin{pmatrix} 1 & 0 & 0 \\ 0 & c_{23} & s_{23} \\ 0 & -s_{23} & c_{23} \end{pmatrix}}_{\text{Atmospheric, Accelerator}} \underbrace{\begin{pmatrix} c_{13} & 0 & s_{13}e^{-i\delta_{CP}} \\ 0 & 1 & 0 \\ -s_{13}e^{-i\delta_{CP}} & 0 & c_{13} \end{pmatrix}}_{\text{Reactor, Accelerator}} \underbrace{\begin{pmatrix} c_{12} & s_{12} & 0 \\ -s_{12} & c_{12} & 0 \\ 0 & 0 & 1 \end{pmatrix}}_{\text{Reactor, Solar}} \underbrace{\begin{pmatrix} e^{i\alpha_1/2} & 0 & 0 \\ 0 & e^{i\alpha_2/2} & 0 \\ 0 & 0 & 1 \end{pmatrix}}_{\text{Majorana}}. \quad (1.8)$$

213 Where $s_{ij} = \sin(\theta_{ij})$ and $c_{ij} = \cos(\theta_{ij})$. The oscillation parameters are often
214 grouped; (1, 2) as “solar”, (2, 3) as “atmospheric” and (1, 3) as “reactor”. Many
215 neutrino experiments aim to measure the PMNS parameters from a wide array of
216 origins, as is the purpose of this thesis.

217 The Majorana phase, $\alpha_{1,2}$, containing matrix included within Equation 1.8 is only
218 included for completeness. For an oscillation analysis experiment, any term in this
219 oscillation probability calculation containing this phase disappears due to taking the
220 expectation value of the PMNS matrix.

221 A two flavour approximation can be attained when one assumes the third mass
222 eigenstate is degenerate with another. As discussed in section 1.3, it is found that
223 $\Delta m_{21}^2 \ll |\Delta m_{31}^2|$. This results in the two flavour approximation being reasonable for
224 understanding the features of the oscillation. In this two flavour case, the mixing
225 matrix becomes,

$$U_{2\text{ Flav.}} = \begin{pmatrix} \cos(\theta) & \sin(\theta) \\ -\sin(\theta) & \cos(\theta) \end{pmatrix}. \quad (1.9)$$

226 This culminates in the oscillation probability,

$$\begin{aligned} P(\nu_\alpha \rightarrow \nu_\alpha) &= 1 - \sin^2(2\theta) \sin^2\left(\frac{\Delta m^2 L}{4E}\right), \\ P(\nu_\alpha \rightarrow \nu_\beta) &= \sin^2(2\theta) \sin^2\left(\frac{\Delta m^2 L}{4E}\right). \end{aligned} \quad (1.10)$$

227 For $\alpha \neq \beta$. For a fixed neutrino energy, the oscillation probability is a sinusoidal
228 function depending upon the distance over which the neutrino propagates. The

229 frequency and amplitude of oscillation are dependent upon the ratio of the $\Delta m^2 / 4E$
230 and $\sin^2 2\theta$, respectively. For more human-readable units, the maximum oscillation
231 probability for a fixed value of θ is given at $L[km] / E[GeV] \sim 1.27 / \Delta m^2$. It is this
232 calculation that determines the best L/E value for a given experiment to be designed
233 around for measurements of a specific value of Δm^2 .

234 1.2.2 The MSW Effect

235 The theory of neutrino oscillation in a vacuum is described in subsection 1.2.1. How-
236 ever, the beam neutrinos and atmospheric neutrinos originating from below the
237 horizon propagate through matter in the Earth. The coherent scattering of neutrinos
238 from a material target modifies the hamiltonian of the system. This results in a change
239 in the oscillation probability. Notably, charged current scattering ($\nu_e + e^- \rightarrow \nu_e + e^-$,
240 propagated by a W boson) only affects electron neutrinos compared to the neutral
241 current scattering ($\nu_l + l^- \rightarrow \nu_l + l^-$, propagated by a Z^0 boson), interacts through
242 all neutrino flavours equally. In the two-flavour limit, the effective mixing parameter
243 becomes

$$\sin^2(2\theta) \rightarrow \sin^2(2\theta_m) = \frac{\sin^2(2\theta)}{(A/\Delta m^2 - \cos(2\theta))^2 + \sin^2(2\theta)}, \quad (1.11)$$

244 where $A = 2\sqrt{2}G_F N_e E$ with N_e is the electron density of the medium and G_F is
245 Fermi's constant. It is clear to see that there exists a value of $A = \Delta m^2 \cos(2\theta)$ for
246 $\Delta m^2 > 0$ which results in a divergent mixing parameter. This resonance is due to
247 the Mikheyev-Smirnov-Wolfenstein (MSW) effect (or more colloquially, the matter
248 resonance) which regenerates the electron neutrino component of the neutrino flux
249 [16–18]. The density at which the resonance occurs is given by

$$N_e = \frac{\Delta m^2 \cos(2\theta)}{2\sqrt{2}G_F E}. \quad (1.12)$$

250 At densities lower than this critical value, the oscillation probability will be much
251 closer to that of vacuum oscillation. The resonance occurring from the MSW effect
252 depends on the sign of Δm^2 . Therefore, any neutrino oscillation experiment which
253 observes neutrinos and antineutrinos which have propagated through matter can have
254 some sensitivity to the ordering of the neutrino mass eigenstates.

255 1.3 Neutrino Oscillation Measurements

256 As evidence of beyond standard model physics, the 2015 Nobel Prize in Physics was
257 awarded to the Super-Kamiokande (SK) [19] and Sudbury Neutrino Observatory
258 (SNO) [20] collaborations for the first definitive observation of solar and atmospheric
259 neutrino oscillation [21]. Since then, the field has seen a wide array of oscillation
260 measurements from a variety of neutrino sources. As seen in subsection 1.2.1, the
261 neutrino oscillation probability is dependent on the ratio of the propagation baseline, L ,
262 to the neutrino energy, E . It is this ratio that determines the type of neutrino oscillation
263 a particular experiment is sensitive to.

264 As illustrated in Figure 1.1, there are many neutrino sources that span a wide
265 range of energies. The least energetic neutrinos are from diffuse supernovae and
266 terrestrial neutrinos at $O(1)\text{MeV}$ whereas the most energetic neutrinos originate from
267 atmospheric and galactic neutrinos of $> O(1)\text{TeV}$.

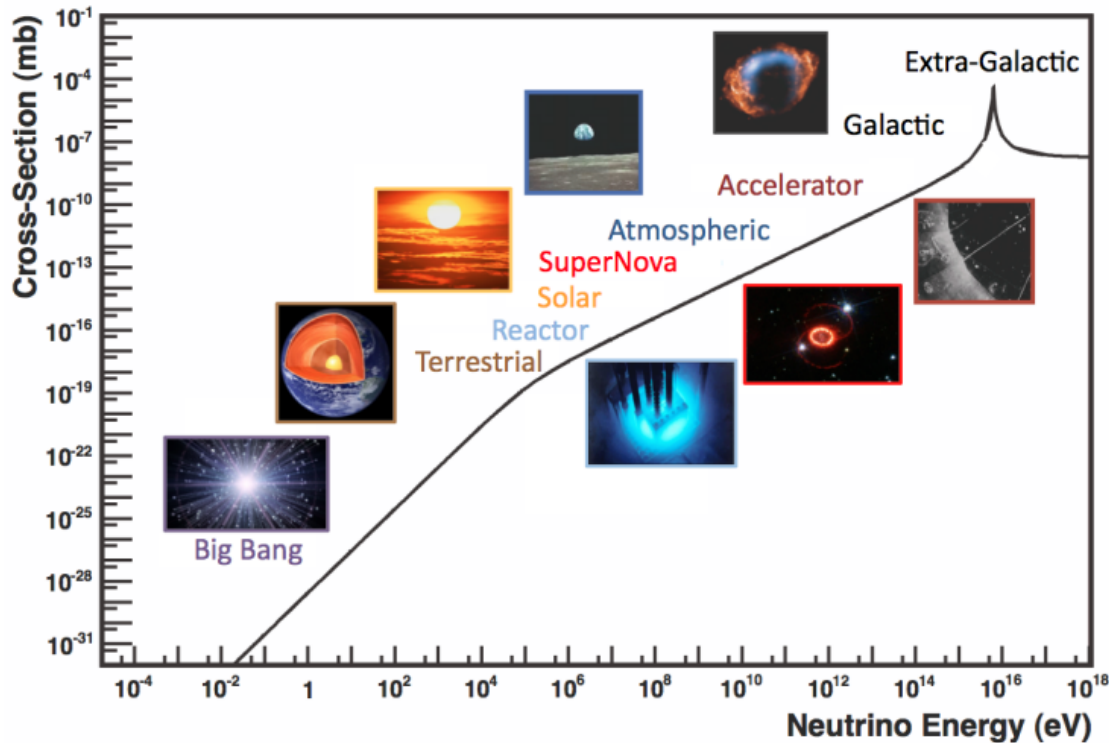


Figure 1.1: The cross-section of neutrinos from various natural and man-made sources as a function of neutrino energy. Taken from [22]

268 1.3.1 Solar Neutrinos

269 Solar neutrinos are emitted from fusion reaction chains at the center of the Sun. The
 270 solar neutrino flux, given as a function of neutrino energy for different fusion and
 271 decay chains is illustrated in Figure 1.2. Whilst proton-proton fusion generates the
 272 largest flux of neutrinos, the neutrinos are of low energy and are difficult to reconstruct
 273 due to the IBD interaction threshold of 1.8MeV. Consequently, most experiments focus
 274 on the neutrinos from the decay of 8B (via $^8B \rightarrow ^8Be^* + e^+ + \nu_e$), which are higher
 275 energy.

276 The first measurements of solar neutrinos observed a significant reduction in the
 277 event rate compared to predictions from the Standard Solar Model [24, 25]. The
 278 proposed solution to this “solar neutrino problem” was $\nu_e \leftrightarrow \nu_\mu$ oscillations in a

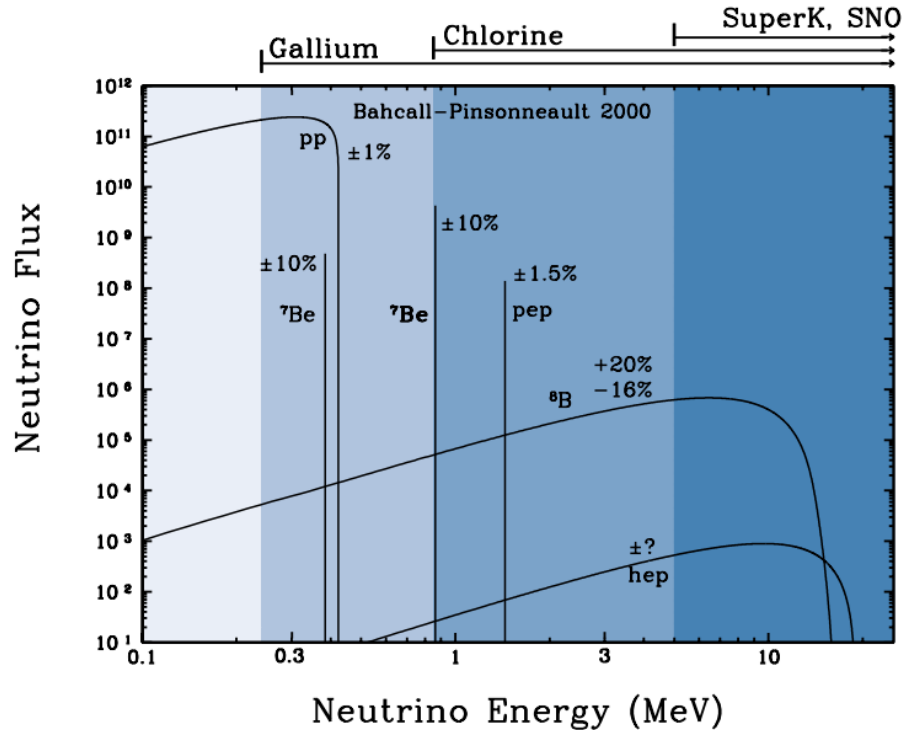


Figure 1.2: The solar neutrino flux as a function of neutrino energy for various fusion reactions and decay chains as predicted by the Standard Solar Model. Taken from [23].

²⁷⁹ precursory version of the PMNS model [26]. The Kamiokande [27], Gallex [28] and
²⁸⁰ Sage [29] experiments confirmed the ~ 0.5 factor deficit of solar neutrinos.

²⁸¹ The conclusive solution to this problem was determined by the SNO collabora-
²⁸² tion [30]. Using a deuterium water target to observe 8B neutrinos, the event rate of
²⁸³ charged current (CC), neutral current (NC), and elastic scattering (ES) interactions
²⁸⁴ (Given in Equation 1.13) was simultaneously measured. CC events can only occur for
²⁸⁵ electron neutrinos, whereas the other interaction channels are agnostic to neutrino
²⁸⁶ flavour (Although the ES reaction is more sensitive to electron neutrino interactions).
²⁸⁷ This meant that there were direct measurements of the ν_e and ν_x neutrino flux. It
²⁸⁸ was concluded that the CC and ES interaction rates were consistent with the deficit
²⁸⁹ previously observed. Most importantly, the NC reaction rate was only consistent with
²⁹⁰ the others under the hypothesis of flavour transformation.

$$\begin{aligned}
 \nu_e + d &\rightarrow p + p + e^- & (CC) \\
 \nu_x + d &\rightarrow p + n + \nu_x & (NC) \\
 \nu_x + e^- &\rightarrow \nu_x + e^- & (ES)
 \end{aligned} \tag{1.13}$$

291 Many experiments have since measured the neutrino flux of different interaction
 292 chains within the sun [31–33]. The most recent measurement was that of CNO neutrinos
 293 which were recently observed with 5σ significance by the Borexino collaboration.
 294 Future neutrino experiments aim to further these spectroscopic measurements of
 295 different fusion chains within the Sun [34–36]. Solar neutrinos act as an irreducible
 296 background for dark matter experiments like DARWIN but oscillation parameter
 297 measurements can be made [37].

298 1.3.2 Atmospheric Neutrinos

299 The interactions of primary cosmic ray protons in Earth’s upper atmosphere generate
 300 showers of energetic hadrons. These are mostly pions and kaons which when they
 301 decay produce a natural source of neutrinos spanning energies of MeV to TeV [38].
 302 This decay is via

$$\begin{aligned}
 \pi^\pm &\rightarrow \mu^\pm + (\nu_\mu, \bar{\nu}_\mu) \\
 \mu^\pm &\rightarrow e^\pm + (\nu_\mu, \bar{\nu}_\mu) + (\nu_e, \bar{\nu}_e)
 \end{aligned} \tag{1.14}$$

303 such that for a single pion decay, three neutrinos are produced. The atmospheric
 304 neutrino flux energy spectra as predicted by the Bartol [39], Honda [40–42], and
 305 FLUKA [43] models are illustrated in Figure 1.3. The flux distribution peaks at an

³⁰⁶ energy of $O(10)$ GeV. The uncertainties associated with these models are dominated
³⁰⁷ by the hadronic production of kaon and pions as well as the primary cosmic flux.

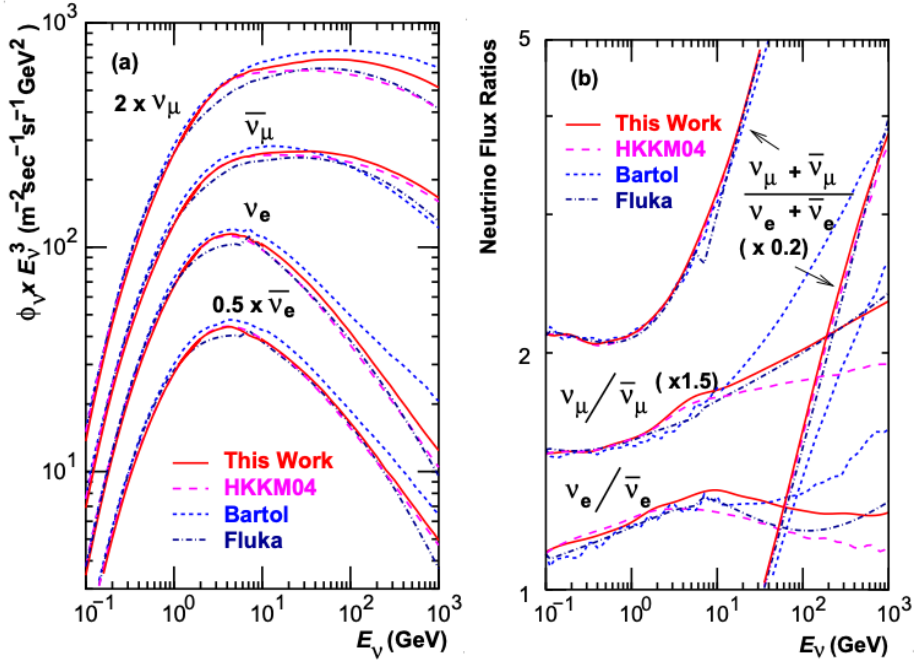


Figure 1.3: Left panel: The atmospheric neutrino flux for different neutrino flavours as a function of neutrino energy as predicted by the 2007 Honda model (“This work”) [40], the 2004 Honda model (“HKKM04”) [41], the Bartol model [39] and the FLUKA model [43]. Right panel: The ratio of the muon to electron neutrino flux as predicted by all the quoted models. Both figures taken from [40].

³⁰⁸ Unlike long-baseline experiments which have a fixed baseline, the distance at-
³⁰⁹ mospheric neutrinos propagate is dependent upon the zenith angle at which they
³¹⁰ interact. This is illustrated in Figure 1.4. Neutrinos that are generated directly above
³¹¹ the detector ($\cos(\theta) = 1.0$) have a baseline equivalent to the height of the atmosphere
³¹² whereas neutrinos that interact directly below the detector ($\cos(\theta) = -1.0$) have to
³¹³ travel a length equal to the diameter of the Earth. This means atmospheric neutrinos
³¹⁴ have a baseline that varies from $O(20)$ km to $O(6 \times 10^3)$ km. Any neutrino generated
³¹⁵ at or below the horizon will be subject to matter effects as they propagate through the
³¹⁶ Earth.

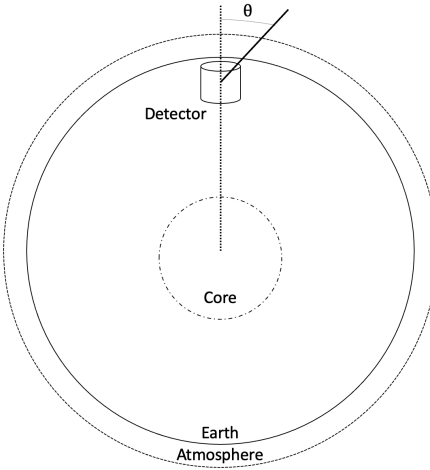


Figure 1.4: A diagram illustrating the definition of zenith angle as used in the Super Kamiokande experiment [44].

317 Figure 1.5 highlights the neutrino flux as a function of the zenith angle for different

318 slices of neutrino energy. For medium to high-energy neutrinos (and to a lesser degree

319 for low-energy neutrinos), the flux is approximately symmetric around $\cos(\theta) = 0$.

320 To the accuracy of this approximation, the systematic uncertainties associated with

321 atmospheric flux for comparing upward-going and down-going neutrino cancels. This

322 allows the down-going events, which are mostly insensitive to oscillation probabilities,

323 to act as an unoscillated prediction (similar to a near detector in an accelerator neutrino

324 experiment).

325 Precursory hints of atmospheric neutrinos were observed in the mid-1960s search-

326 ing for $\nu_\mu^{(-)} + X \rightarrow X^* + \mu^\pm$ [45]. This was succeeded with the IMB-3 [46] and

327 Kamiokande [47] experiments which measured the ratio of muon neutrinos com-

328 pared to electron neutrinos $R(\nu_\mu/\nu_e)$. Both experiments were found to have a con-

329 sistent deficit of muon neutrinos, with $R(\nu_\mu/\nu_e) = 0.67 \pm 0.17$ and $R(\nu_\mu/\nu_e) =$

330 $0.60^{+0.07}_{-0.06} \pm 0.05$. Super-Kamiokande (SK) [44] extended this analysis by fitting os-

331 cillation parameters in $P(\nu_\mu \rightarrow \nu_\tau)$ which found best fit parameters $\sin^2(2\theta) > 0.92$

332 and $1.5 \times 10^{-3} < \Delta m^2 < 3.4 \times 10^{-3} \text{ eV}^2$.

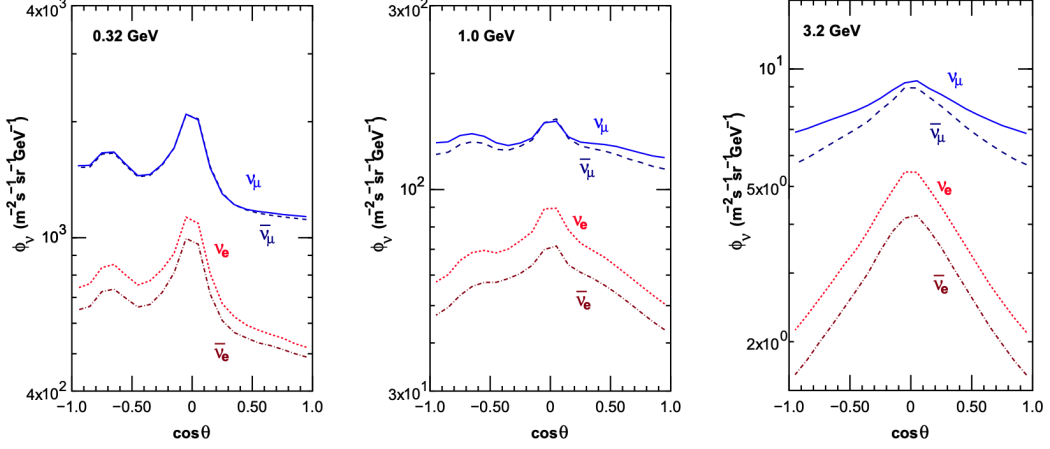


Figure 1.5: Prediction of $\nu_e, \bar{\nu}_e, \nu_\mu, \bar{\nu}_\mu$ fluxes as a function of zenith angle as calculated by the HKKM model [42]. The left, middle and right panels represent three values of neutrino energy, 0.32GeV, 1.0GeV and 3.2GeV respectively. Predictions for other models including Bartol [39], Honda [40] and FLUKA [43] are given in [44].

Since then, atmospheric neutrino experiments have been making precision measurements of the $\sin^2(\theta_{23})$ and Δm_{32}^2 oscillation parameters. Atmospheric neutrino oscillation is dominated by $P(\nu_\mu \rightarrow \nu_\tau)$, where SK observed a 4.6σ discovery of ν_τ appearance [48]. Figure 1.6 illustrates the current estimates on the atmospheric mixing parameters from a wide range of atmospheric and accelerator neutrino observatories.

1.3.3 Accelerator Neutrinos

The concept of using a man-made “neutrino beam” was first realised in 1962 [55]. Since then, many experiments have followed which all use the same fundamental concepts. Typically, a proton beam is aimed at a target producing charged mesons that decay to neutrinos. The mesons can be sign-selected by the use of magnetic focusing horns to generate a neutrino or antineutrino beam. Pions are the primary meson that decay and depending on the orientation of the magnetic field, a muon (anti-)neutrino beam is generated via $\pi^+ \rightarrow \mu^+ + \nu_\mu$ or $\pi^- \rightarrow \mu^- + \bar{\nu}_\mu$. The decay of muons and kaons does result in an irreducible intrinsic electron neutrino background. In T2K,

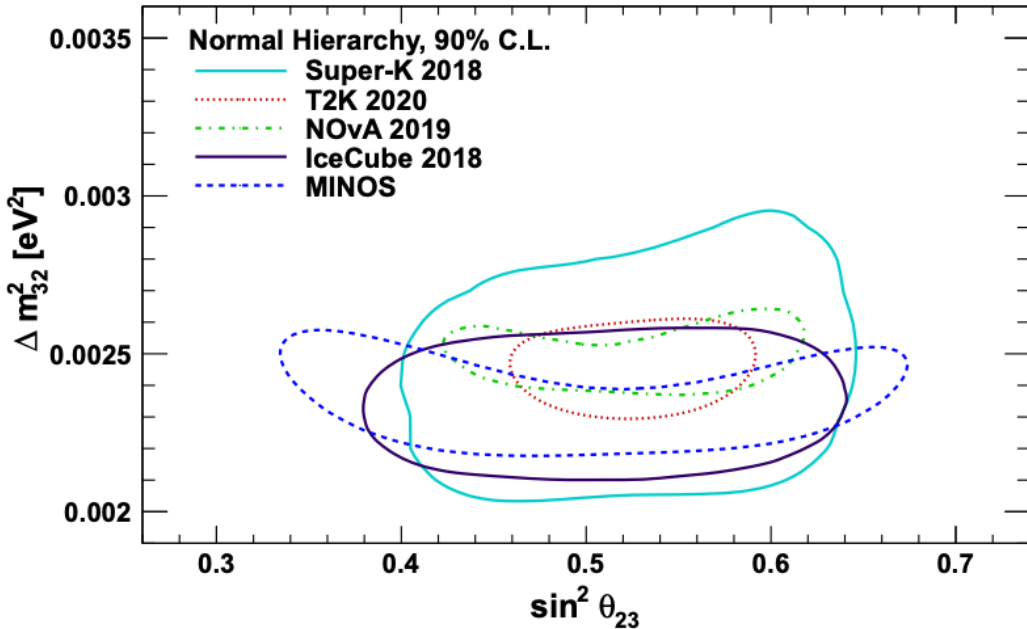


Figure 1.6: Constraints on the atmospheric oscillation parameters, $\sin^2(\theta_{23})$ and Δm_{23}^2 , from atmospheric and long baseline experiments: SK [49], T2K [50], NO ν A [51], IceCube [52] and MINOS [53]. Figure taken from [54].

347 this background contamination is $O(< 1\%)$ [56]. There is also an approximately $\sim 5\%$
 348 “wrong-sign” neutrino background of $\bar{\nu}_\mu$ generated via the same decays.

349 The energy of each neutrino in the beam is dependent on the energy of the initial
 350 proton beam. Therefore, tuning the proton energy allows the neutrino energy to be set
 351 to a value that maximises the disappearance oscillation probability in the L/E term in
 352 Equation 1.10. This means that accelerator experiments are typically more sensitive
 353 to the mixing parameters as compared to a natural neutrino source. However, the
 354 disadvantage compared to atmospheric neutrino experiments is that the baseline has
 355 to be shorter due to the lower flux. Consequently, there is typically less sensitivity to
 356 matter effects and the ordering of the neutrino mass eigenstates.

357 A neutrino experiment measures

$$R(\vec{x}) = \Phi(E_\nu) \times \sigma(E_\nu) \times \epsilon(\vec{x}) \times P(\nu_\alpha \rightarrow \nu_\beta), \quad (1.15)$$

358 where $R(\vec{x})$ is the event rate of neutrinos at position \vec{x} , $\Phi(E_\nu)$ is the flux of neutrinos
 359 with energy E_ν , $\sigma(E_\nu)$ is the cross-section of the neutrino interaction and $\epsilon(\vec{x})$ is the
 360 efficiency of the detector. In order to leverage the most out of an accelerator neutrino
 361 experiment, the flux and cross-section systematics need to be constrained. This is
 362 typically done via the use of a “near detector”, situated at a baseline of $O(1)$ km. This
 363 detector observes the unoscillated neutrino flux and constrains the parameters used
 364 within the flux and cross-section model.

365 The first accelerator experiments to precisely measure oscillation parameters were
 366 MINOS [57] and K2K [58]. These experiments confirmed the $\nu_\mu \rightarrow \nu_\mu$ oscillations seen
 367 in atmospheric neutrino experiments by finding consistent mixing parameter values
 368 for $\sin^2(\theta_{23})$ and Δm_{23}^2 . The current generation of accelerator neutrino experiments,
 369 T2K and NO ν A extended this field by observing $\bar{\nu}_\mu \rightarrow \bar{\nu}_e$ and lead the sensitivity
 370 to atmospheric mixing parameters as seen in Figure 1.6 [59]. The two experiments
 371 differ in their peak neutrino energy, baseline, and detection technique. The NO ν A
 372 experiment is situated at a baseline of 810km from the NuMI beamline which delivers
 373 2GeV neutrinos. The T2K neutrino beam is peaked around 0.6GeV and propagates
 374 295km. The NO ν A experiment also uses functionally identical detectors (near and far)
 375 which allow the approximate cancellation of detector systematics whereas T2K uses a
 376 plastic scintillator technique at the near detector and a water Cherenkov far detector.
 377 The future generation experiments DUNE [60] and Hyper-Kamiokande [61] will
 378 succeed these experiments as the high-precision era of neutrino oscillation parameter
 379 measurements develops.

Several anomalous results have been observed in the LSND [9] and MiniBooNE [10] detectors which were designed with purposefully short baselines. Parts of the neutrino community attributed these results to oscillations induced by a fourth “sterile” neutrino [62] but several searches in other experiments, MicroBooNE [63] and KARMEN [64], found no hints of additional neutrino species. The solution to the anomalous results are still being determined.

1.3.4 Reactor Neutrinos

As illustrated in the first discovery of neutrinos (section 1.1), nuclear reactors are a very useful man-made source of electron antineutrinos. For reactors that use low-enriched uranium ^{235}U as fuel, the antineutrino flux is dominated by the β -decay fission of ^{235}U , ^{238}U , ^{239}Pu and ^{241}Pu [65] as illustrated in Figure 1.7.

Due to their low energy, reactor electron antineutrinos predominantly interact via the inverse β -decay (IBD) interaction. The typical signature contains two signals delayed by $O(200)\mu\text{s}$; firstly the prompt photons from positron annihilation, and secondly the photons emitted ($E_{tot}^\gamma = 2.2\text{MeV}$) from de-excitation after neutron capture on hydrogen. Searching for both signals improves the detector’s ability to distinguish between background and signal events [67]. Recently, SK included gadolinium dopants into the ultra-pure water to increase the energy released from the photon cascade to $\sim 8\text{MeV}$ and reduce the time of the delayed signal to $\sim 28\mu\text{s}$.

There are many short baseline experiments ($L \sim O(1)\text{km}$) that have measured the $\sin^2(\theta_{13})$ and Δm_{23}^2 oscillation parameters. Daya Bay [68], RENO [69] and Double Chooz [70] have all provided precise measurements, with the first discovery of a non-zero θ_{13} made by Daya Bay and RENO (and complimented by T2K [70]). The constraints on $\sin^2(\theta_{13})$ by the reactor experiments lead the field and are often used as

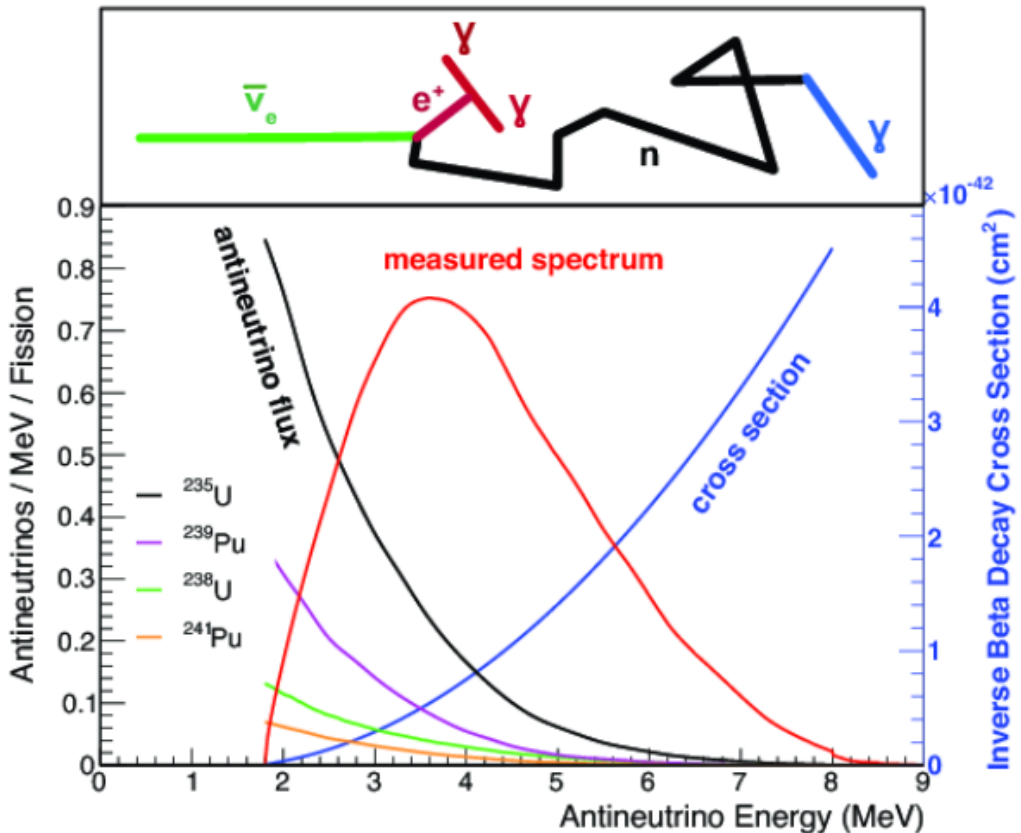


Figure 1.7: Reactor electron antineutrino fluxes for ^{235}U (Black), ^{238}U (Green), ^{239}Pu (Purple), and ^{241}Pu (Orange) isotopes. The inverse β -decay cross-section (Blue) and corresponding measurable neutrino spectrum (Red) are also given. Top panel: Schematic of Inverse β -decay interaction including the eventual capture of the emitted neutron. This capture emits a γ -ray which provides a second signal of the event. Taken from [66].

404 external inputs to accelerator neutrino experiments to improve their sensitivity to δ_{CP}
 405 and mass hierarchy determination. JUNO-TAO [71], a small collaboration within the
 406 larger JUNO experiment, is a next-generation reactor experiment that aims to precisely
 407 measure the isotopic antineutrino yields from the different fission chains. Alongside
 408 this, it aims to explain the ‘5MeV excess’ [72–74] by conducting a search for sterile
 409 neutrinos with a mass scale of around 1eV.

410 Kamlan [75] is the only experiment to have observed reactor neutrinos using a
 411 long baseline (flux weighted averaged baseline of $L \sim 180\text{km}$) which allows it to have
 412 sensitivity to Δm_{12}^2 . Combined with the SK solar neutrino experiment, the combined

⁴¹³ analysis puts the most stringent constraint on Δm_{12}^2 [76] which is used as a prior

⁴¹⁴ uncertainty within accelerator neutrino experiments.

⁴¹⁵ **Chapter 2**

⁴¹⁶ **T2K and SK Experiment Overview**

⁴¹⁷ As the successor of the Kamiokande experiment, the Super-Kamiokande (SK) collaboration has been leading atmospheric neutrino oscillation analyses for over two decades.
⁴¹⁹ The detector has provided some of the strongest constraints on proton decay limits
⁴²⁰ and as well as the first precise measurements of the Δm_{23}^2 and $\sin^2(\theta_{23})$ neutrino
⁴²¹ oscillation parameters. Despite this, the ability of the detector to low-energy neutrino
⁴²² events has been significantly improved with the recent gadolinium doping of the
⁴²³ ultra-pure water target. section 2.1 describes the history, detection technique, and
⁴²⁴ operation of the SK detector.

⁴²⁵ The Tokai-to-Kamioka (T2K) experiment was one of the first long-baseline experiments to use both neutrino and antineutrino beams to precisely measure the
⁴²⁷ charge parity violation within the neutrino sector. With the SK detector observing
⁴²⁸ the oscillated neutrino flux, the T2K experiment observed the first hints of a non-zero
⁴²⁹ $\sin^2(\theta_{13})$ measurement and continues to lead the field with the constraints it provides on $\sin^2(\theta_{13})$, $\sin^2(\theta_{23})$, Δm_{23}^2 and δ_{CP} . section 2.2 documents the techniques
⁴³¹ which T2K uses in generating its neutrino beam as well as the ‘near-detector’ used to
⁴³² constrain the flux and cross-section parameters invoked within the systematic models.

⁴³³ **2.1 The Super-Kamiokande Experiment**

⁴³⁴ The SK experiment began taking data in 1996 [77] and has had many modifications
⁴³⁵ throughout its lifespan. There have been seven defined periods of data taking as

436 noted in Table 2.1. Data taking began in SK-I which ran for five years. Between the
 437 SK-I and SK-II periods, a significant proportion of the PMTs were damaged during
 438 maintenance. Those that survived were equally distributed throughout the detector
 439 in the SK-II era, which resulted in a reduced photo-coverage. From SK-III onwards,
 440 repairs to the detector meant the full suite of PMTs was operational. Before the
 441 start of SK-IV, the data acquisition and electronic systems were upgraded. Between
 442 SK-IV and SK-V, a significant effort was placed into tank open maintenance and
 443 repair/replacement of defective PMTs, a task for which the author of this thesis was
 444 required. Consequently, the detector conditions were significantly different between
 445 the two operational periods. SK-VI saw the start of the 0.01% gadolinium doped
 446 water. SK-VII, which started during the writing of this thesis, has increased the
 447 gadolinium concentration to 0.03% for continued operation. [DB: Link to Linyan's talk from Nu2022.](#)
 448

Period	Start Date	End Date	Live-time (days)
I	April 1996	July 2001	1489.19
II	October 2002	October 2005	798.59
III	July 2006	September 2008	518.08
IV	September 2008	May 2018	3244.4
V	January 2019	July 2020	461.02
VI	July 2020	May 2022	583.3
VII	May 2022	Ongoing	N/A

Table 2.1: The various SK periods and respective live-time. The SK-VI live-time is calculated until 1st April 2022. SK-VII started during the writing of this thesis.

449 2.1.1 The SK Detector

450 The basic structure of the Super-Kamiokande (SK) detector is a cylindrical tank with a
 451 diameter 39.3m and height 41.1m filled with ultrapure water [78]. A diagram of the
 452 significant components of the SK detector is illustrated in Figure 2.1. The SK detector

453 is situated in the Kamioka mine in Gifu, Japan. The mine is underground with roughly
 454 1km rock overburden (2.7km water equivalent overburden) [79]. At this depth, the
 455 rate of cosmic ray muons is significantly decreased to a value of $\sim 2\text{Hz}$. The top of
 456 the tank is covered with stainless steel which is designed as a working platform for
 457 maintenance, calibration, and location for high voltage and data acquisition electronics.

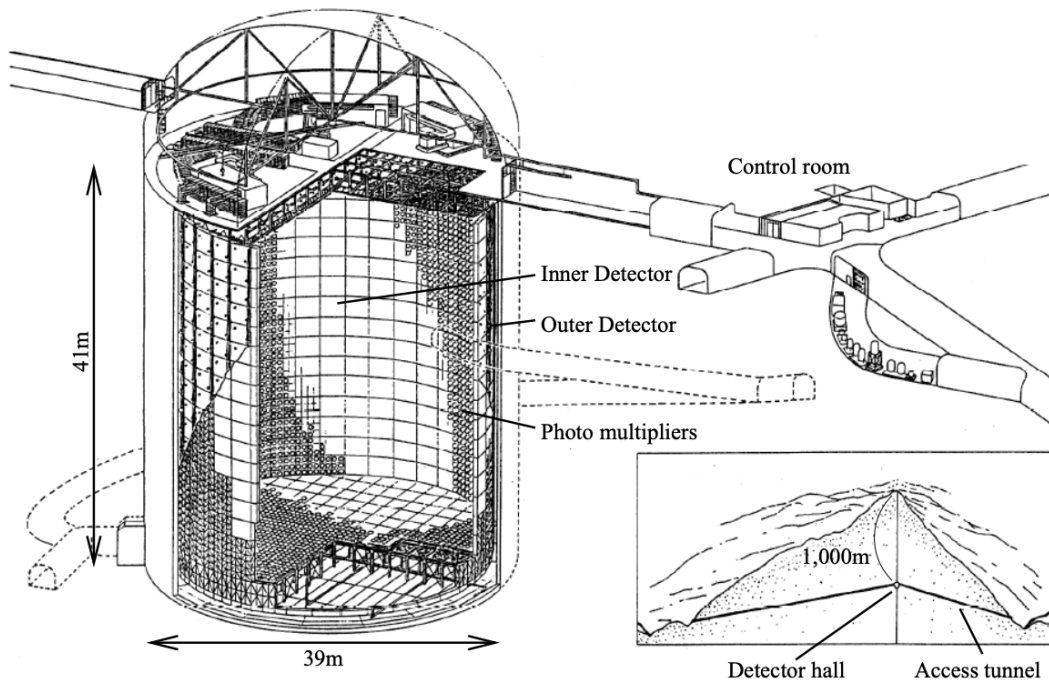


Figure 2.1: A schematic diagram of the Super-Kamiokande Detector. Taken from [80].

458 A smaller cylindrical structure (36.2m diameter, 33.8m height) is situated inside the
 459 tank, with an approximate 2m gap between this structure and the outer tank wall. The
 460 purpose of this structure is to support the photomultiplier tubes (PMTs). The volume
 461 inside and outside the support structure is referred to as the inner detector (ID) and
 462 outer detector (OD), respectively. In the SK-IV era, the ID and OD are instrumented
 463 by 11,129 50cm and 1,885 20cm PMTs respectively [78]. The ID contains a 32kton
 464 mass of water. Many analyses performed at SK use a “fiducial volume” defined by the
 465 volume of water inside the ID excluding some distance to the ID wall. This reduces the
 466 volume of the detector which is sensitive to neutrino events but reduces radioactive

⁴⁶⁷ backgrounds and allows for better reconstruction performance. The nominal fiducial
⁴⁶⁸ volume is defined as the area contained inside 2m from the ID wall for a total of
⁴⁶⁹ 22.5kton water [81].

⁴⁷⁰ The two regions of the detector (ID and OD) are optically separated with opaque
⁴⁷¹ black plastic. The purpose of this is to determine whether a track entered or exited
⁴⁷² the ID. This allows cosmic ray muons and partially contained events to be tagged and
⁴⁷³ separated from neutrino events entirely contained within the ID. This black plastic is
⁴⁷⁴ also used to cover the area between the ID PMTs to reduce photon reflection from the
⁴⁷⁵ ID walls. Opposite to this, the OD is lined with a reflective material to allow photons to
⁴⁷⁶ reflect around inside the OD until collected by one of the PMTs. Furthermore, each OD
⁴⁷⁷ PMT is backed with $50 \times 50\text{cm}$ plates of wavelength shifting acrylic which increases
⁴⁷⁸ the efficiency of light collection [79].

⁴⁷⁹ In the SK-IV data-taking period, the photocathode coverage of the detector, or the
⁴⁸⁰ fraction of the ID wall instrumented with PMTs, is $\sim 40\%$ [79]. The PMTs have a
⁴⁸¹ quantum efficiency (the ratio of detected electrons to incident photons) of $\sim 21\%$ for
⁴⁸² photons with wavelengths of $360\text{nm} < \lambda < 390\text{nm}$. The proportion of photoelectrons
⁴⁸³ that produce a signal in the dynode of a PMT, termed the collection efficiency, is
⁴⁸⁴ $> 70\%$ [79]. The PMTs used within SK are most sensitive to photons with wavelength
⁴⁸⁵ $300\text{nm} \leq \lambda \leq 600\text{nm}$ [79]. One disadvantage of using PMTs as the detection media
⁴⁸⁶ is that the Earth's geomagnetic field can modify its response. Therefore, a set of
⁴⁸⁷ compensation coils is built around the inner surface of the detector to mitigate this
⁴⁸⁸ effect [82].

⁴⁸⁹ As mentioned, the SK detector is filled with ultrapure water, which in a perfect
⁴⁹⁰ world would contain no impurities. However, bacteria and organic compounds can
⁴⁹¹ significantly degrade the water quality. This decreases the attenuation length which
⁴⁹² reduces the total number of photons that hit a PMT. To combat this, a sophisticated

493 water treatment system has been developed [79, 83]. UV lights, mechanical filters, and
494 membrane degasifiers are used to reduce the bacteria, suspended particulates, and
495 radioactive materials from the water. The flow of water within the tank is also critical
496 as it can remove stagnant bacterial growth or build-up of dust on the surfaces within
497 the tank. Gravity drifts impurities in the water towards the bottom of the tank which,
498 if left uncontrolled, can create asymmetric water conditions between the top and
499 bottom of the tank. Typically, the water entering the tank is cooled below the ambient
500 temperature of the tank to control convection and inhibit bacteria growth. Furthermore,
501 the dark noise hits within PMTs is sensitive to the PMT temperature [84] so controlling
502 the temperature gradients within the tank is beneficial for stable measurements.

503 SK-VI is the first phase of the SK experiment to use gadolinium dopants within
504 the ultrapure water [DB: Link to Linyan's talk at Nu2022](#). As such, the SK water
505 system had to be replaced to avoid removing the gadolinium concentrate from the
506 ultrapure water [85]. For an inverse β -decay (IBD) interaction in a water target, the
507 emitted neutron is thermally captured on hydrogen. This process releases 2.2MeV γ
508 rays which are difficult to detect due to Compton scattered electrons from a γ ray of
509 this energy is very close to the Cherenkov threshold, limiting the number of photons
510 produced. Thermal capture of neutrons on gadolinium generates γ rays with higher
511 energy meaning they are more easily detected. SK-VI has 0.01% Gd loading (0.02%
512 gadolinium sulphate by mass) which causes \approx 50% of neutrons emitted by IBD to
513 be captured on gadolinium [86, 87]. Whilst predominantly useful for low energy
514 analyses, Gd loading allows better $\nu/\bar{\nu}$ separation for atmospheric neutrino event
515 selections [88]. Efforts are currently in place to increase the gadolinium concentrate to
516 0.03% for \approx 75% neutron capture efficiency on gadolinium [DB: Link to Mark's talk at](#)
517 [Nu2022](#). The final stage of loading targets 0.1% concentrate.

518 2.1.2 Calibration

519 The calibration of the SK detector is documented in [78] and summarised below. The
520 analysis presented within this thesis is dependent upon ‘high energy events’ (Charged
521 particles with $O(> 100)\text{MeV}$ momenta). These are events that are expected to generate
522 a larger number of photons such that each PMT will be hit with multiple photons.
523 The reconstruction of these events depends upon the charge deposited within each
524 PMT and the timing response of each individual PMT. Therefore, the most relevant
525 calibration techniques to this thesis are outlined.

526 Before installation, 420 PMTs were calibrated to have identical charge responses
527 and then distributed throughout the tank in a cross-shape pattern (As illustrated by
528 Figure 2.2). These are used as a standardised measure for the rest of the PMTs installed
529 at similar geometric positions within SK to be calibrated against. To perform this
530 calibration, a xenon lamp is located at the center of the SK tank which flashes uniform
531 light at 1Hz. This allows for geometrical effects, water quality variation, and timing
532 effects to be measured in-situ throughout normal data-taking periods.

533 When specifically performing calibration of the detector (in out-of-data taking
534 mode), the water in the tank was circulated to avoid top/bottom asymmetric water
535 quality. Any non-uniformity within the tank significantly affects the PMT hit proba-
536 bility through scattering or absorption. This becomes a dominant effect for the very
537 low-intensity light sources discussed later which are designed such that only one
538 photon is incident upon a given PMT.

539 The “gain” of a PMT is defined as the ratio of the total charge of the signal produced
540 compared to the charge of photoelectrons emitted by the photocathodes within the
541 PMT. To calibrate the signal of each PMT, the “relative” and “absolute” gain values are

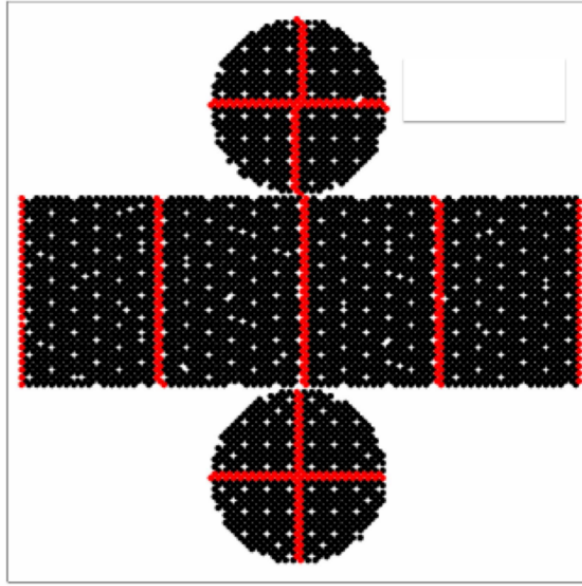


Figure 2.2: The location of “standard PMTs” (red) inside the SK detector. Taken from [78].

542 measured. The relative gain is the variation of gain among each of the PMTs whereas
 543 the absolute gain is the average gain of all PMTs.

544 The relative gain is calibrated as follows. A laser is used to generate two measure-
 545 ments; a high-intensity flash that illuminates every PMT with a sufficient number of
 546 photons, and a low-intensity flash in which only a small number of PMTs collect light.
 547 The first measurement creates an average charge, $Q_{obs}(i)$ on PMT i , whereas the second
 548 measurement ensures that each hit PMT only generates a single photoelectron. For the
 549 low-intensity measurement, the number of times each PMT records a charge larger
 550 than 1/4 photoelectrons, $N_{obs}(i)$, is counted. The values measured can be expressed as

$$\begin{aligned} Q_{obs}(i) &\propto I_H \times f(i) \times \epsilon(i) \times G(i), \\ N_{obs}(i) &\propto I_L \times f(i) \times \epsilon(i), \end{aligned} \tag{2.1}$$

551 Where I_H and I_L is the intensity of the high and low flashes, $f(i)$ is the acceptance
 552 efficiency of the i^{th} PMT, $\epsilon(i)$ is the product of the quantum and collection efficiency

553 of the i^{th} PMT and $G(i)$ is the gain of the i^{th} PMT. The relative gain for each PMT can
554 determined by taking the ratio of these quantities.

555 The absolute gain calibration is performed by observing fixed energy γ -rays of
556 $E_{\gamma} \sim 9\text{MeV}$ emitted isotropically from neutron capture on a NiCf source situated at
557 the center of the detector. This generates a photon yield of about 0.004 photoelec-
558 trons/PMT/event, meaning that $> 99\%$ of PMT signals are generated from single
559 photoelectrons. A charge distribution is generated by performing this calibration over
560 all PMTs, and the average value of this distribution is taken to be the absolute gain
561 value.

562 As mentioned in subsection 2.1.1, the average quantum and collection efficiency
563 for the SK detector is $\sim 21\%$ and $> 70\%$ respectively. However, these values do differ
564 between each PMT and need to be calibrated accordingly. Consequently, the NiCf
565 source is also used to calibrate the “quantum \times collection” efficiency (denoted “QE”)
566 value of each PMT. The NiCf low-intensity source is used as the PMT hit probability
567 is proportional to the QE ($N_{\text{obs}}(i) \propto \epsilon(i)$ in Equation 2.1). A Monte Carlo prediction
568 which includes photon absorption, scattering, and reflection is made to estimate the
569 number of photons incident on each PMT and the ratio of the number of predicted
570 to observed hits is calculated. The difference is attributed to the QE efficiency of that
571 PMT. This technique is extended to calculate the relative QE efficiency by normalizing
572 the average of all PMTs which removes the dependence on the light intensity.

573 Due to differing cable lengths and readout electronics, the timing response between
574 a photon hitting the PMT and the signal being captured by the data acquisition can be
575 different between each PMT. Due to threshold triggers (Described in subsection 2.1.3),
576 the time at which a pulse reaches a threshold is dependent upon the size of the pulse.
577 This is known as the ‘time-walk’ effect and also needs to be accounted for in each PMT.
578 To calibrate the timing response, a pulse of light with width 0.2ns is emitted into the

579 detector through a diffuser Two-dimensional distributions of time and pulse height
580 (or charge) are made for each PMT and are used to calibrate the timing response. This
581 is performed in-situ whilst data taking with the light source pulsing at 0.03Hz.

582 The top/bottom water quality asymmetry is measured using the NiCf calibration
583 data and cross-referencing these results to the “standard PMTs”. The water attenuation
584 length is continuously measured by the rate of vertically-downgoing cosmic-ray
585 muons which enter via the top of the tank.

586 2.1.3 Data Acquisition and Triggering

587 Dark noise is the phenomenon where a PMT registers a pulse that is consistent with a
588 single photoelectron emitted from photon detection despite the PMT being in complete
589 darkness. This is predominately caused by two processes. Firstly there is intrinsic
590 dark noise which is where photoelectrons gain enough thermal energy to be emitted
591 from the photocathode, and secondly, the radioactive decay of contaminants inside the
592 structure of the PMT. Typical dark noise rate for PMTs used within SK are $O(3)$ kHz [79]
593 which equates to about 12 dark noise hits per 220ns [89]. This is lower than the
594 expected number of photons generated for a ‘high energy event’ (As described in
595 subsection 2.1.4) but instability in this value can cause biases in reconstruction.

596 The analysis presented in this thesis only uses the SK-IV period of the SK exper-
597 iment so this subsection focuses on the relevant points of the data acquisition and
598 triggering systems to that SK period. The earlier data acquisition and triggering
599 systems are documented in [90, 91].

600 Before the SK-IV period started, the existing front-end electronics were replaced
601 with “QTC-Based Electrons with Ethernet, QBEE” systems [92]. When the QBEE
602 observes a signal above a 1/4 photoelectron threshold, the charge-to-time (QTC)

603 converter generates a rectangular pulse. The start of the rectangular pulse indicates
 604 the time at which the analog photoelectron signal was received and the width of the
 605 pulse indicates the total charge integrated throughout the signal. This is then digitized
 606 by time-to-digital converters and sent to the “front-end” PCs. The digitized signal
 607 from every QBEE is then chronologically ordered and sent to the “merger” PCs. It is
 608 the merger PCs that apply the software trigger. Any triggered events are passed to the
 609 “organizer” PC. This sorts the data stream of multiple merger PCs into chronologically
 610 ordered events which are then saved to disk. The schematic of data flow from PMTs to
 611 disk is illustrated in Figure 2.3.

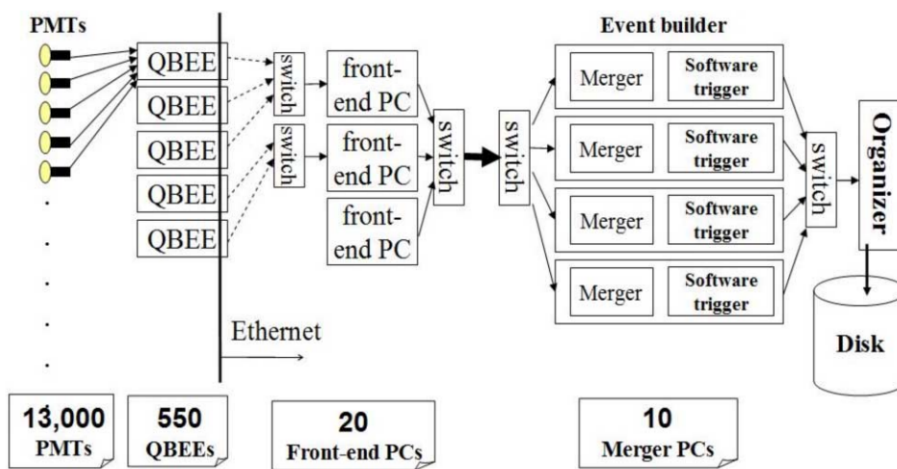


Figure 2.3: Schematic view of the data flow through the data acquisition and online system.
 Taken from [93].

612 The software trigger (described in [94]) operates by determining the number of
 613 PMT hits within a 200ns sliding window, N_{200} , coincides with the maximum time that
 614 a Cherenkov photon would take to traverse the length of the SK tank [91]. For lower
 615 energy events that generate fewer photons, this technique is useful for eliminating
 616 background processes like dark noise and radioactive decay which would be expected
 617 to separate in time. When the value of N_{200} exceeds some threshold, a software trigger
 618 is issued. There are several trigger thresholds used within the SK-IV period which are
 619 detailed in Table 2.2. If one of these thresholds is met, the PMT hits within an extended

time window are also read out and saved to disk. In the special case of an event that exceeds the SHE trigger but does not exceed the OD trigger, the AFT trigger looks for delayed coincidences of 2.2MeV gamma rays emitted from neutron capture in a $535\mu\text{s}$ window after the SHE trigger. A similar but more complex “Wideband Intelligent Trigger (WIT)” has been deployed and is described in [89].

Trigger	Acronym	Condition	Extended time window (μs)
Super Low Energy	SLE	>34/31 hits	1.3
Low Energy	LE	>47 hits	40
High Energy	HE	>50 hits	40
Super High Energy	SHE	>70/58 hits	40
Outer Detector	OD	>22 hits in OD	N/A

Table 2.2: The trigger thresholds and extended time windows saved around an event which were utilised throughout the SK-IV period. The exact thresholds can change and the values listed here represent the thresholds at the start and end of the SK-IV period.

2.1.4 Cherenkov Radiation

Cherenkov light is emitted from any highly energetic charged particle traveling with relativistic velocity, β , greater than the local speed of light in a medium [95]. Cherenkov light is formed at the surface of a cone with characteristic pitch angle,

$$\cos(\theta) = \frac{1}{\beta n}. \quad (2.2)$$

where n is the refractive index of the medium. Consequently, the Cherenkov momentum threshold, P_{thres} , is dependent upon the mass, m , of the charged particle moving through the media,

$$P_{thres} = \frac{m}{\sqrt{n^2 - 1}} \quad (2.3)$$

For water, where $n = 1.33$, the Cherenkov threshold momentum and energy for various particles are given in Table 2.3. In contrast, γ -rays are detected indirectly via the combination of photons generated by Compton scattering and pair production. The threshold for detection in the SK detector is typically higher than the threshold for photon production. This is due to the fact that the attenuation of photons in the water means that typically $\sim 75\%$ of Cherenkov photons reach the ID PMTs. Then the collection and quantum efficiencies described in subsection 2.1.1 result in the number of detected photons being lower than the number of photons which reach the PMTs.

Particle	Threshold Momentum (MeV)	Threshold Energy (MeV)
Electron	0.5828	0.7751
Muon	120.5	160.3
Pion	159.2	211.7
Proton	1070.0	1423.1

Table 2.3: The threshold momentum and energy for a particle to generate Cherenkov light in ultrapure water, as calculated in Equation 2.2 in ultrapure water which has refractive index $n = 1.33$.

The Frank-Tamm equation [96] describes the relationship between the number of Cherenkov photons generated per unit length, dN/dx , the wavelength of the photons generated, λ , and the relativistic velocity of the charged particle,

$$\frac{d^2N}{dxd\lambda} = 2\pi\alpha \left(1 - \frac{1}{n^2\beta^2}\right) \frac{1}{\lambda^2}. \quad (2.4)$$

where α is the fine structure constant. For a 100MeV momentum electron, approximately 330 photons will be produced per centimeter in the $300\text{nm} \leq \lambda \leq 700\text{nm}$ region which the ID PMTs are most sensitive to [79].

2.2 The Tokai to Kamioka Experiment

The Tokai to Kamioka (T2K) experiment is a long-baseline neutrino oscillation experiment located in Japan. Proposed in the early 2000s [97, 98] to replace K2K [99], T2K was designed to observe electron neutrino appearance whilst precisely measuring the oscillation parameters associated with muon neutrino disappearance [100]. The experiment consists of a neutrino beam generated at the Japan Proton Accelerator Research Complex (J-PARC), a suite of near detectors situated 280m from the beam target, and the Super Kamiokande far detector positioned at a 295km baseline. The cross-section view of the T2K experiment is drawn in Figure 2.4.

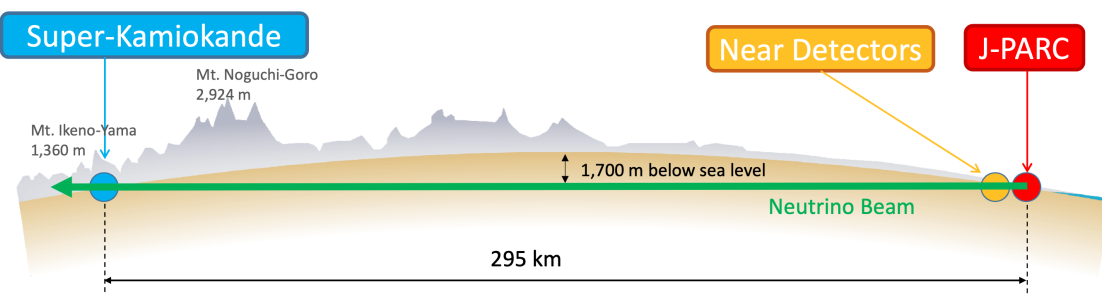


Figure 2.4: The cross-section view of the Tokai to Kamioka experiment illustrating the beam generation facility at J-PARC, the near detector situated at a baseline of 280m and the Super Kamiokande far detector situated 295km from the beam target.

The T2K collaboration makes world-leading measurements of the $\sin^2(\theta_{23})$, Δm_{23}^2 , and δ_{CP} oscillation parameters. Improvements in the precision and accuracy of parameter estimates are still being made by including new data samples and developing the models which describe the neutrino interactions and detector responses [DB: Link to Christophe's slides from Nu2022](#). Electron neutrino appearance was first observed

660 at T2K in 2014 [101] which accompanied a 7.3σ significance of a non-zero $\sin^2(\theta_{13})$
 661 measurement.

662 The near detectors provide constraints on the beam flux and cross-section model
 663 parameters used within the fit by observing the unoscillated neutrino beam. There
 664 are a host of detectors situated in the near detector hall (As illustrated in Figure 2.5);
 665 ND280 (subsection 2.2.2), INGRID (subsection 2.2.3), NINJA [102], WAGASCI [103],
 666 and Baby-MIND [104]. The latter three are not currently used within the oscillation
 667 analysis presented within this thesis.

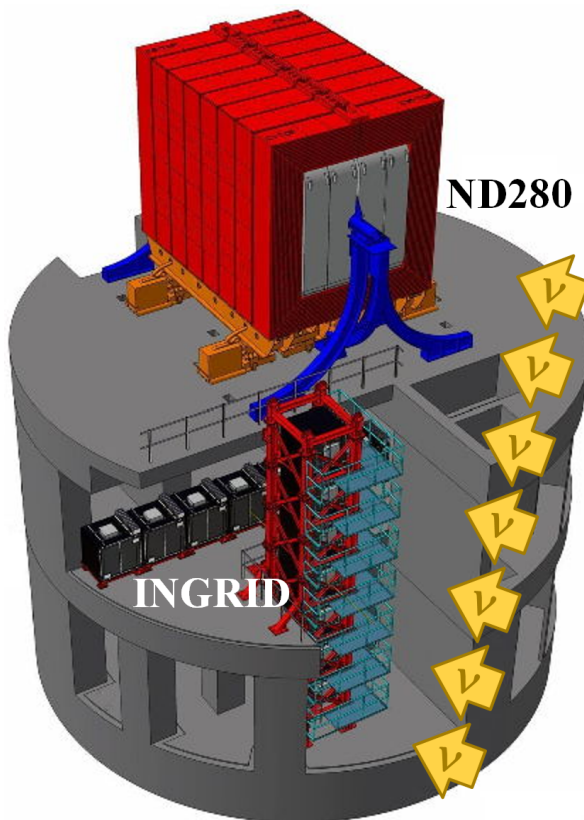


Figure 2.5: The near detector suite for the T2K experiment showing the ND280 and INGRID detectors. The distance between the detectors and the beam target is 280m.

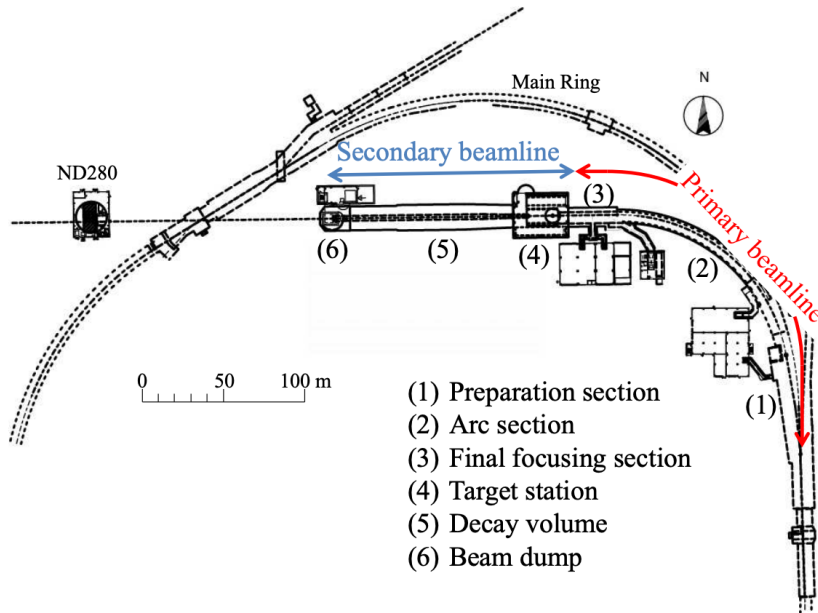
668 Whilst this thesis presents the ND280 in terms of its purpose for the oscillation
 669 analysis, the detector can also make many cross-section measurements at neutrino
 670 energies of $O(1)\text{GeV}$ for the different targets within the detector [105, 106]. These

671 measurements are of equal importance as they can lead the way in determining the
672 model parameters used in the interaction models for the future high-precision era of
673 neutrino physics.

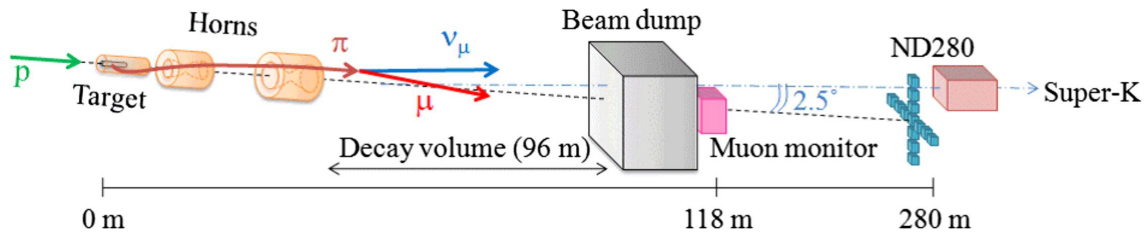
674 2.2.1 The Neutrino Beam

675 The neutrino beam used within the T2K experiment is described in [56, 107] and
676 summarised below. The accelerating facility at J-PARC is composed of two sections; the
677 primary and secondary beamlines. Figure 2.6 illustrates a schematic of the beamline,
678 focusing mostly on the components of the secondary beamline. The primary beamline
679 has three accelerators that progressively accelerate protons; a linear accelerator, a rapid-
680 cycling synchrotron, and the main-ring (MR) synchrotron. Once fully accelerated by
681 the MR, the protons have a kinetic energy of 30GeV. Eight bunches of these protons,
682 separated by 500ns, are extracted per “spill” from the MR and directed towards a
683 graphite target (A rod of length 91.4cm and diameter 2.6cm). Spills are extracted at
684 0.5Hz with $\sim 3 \times 10^{14}$ protons contained per spill.

685 The secondary beamline consists of three main components; the target station, the
686 decay volume, and the beam dump. The target station is comprised of the target, beam
687 monitors, and three magnetic focusing horns. The proton beam interacts with the
688 graphite target to form a secondary beam of mostly pions and kaons. The secondary
689 beam travels through a 96m long decay volume, generating neutrinos through the
690 following decays [56],



(a) Primary and secondary beamline



(b) Secondary beamline

Figure 2.6: Top panel: Bird's eye view of the most relevant part of primary and secondary beamline used within the T2K experiment. The primary beamline is the main-ring proton synchrotron, kicker magnet, and graphite target. The secondary beamline consists of the three focusing horns, decay volume, and beam dump. Figure taken from [107]. Bottom panel: The side-view of the secondary beamline including the focusing horns, beam dump and neutrino detectors. Figure taken from [108].

$$\begin{array}{ll}
 \pi^+ \rightarrow \mu^+ + \nu_\mu & \pi^- \rightarrow \mu^- + \bar{\nu}_\mu \\
 K^+ \rightarrow \mu^+ + \nu_\mu & K^- \rightarrow \mu^- + \bar{\nu}_\mu \\
 \rightarrow \pi^0 + e^+ + \nu_e & \rightarrow \pi^0 + e^- + \bar{\nu}_e \\
 \rightarrow \pi^0 + \mu^+ + \nu_\mu & \rightarrow \pi^0 + \mu^- + \bar{\nu}_\mu \\
 K_L^0 \rightarrow \pi^- + e^+ + \nu_e & K_L^0 \rightarrow \pi^+ + e^- + \bar{\nu}_e \\
 \rightarrow \pi^- + \mu^+ + \nu_\mu & \rightarrow \pi^+ + \mu^- + \bar{\nu}_\mu \\
 \mu^+ \rightarrow e^+ + \bar{\nu}_\mu + \nu_e & \mu^- \rightarrow e^- + \nu_\mu + \bar{\nu}_e
 \end{array}$$

The electrically charged component of the secondary beam is focused towards the far detector by the three magnetic horns. These horns direct charged particles of a particular polarity towards SK whilst defocusing the oppositely charged particles. This allows a mostly neutrino or mostly antineutrino beam to be used within the experiment, denoted as “forward horn current (FHC)” or “reverse horn current (RHC)” respectively.

Figure 2.7 illustrates the different contributions to the FHC and RHC neutrino flux.

The low energy flux is dominated by the decay of pions whereas kaon decay becomes the dominant source of neutrinos for $E_\nu > 3\text{GeV}$. The “wrong-sign” component, which is the $\bar{\nu}_\mu$ background in a ν_μ beam, and the intrinsic irreducible ν_e background are predominantly due to muon decay for $E_\nu < 2\text{GeV}$. As the antineutrino cross-section is smaller than the neutrino cross-section, the wrong-sign component is more dominant in the RHC beam as compared to that in the FHC beam.

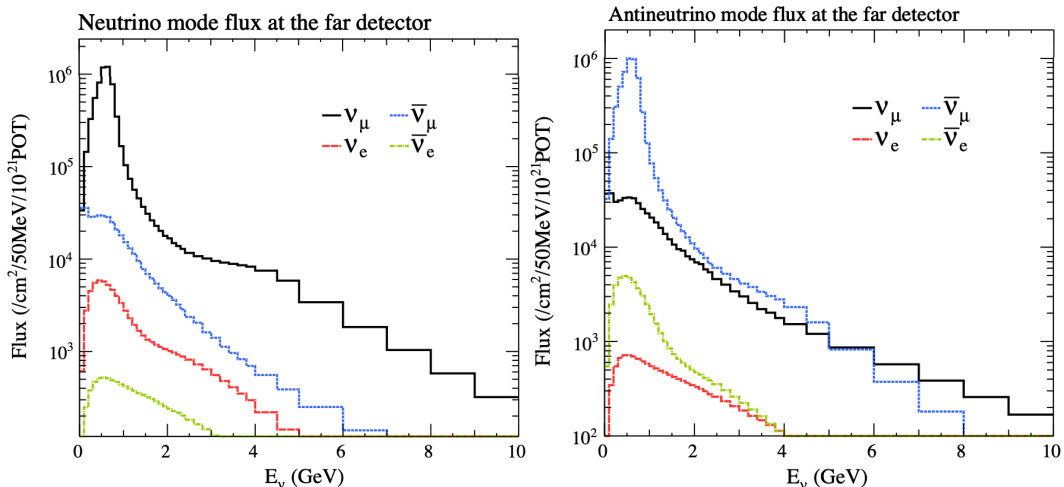


Figure 2.7: The Monte Carlo prediction of the energy spectrum for each flavour of neutrino (ν_e , $\bar{\nu}_e$, ν_μ and $\bar{\nu}_\mu$) in the neutrino dominated beam FHC mode (Left) and antineutrino dominated beam RHC mode (Right) expected at SK. Taken from [109].

The beam dump, situated at the end of the decay volume, stops all charged particles other than highly energetic muons ($p_\mu > 5\text{GeV}$). The MuMon detector monitors the

⁷⁰⁷ penetrating muons to determine the beam direction and intensity which is used to
⁷⁰⁸ constrain some of the beam flux systematics within the analysis [108, 110].

⁷⁰⁹ The T2K experiment uses an off-axis beam to narrow the neutrino energy distribu-
⁷¹⁰ tion. This was the first implementation of this technique in a long-baseline neutrino
⁷¹¹ oscillation experiment after its original proposal [111]. Pion decay, $\pi \rightarrow \mu + \nu_\mu$, is a
⁷¹² two-body decay. Consequently, the neutrino energy, E_ν , can be determined based on
⁷¹³ the pion energy, E_π , and the angle at which the neutrino is emitted, θ ,

$$E_\nu = \frac{m_\pi^2 - m_\mu^2}{2(E_\pi - p_\pi \cos(\theta))}, \quad (2.5)$$

⁷¹⁴ where m_π and m_μ are the mass of the pion and muon respectively. For a fixed
⁷¹⁵ energy pion, the neutrino energy distribution is dependent upon the angle at which
⁷¹⁶ the neutrinos are observed from the initial pion beam direction. For the 295km
⁷¹⁷ baseline at T2K, $E_\nu = 0.6\text{GeV}$ maximises the electron neutrino appearance probability,
⁷¹⁸ $P(\nu_\mu \rightarrow \nu_e)$, whilst minimising the muon disappearance probability, $P(\nu_\mu \rightarrow \nu_\mu)$.
⁷¹⁹ Figure 2.8 illustrates the neutrino energy distribution for a range of off-axis angles, as
⁷²⁰ well as the oscillation probabilities most relevant to T2K.

⁷²¹ 2.2.2 The Near Detector at 280m

⁷²² Whilst all the near detectors are situated in the same “pit” located at 280m from the
⁷²³ beamline, the “ND280” detector is the off-axis detector which is situated at the same
⁷²⁴ off-axis angle as the Super-Kamiokande far detector. It has two primary functions;
⁷²⁵ firstly it measures the neutrino flux and secondly it counts the event rates of different
⁷²⁶ types of neutrino interactions. Both of these constrain the flux and cross-section

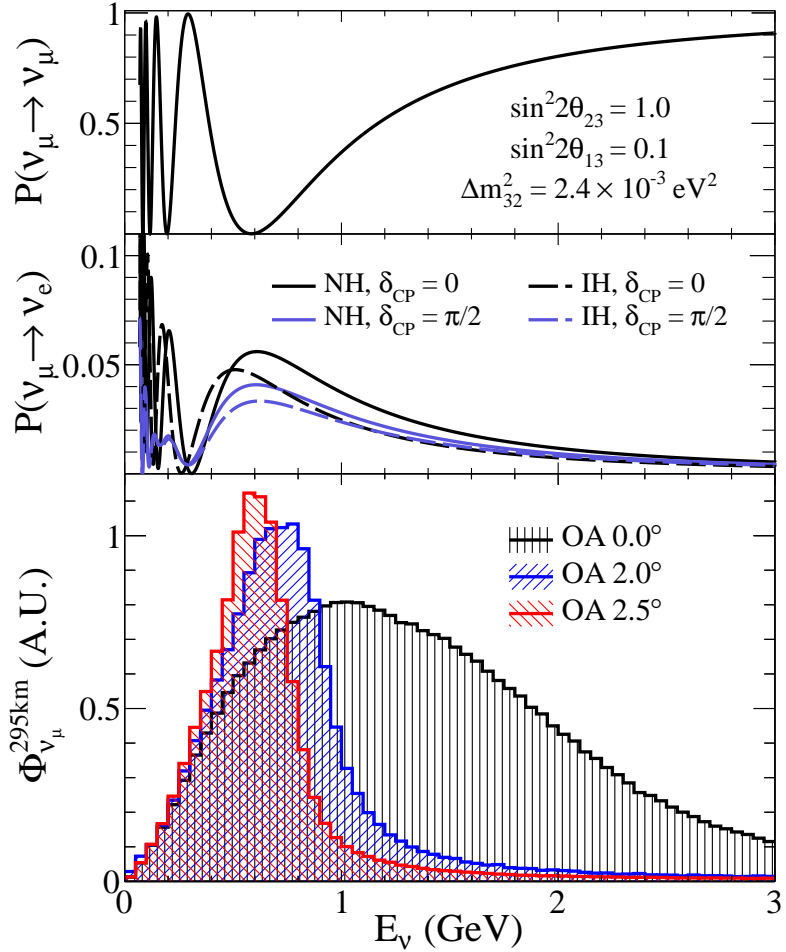


Figure 2.8: Top panel: T2K muon neutrino disappearance probability as a function of neutrino energy. Middle panel: T2K electron neutrino appearance probability as a function of neutrino energy. Bottom panel: The neutrino flux distribution for three different off-axis angles (Arbitrary units) as a function of neutrino energy.

727 systematics invoked within the model for a more accurate prediction of the expected
 728 event rate at the far detector.

729 As illustrated in Figure 2.9, the ND280 detector consists of several sub-detectors.
 730 The most important part of the detector for this analysis is the tracker region. This is
 731 comprised of two time projection chambers (TPCs) sandwiched between three fine
 732 grain detectors (FGDs). The FGDs contain both hydrocarbon plastics and water tar-
 733 gets for neutrino interactions and provide track reconstruction near the interaction
 734 vertex. The emitted charged particles can then propagate into the TPCs which pro-
 735 vide particle identification and momentum reconstruction. The FGDs and TPCs are

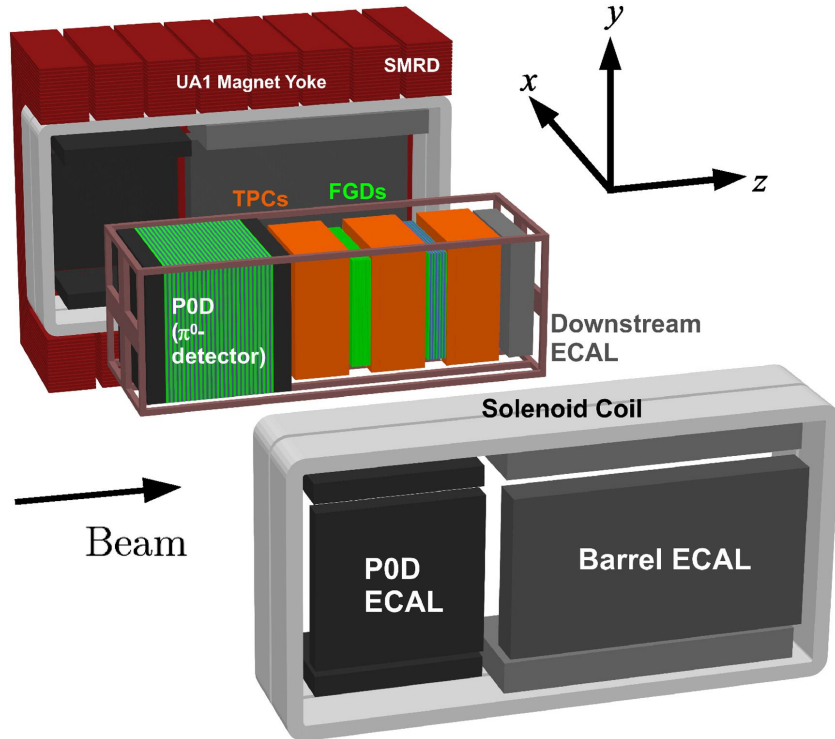


Figure 2.9: The components of the ND280 detector. The neutrino beam travels from left to right. Taken from [107].

⁷³⁶ further described in subsubsection 2.2.2.1 and subsubsection 2.2.2.2 respectively. The
⁷³⁷ electromagnetic calorimeter (ECAL) encapsulates the tracker region alongside the π^0
⁷³⁸ detector (P0D). The ECAL measures the deposited energy from photons emitted from
⁷³⁹ interactions within the FGD. The P0D constrains the cross-section of neutral current
⁷⁴⁰ interactions which generate neutral pions, which is one of the largest backgrounds in
⁷⁴¹ the electron neutrino appearance oscillation channel. The P0D and ECAL detectors
⁷⁴² are detailed in subsubsection 2.2.2.3 and subsubsection 2.2.2.4 respectively. The entire
⁷⁴³ detector is located within a large yolk magnet which produces a 0.2T magnetic field.
⁷⁴⁴ This design of the magnet also includes a scintillating detector called the side muon
⁷⁴⁵ range detector (SMRD) which is used to track high-angle muons as well as acting as a
⁷⁴⁶ cosmic veto. The SMRD is described in subsubsection 2.2.2.5.

747 2.2.2.1 Fine Grained Detectors

748 The T2K tracker region is comprised of two fine grained detectors (FGD) and three
749 Time Projection Chambers (TPC). A detailed description of the FGD design, construc-
750 tion, and assembly is found in [112] and summarised below. The FGDs are the primary
751 target for neutrino interactions with a mass of 1.1 tonnes per FGD. Alongside this,
752 the FGDs are designed to be able to track short-range particles which do not exit the
753 FGD. Typically, short-range particles are low momentum and are observed as tracks
754 that deposit a large amount of energy per unit length. This means the FGD needs
755 good granularity to resolve these particles. The FGDs have the best timing resolution
756 ($\sim 3\text{ns}$) of any of the sub-detectors of the ND280 detector. As such, the FGDs are
757 used for time of flight measurements to determine forward going positively charged
758 particles from backward going negatively charged particles. Finally, any tracks which
759 pass through multiple sub-detectors are required to be track matched to the FGD.

760 Both FDGs are made from square scintillator planes of side length 186cm and width
761 2.02cm. Each plane consists of two layers of 192 scintillator bars in an XY orientation.
762 A wave-length shift fiber is threaded through the center of each bar and is read out by
763 a multi-photon pixel counter (MPPC). FGD1 is the most upstream of the two FGDs
764 and contains 15 planes of carbon plastic scintillator which is a common target in
765 external neutrino scattering data. As the far detector is a pure water target, 7 of the 15
766 scintillator planes in FGD2 have been replaced with a hybrid water-scintillator target.
767 Due to the complexity of the nucleus, nuclear effects can not be extrapolated between
768 different nuclei. Therefore having the ability to take data on one target which is the
769 same as external data and another target which is the same as the far detector target is
770 beneficial for reliable model parameter estimates.

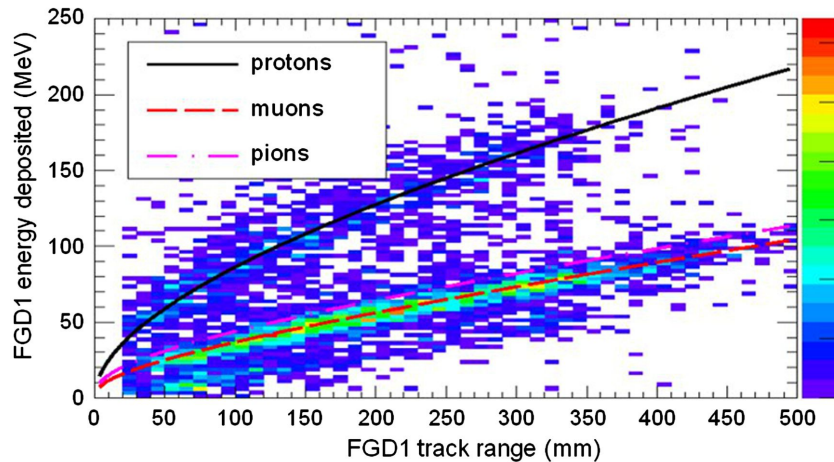


Figure 2.10: Comparison of data to Monte Carlo prediction of integrated deposited energy as a function of track length for particles that stopped in FGD1. Taken from [112].

771 The integrated deposited energy is used for particle identification. The FGD
 772 can distinguish protons from other charged particles by comparing the integrated
 773 deposited energy from data to Monte Carlo prediction as seen in Figure 2.10.

774 2.2.2.2 Time Projection Chambers

775 The majority of particle identification and momentum measurements within ND280
 776 are provided by three Time Projection Chambers (TPCs) [113]. The TPCs are located
 777 on either side of the FGDs. They are located inside of the magnetic field meaning the
 778 momentum of a charged particle can be determined from the bending of the track.

779 Each TPC module consists of two gas-tight boxes, as shown in Figure 2.11, which
 780 are made of non-magnetic material. The outer box is filled with CO₂ which acts as
 781 an electrical insulator between the inner box and the ground. The inner box forms
 782 the field cage which produces a uniform electric drift field of $\sim 275\text{V/cm}$ and an
 783 argon gas mixture. Charged particles moving through this gas mixture ionize the gas
 784 mixture. The ionised charge is drifted towards micromega detectors which measure
 785 the ionization charge. The time and position information in the readout allows a
 786 three-dimensional image of the neutrino interaction.

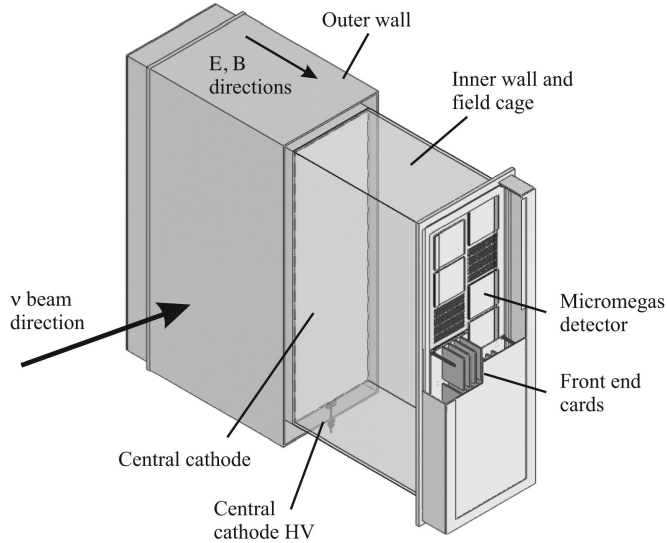


Figure 2.11: Schematic design of a Time Projection Chamber detector. Taken from [113].

The particle identification of tracks that pass through the TPCs is performed using

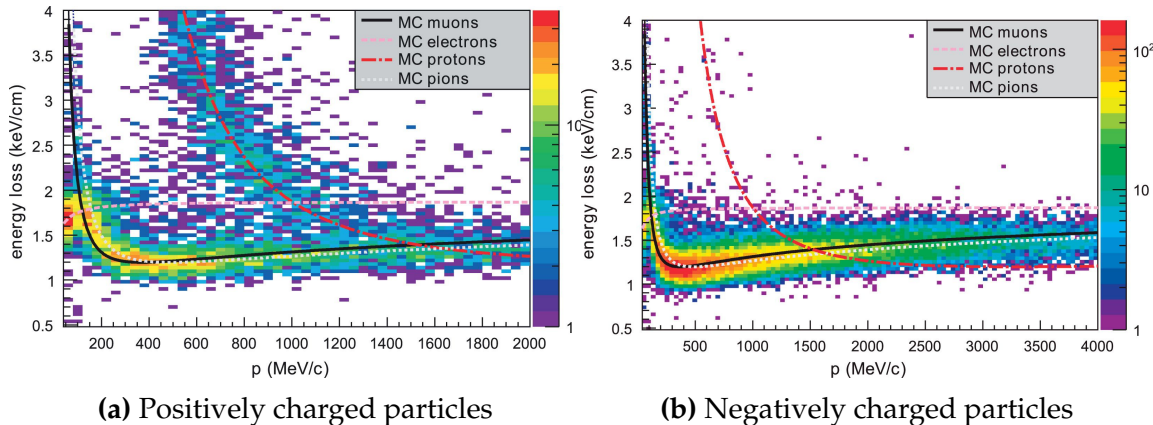
dE/dx measurements. Figure 2.12 illustrates the data to Monte Carlo distributions

of the energy lost by a charged particle passing through the TPC as a function of the

reconstructed particle momentum. The resolution is $7.8 \pm 0.2\%$ meaning that electrons

and muons can be distinguished. This allows reliable measurements of the intrinsic ν_e

component of the beam.



(a) Positively charged particles

(b) Negatively charged particles

Figure 2.12: The distribution of energy loss as a function of reconstructed momentum for charged particles passing through the TPC, comparing data to Monte Carlo prediction. Taken from [113].

793 2.2.2.3 π^0 Detector

794 If one of the γ -rays from a $\pi^0 \rightarrow 2\gamma$ decay is missed at the far detector, the reconstruc-
795 tion will determine that event to be electron-like. This is one of the main backgrounds
796 hindering the electron neutrino appearance searches. Therefore, the π^0 detector (P0D)
797 measures the cross-section of the neutral current induced neutral pion production on
798 a water target.

799 The P0D is a cube of approximately 2.5m length. The P0D consists of layers of
800 scintillating bars, brass and lead sheets, and water bags as illustrated in Figure 2.13.
801 Two electromagnetic calorimeters are positioned at the most upstream and most
802 downstream position in the sub-detector and the water target is situated in between
803 them. The scintillator layers are built from two triangular bars orientated in opposite
804 directions to form a rectangular layer. Each triangular scintillator bar is threaded with
805 optical fiber which is read out by MPPCs. The high-Z brass and lead regions produce
806 electron showers from the photons emitted in π^0 decay.

807 The sub-detector can generate measurements of NC1 π^0 cross-sections on a water
808 target by measuring the event rate both with and without the water target, with the
809 cross-section on a water target being determined as the difference. The total active
810 mass is 16.1 tonnes when filled with water and 13.3 tonnes when empty.

811 2.2.2.4 Electromagnetic Calorimeter

812 The electromagnetic calorimeter [115] (ECal) encapsulates the P0D and tracking sub-
813 detectors. Its primary purpose is to aid π^0 reconstruction from any interaction in
814 the tracker. To do this, it measures the energy and direction of photon showers from
815 $\pi^0 \rightarrow 2\gamma$ decay. It can also distinguish pion and muon tracks depending on the shape
816 of the photon shower deposited.

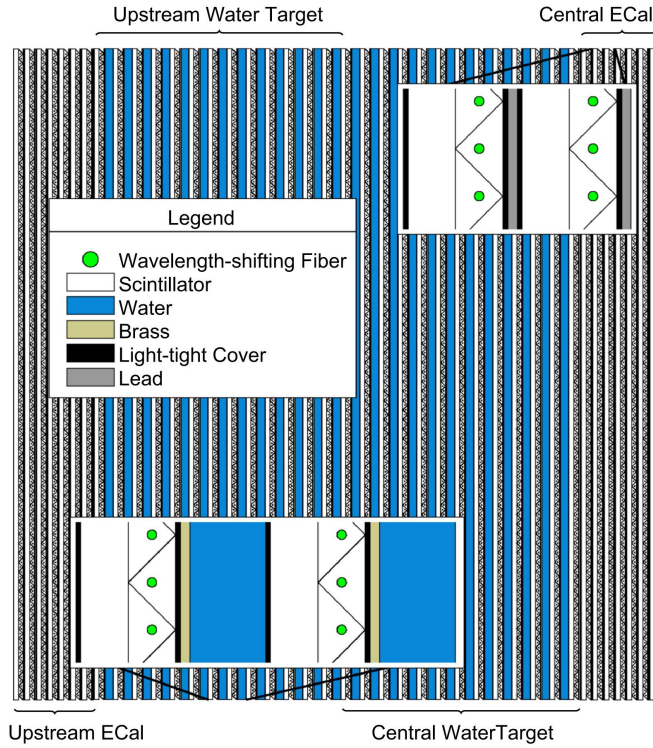


Figure 2.13: A schematic of the P0D side-view. Taken from [114].

The ECal is comprised of three sections; the P0D ECal which surrounds the P0D, the barrel ECal which encompasses the tracking region, and the downstream ECal which is situated downstream of the tracker region. The barrel and downstream ECals are tracking calorimeters that focus on electromagnetic showers from high-angle particles emitted from the tracking sub-detectors. Particularly in the TPC, high-angle tracks (those which travel perpendicularly to the beam-axis) can travel along a single scintillator bar resulting in very few hits. The width of the barrel and downstream ECal corresponds to ~ 11 electron radiation lengths to ensure $\sim 50\%$ of the energy of the π^0 is contained. As the P0D has its own calorimetry which reconstructs showers, the P0D ECal determines the energy which escapes the P0D.

Each ECal is constructed of multiple layers of scintillating bars sandwiched between lead sheets. The scintillating bars are threaded with optical fiber and read out by MPPCs. Each sequential layer of the scintillator is orientated perpendicular to the previous which allows a two-dimensional readout, which when temporal, information

⁸³¹ is included results in three-dimension event displays. The target mass of the P0D ECal,
⁸³² barrel ECal, and downstream ECal are 1.50, 4.80 and 6.62 tonnes respectively.

⁸³³ **2.2.2.5 Side Muon Range Detector**

⁸³⁴ As illustrated in Figure 2.9, the ECal, FGDs, P0D, and TPCs are enclosed within the
⁸³⁵ UA1 magnet. Originally designed for the NOMAD [116] experiment and reconditioned
⁸³⁶ for use in the T2K experiment [117], the UA1 magnet provides a uniform horizontal
⁸³⁷ magnetic field of $0.2 \pm 2 \times 10^{-4}$ T.

⁸³⁸ Built into the UA1 magnet, the side muon range detector (SMRD) [118] monitors
⁸³⁹ high-energy muons which leave the tracking region and permeate through the ECal.
⁸⁴⁰ It additionally acts as a cosmic muon veto and trigger.

⁸⁴¹ **2.2.3 The Interactive Neutrino GRID**

⁸⁴² The Interactive Neutrino GRID (INGRID) detector is situated within the same “pit” as
⁸⁴³ the other near detectors. It is aligned with the beam in the “on-axis” position and mea-
⁸⁴⁴ sures the beam direction, spread, and intensity. The detector was originally designed
⁸⁴⁵ with 16 identical modules [107] (two modules have since been decommissioned) and a
⁸⁴⁶ “proton” module. The design of the detector is cross-shaped with length and height
⁸⁴⁷ 10m × 10m as illustrated in Figure 2.14.

⁸⁴⁸ Each module is composed of iron sheets interlaced with eleven tracking scintillator
⁸⁴⁹ planes for a total target mass of 7.1 tonnes per module. The scintillator design is an X-Y
⁸⁵⁰ pattern of 24 bars in both orientations, where each bar contains wave-length shifting
⁸⁵¹ fibers which are connected to multi-pixel photon counters (MPPCs). The MPPCs
⁸⁵² convert detected photons into electrical signals via photodiodes. This is then read
⁸⁵³ out by Trip-T front-end electronics [119] and passed to the readout merging modules

854 along with timing information from the clock module. Each module is encapsulated
855 inside veto planes to aid the rejection of charged particles entering the module.

856 The proton module is different from the other modules in that it consists of entirely
857 scintillator planes with no iron target. The scintillator bars are also smaller than those
858 used in the other modules to increase the granularity of the detector and improve
859 tracking capabilities. The module sits in the center of the beamline and is designed to
860 give precise measurements of quasi-elastic charged current interactions to evaluate
861 the performance of the Monte Carlo simulation of the beamline.

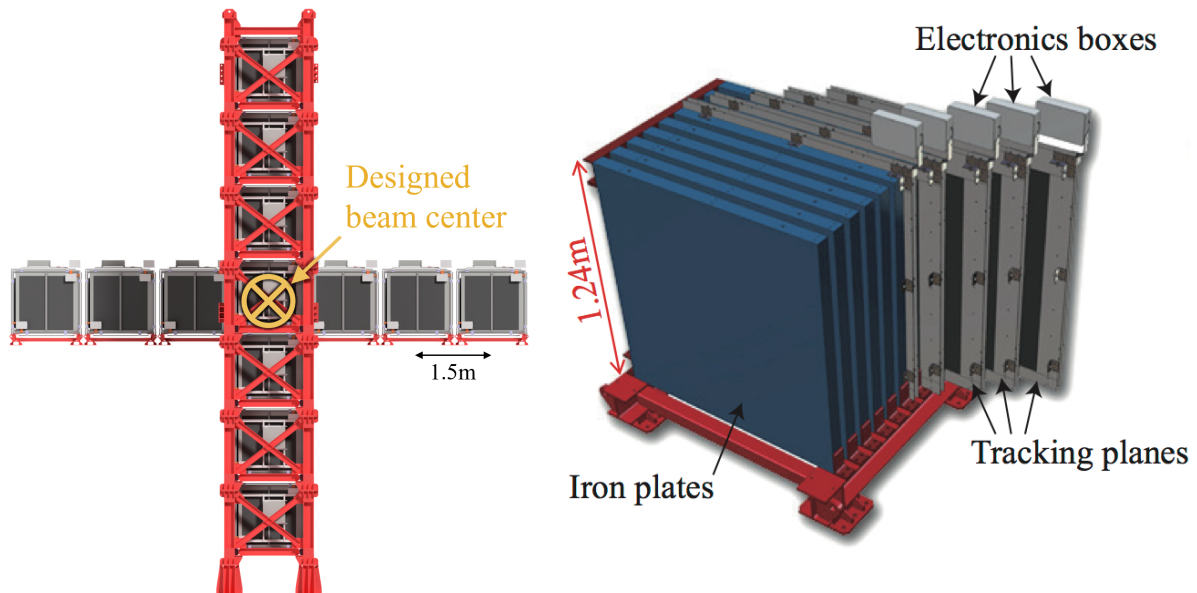


Figure 2.14: Left panel: The Interactive Neutrino GRID on-axis Detector. 14 modules are arranged in a cross-shape configuration, with the center modules being directly aligned with the on-axis beam. Right panel: The layout of a single module of the INGRID detector. Both figures are recreated from [107].

862 The INGRID detector can measure the beam direction to an uncertainty of 0.4mrad
863 and the beam center within a resolution of 10cm [107]. The beam direction in both the
864 vertical and horizontal directions is discussed in [120] and it is found to be in good
865 agreement with the MUMON monitor described in subsection 2.2.1.

866 **Chapter 3**

867 **Bayesian Statistics and Markov Chain**
868 **Monte Carlo Techniques**

869 The analysis throughout this thesis is based upon a Bayesian oscillation analysis. To
870 extract the oscillation parameters, a Markov Chain Monte Carlo (MCMC) method is
871 used. This chapter explains the theory of how parameter estimates can be determined
872 using this technique and condenses the material found in the literature [121–124].

873 The oscillation parameter determination presented within this thesis is built upon a
874 simultaneous fit to the near detector, far detector beam, and atmospheric neutrino data.
875 In total, there are four oscillation parameters of interest ($\sin^2(\theta_{23})$, $\sin^2(\theta_{13})$, Δm_{23}^2 ,
876 and δ_{CP}), two oscillation parameters to which this study will not be sensitive ($\sin^2(\theta_{12})$
877 , Δm_{12}^2) and many nuisance parameters that control the systematic uncertainty models
878 invoked within this study. The systematic uncertainties can be grouped into categories
879 depending on how they are defined; 574 bin-normalisations due to the near detector
880 response, 45 bin-normalisations to describe the far detector response to neutrino beam
881 events, 27 parameters to describe the detector response to atmospheric neutrino events,
882 100 to model the bin-normalisation due to beam flux uncertainties, 18 which model the
883 atmospheric flux uncertainties, and 87 to describe the correlated cross-section model.
884 An alternative parameterisation, where the far detector response is correlated between
885 the beam and atmospheric samples, replaces the bin-normalisation parameters with
886 224 shift and smear systematics. Section [DB: Link to Systematics Chapter](#) describes
887 the systematic model in more depth.

888 The MCMC technique generates a multi-dimensional probability distribution across
 889 all of the model parameters used in the fit. To determine the parameter estimate of a
 890 single parameter, this multi-dimensional object is integrated over all other parameters.
 891 This process is called Marginalisation and is further described in subsection 3.3.1.
 892 Monte Carlo techniques approximate the probability distribution of each parameter
 893 within the limit of generating infinite samples. As ever, generating a large number of
 894 samples is time and resource-dependent. Therefore, an MCMC technique is utilised
 895 within this analysis to reduce the required number of steps to sufficiently sample the
 896 parameter space. This technique is described in further detail in subsection 3.2.1.

897 **3.1 Bayesian Statistics**

898 According to Bayesian Inference, observables and parameters of a statistical model are
 899 treated on an equal footing. To estimate model parameters $\vec{\theta}$ from some data D , one
 900 needs to define the joint probability distribution $P(D|\vec{\theta})$ which can be described as the
 901 prior distribution for model parameters $P(\vec{\theta})$ and the likelihood of the data given the
 902 model parameters $P(D|\vec{\theta})$,

$$P(D, \vec{\theta}) = P(D|\vec{\theta})P(\vec{\theta}). \quad (3.1)$$

903 The prior distribution, $P(\vec{\theta})$, describes all previous knowledge about the parameters
 904 within the model. For example, if the risk of developing health problems is known
 905 to increase with age, the prior distribution would describe the increase. For the
 906 purpose of this analysis, the prior distribution is typically the best-fit values taken
 907 from external data measurements with a Gaussian uncertainty. The prior distribution

908 can also contain correlations between model parameters. In an analysis using Monte
 909 Carlo techniques, the likelihood of measuring some data assuming some set of model
 910 parameters is calculated by comparing the Monte Carlo prediction generated at that
 911 particular set of model parameters to the data.

912 It is parameter estimation that is important for this analysis and as such, we apply
 913 Bayes' theorem [125]. To calculate the probability for each parameter to have a certain
 914 value given the observed data $P(\vec{\theta}|D)$, known as the posterior distribution (often
 915 termed the posterior). This can be expressed as

$$P(\vec{\theta}|D) = \frac{P(D|\vec{\theta})P(\vec{\theta})}{\int P(D|\vec{\theta})P(\vec{\theta})d\vec{\theta}}. \quad (3.2)$$

916 The denominator in Equation 3.2 is the integral of the joint probability distribution
 917 over all values of all parameters used within the fit. For brevity, we say that the
 918 posterior distribution is

$$P(\vec{\theta}|D)\alpha P(D|\vec{\theta})P(\vec{\theta}). \quad (3.3)$$

919 In subsection 3.3.1, we see that for the cases used within this analysis, it is reason-
 920 able to know the posterior to some normalisation constant.

921 3.2 Monte Carlo Simulation

922 Monte Carlo techniques are used to numerically solve a complex problem that does
 923 not necessarily have an analytical solution. These techniques rely on building a large

ensemble of samples from an unknown distribution and then using the ensemble to approximate the properties of the distribution.

An example that uses Monte Carlo techniques is to calculate the area underneath a curve. For example, take the problem of calculating the area under a straight line with gradient $M = 0.4$ and intercept $C = 1.0$. Analytically, one can calculate the area under the line is equal to 30 units for $0 \leq x \leq 10$. Using Monte Carlo techniques, one can calculate the area under this line by throwing many random values for the x and y components of each sample and then calculating whether that point falls below the line. The area can then be calculated by the ratio of points below the line to the total number of samples thrown multiplied by the total area in which samples were scattered. The study is shown in Figure 3.1 highlights this technique and finds the area under the curve to be 29.9 compared to an analytical solution of 30.0. The deviation of the numerical to analytical solution can be attributed to the number of samples used in the study. The accuracy of the approximation in which the properties of the Monte Carlo samples replicate those of the desired distribution is dependent on the number of samples used. Replicating this study with a differing number of Monte Carlo samples used in each study (As shown in Figure 3.2) highlights how the Monte Carlo techniques are only accurate within the limit of a high number of samples.

Whilst the above example has an analytical solution, these techniques are just as applicable to complex solutions. Clearly, any numerical solution is only as useful as its efficiency. As discussed, the accuracy of the Monte Carlo technique is dependent upon the number of samples generated to approximate the properties of the distribution. Furthermore, if the positions at which the samples are evaluated are not 'cleverly' picked, the efficiency of the Monte Carlo technique significantly drops. Given the example in Figure 3.1, if the region in which the samples are scattered significantly extends passed the region of interest, many calculations will be calculated but do

not add to the ability of the Monte Carlo technique to achieve the correct result. For instance, any sample evaluated at a $y \geq 5$ could be removed without affecting the final result. This does bring in an aspect of the ‘chicken and egg’ problem in that to achieve efficient sampling, one needs to know the distribution beforehand.

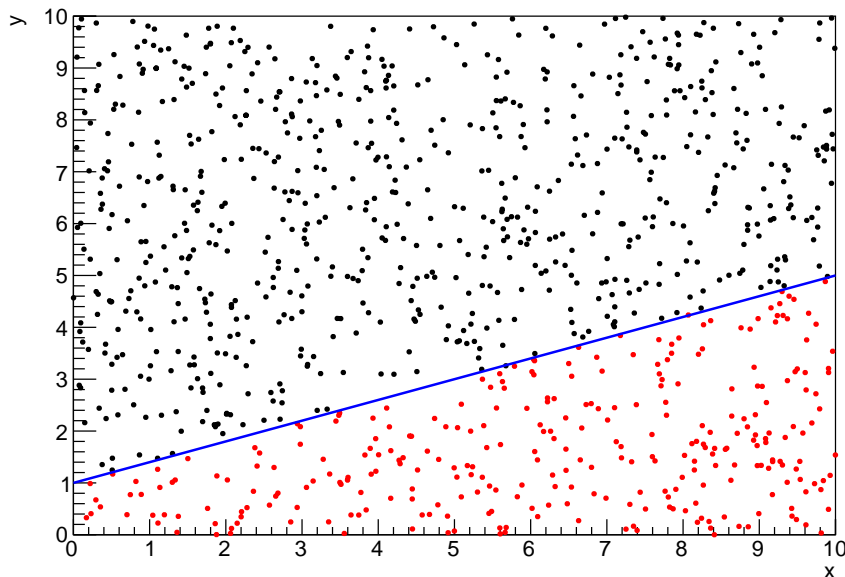


Figure 3.1: Example of using Monte Carlo techniques to find the area under the blue line. The gradient and intercept of the line are 0.4 and 1.0 respectively. The area found to be under the curve using one thousand samples is 29.9 units.

3.2.1 Markov Chain Monte Carlo

This analysis utilises a multi-dimensional probability distribution, with some dimensions being significantly more constrained than others. This could be from prior knowledge of parameter distributions from external data or un-physical regions in which parameters can not exist. Consequently, the Monte Carlo techniques used need to be as efficient as possible. For this analysis, the Markov Chain Monte Carlo (MCMC) technique is chosen. An MCMC technique is a Monte Carlo technique that uses a Markov chain to select which points at which to sample the parameter distribution.

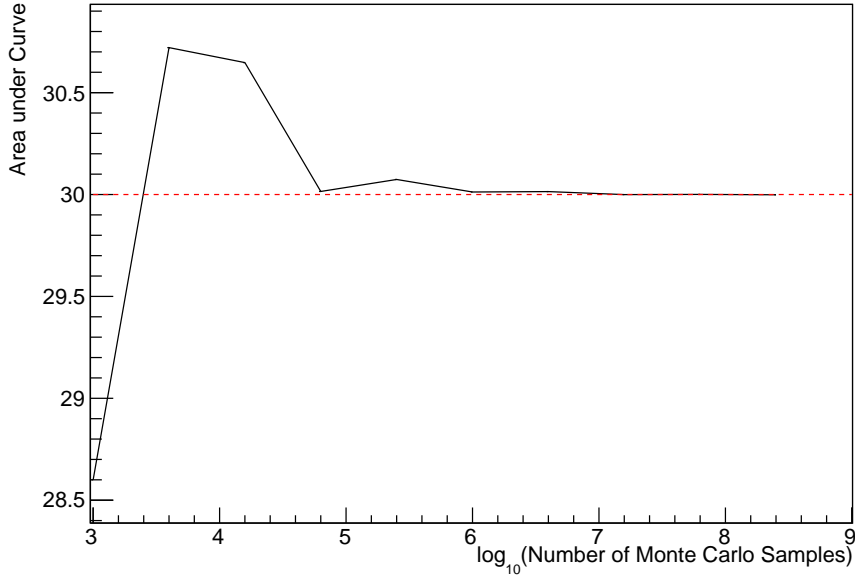


Figure 3.2: The area under a line of gradient 0.4 and intercept 1.0 for the range $0 \leq x \leq 10$ as calculated using Monte Carlo techniques as a function of the number of samples used in each repetition. The analytical solution to the area is 30 units as given by the red line.

962 This technique performs a semi-random stochastic walk through the allowable pa-
 963 rameter space. This builds a posterior distribution which has the property that the
 964 density of sampled points is proportional to the probability density of that parame-
 965 ter. This does mean that the samples produced by this technique are not statistically
 966 independent but they will cover the space of the distribution.

967 A Markov chain functions by selecting the position of step \vec{x}_{i+1} based on the
 968 position of \vec{x}_i . The space in which the Markov chain selects samples is dependent
 969 upon the total number of parameters utilised within the fit, where a discrete point in
 970 this space is described by the N-dimensional space \vec{x} . In a perfectly operating Markov
 971 chain, the position of the next step depends solely on the previous step and not on the
 972 further history of the chain (\vec{x}_0, \vec{x}_1 , etc.). However, in solving the multi-dimensionality
 973 of the fit used within this analysis, each step becomes correlated with several of
 974 the steps preceding itself. This behaviour is further explained in subsection 3.2.3.
 975 Providing the MCMC chain is well optimised, it will begin to converge towards a

976 unique stationary distribution. The period between the chain's initial starting point
977 and the convergence to the unique stationary distribution is colloquially known as the
978 burn-in period. This is discussed further in subsection 3.2.3. Once the chain reaches
979 the stationary distribution, all points sampled after that point will look like samples
980 from that distribution.

981 Further details of the theories underpinning MCMC techniques are discussed
982 in [122] but can be summarised by the requirement that the chain satisfies the three
983 'regularity conditions':

- 984 • Irreducibility: From every position in the parameter space \vec{x} , there must exist a
985 non-zero probability for every other position in the parameter space to be reached.
- 986 • Recurrence: Once the chain arrives at the stationary distribution, every step fol-
987 lowing from that position must be samples from the same stationary distribution.
- 988 • Aperiodicity: The chain must not repeat the same sequence of steps at any point
989 throughout the sampling period.

990 The output of the chain after burn-in (ie. the sampled points after the chain
991 has reached the stationary distribution) can be used to approximate the posterior
992 distribution and model parameters $\vec{\theta}$. To achieve the requirement that the unique
993 stationary distribution found by the chain be the posterior distribution, one can use
994 the Metropolis-Hastings algorithm. This guides the stochastic process depending on
995 the likelihood of the current proposed step compared to that of the previous step.
996 Implementation and other details of this technique are discussed in subsection 3.2.2.

⁹⁹⁷ 3.2.2 Metropolis-Hastings Algorithm

⁹⁹⁸ As a requirement for MCMCs, the Markov chain implemented in this technique must
⁹⁹⁹ have a unique stationary distribution that is equivalent to the posterior distribution.
¹⁰⁰⁰ To ensure this requirement and that the regularity conditions are met, this analysis
¹⁰⁰¹ utilises the Metropolis-Hastings (MH) algorithm [126,127]. For the i^{th} step in the chain,
¹⁰⁰² the MH algorithm determines the position in the parameter space to which the chain
¹⁰⁰³ moves to based on the current step, \vec{x}_i , and the proposed step, \vec{y}_{i+1} . The proposed step
¹⁰⁰⁴ is randomly selected from some proposal function $f(\vec{x}_{i+1}|\vec{x}_i)$, which depends solely
¹⁰⁰⁵ on the current step (ie. not the further history of the chain). The next step in the chain
¹⁰⁰⁶ \vec{x}_{i+1} can be either the current step or the proposed step determined by whether the
¹⁰⁰⁷ proposed step is accepted or rejected. To decide if the proposed step is selected, the
¹⁰⁰⁸ acceptance probability, $\alpha(\vec{x}_i, \vec{y}_i)$, is calculated as

$$\alpha(\vec{x}_i, \vec{y}_{i+1}) = \min\left(1, \frac{P(\vec{y}_{i+1}|D)f(\vec{x}_i|\vec{y}_{i+1})}{P(\vec{x}_i|D)f(\vec{y}_{i+1}|\vec{x}_i)}\right). \quad (3.4)$$

¹⁰⁰⁹ Where $P(\vec{y}_{i+1}|D)$ is the posterior distribution as introduced in section 3.1. To
¹⁰¹⁰ simplify this calculation, the proposal function is required to be symmetric such that
¹⁰¹¹ $f(\vec{x}_i|\vec{y}_{i+1}) = f(\vec{y}_{i+1}|\vec{x}_i)$. In practice, a multi-variate Gaussian distribution is used to
¹⁰¹² throw parameter proposals from. This reduces Equation 3.4 to

$$\alpha(\vec{x}_i, \vec{y}_{i+1}) = \min\left(1, \frac{P(\vec{y}_{i+1}|D)}{P(\vec{x}_i|D)}\right). \quad (3.5)$$

1013 After calculating this quantity, a random number, β , is generated uniformly be-
1014 tween 0 and 1. If $\beta \leq \alpha(\vec{x}_i, \vec{y}_{i+1})$, the proposed step is accepted. Otherwise, the chain
1015 sets the next step equal to the current step and this procedure is repeated. This can be
1016 interpreted as if the posterior probability of the proposed step is greater than that of
1017 the current step, ($P(\vec{y}_{i+1}|D) \geq P(\vec{x}_i|D)$), the proposed step will always be accepted.
1018 If the opposite is true, ($P(\vec{y}_{i+1}|D) \leq P(\vec{x}_i|D)$), the proposed step will be accepted
1019 with probability $P(\vec{x}_i|D)/P(\vec{y}_{i+1}|D)$. This ensures that the Markov chain does not get
1020 trapped in any local minima in the potentially non-Gaussian posterior distribution.
1021 The outcome of this technique is that the density of steps taken in a discrete region is
1022 directly proportional to the probability density in that region.

1023 3.2.3 MCMC Optimisation

1024 As discussed in subsection 3.2.2, the proposal function invoked within the MH algo-
1025 rithm can take any form and the chain will still converge to the stationary distribution.
1026 As discussed in [DB: Link to Analysis Strategy Section](#), this analysis performs the
1027 Monte Carlo reweighting on an event-by-event basis. This requires significant com-
1028 putational resources to perform a parameter fit. Therefore, the number of steps taken
1029 before the unique stationary distribution is found should be minimised as only steps
1030 after convergence add information to the fit. Furthermore, the chain should entirely
1031 cover the allowable parameter space to ensure that all values have been considered.
1032 Tuning the distance that the proposal function jumps between steps on a parameter-
1033 by-parameter basis can both minimise the length of the burn-in period and ensure that
1034 the correlation between step \vec{x}_i and \vec{x}_j is sufficiently small.

1035 The effect of changing the width of the proposal function is highlighted in Figure 3.3.
1036 Three scenarios, each with the same underlying stationary distribution (A Gaussian of
1037 width 1.0 and mean 0.), are presented. The only difference between the three scenarios

is the width of the proposal function, colloquially known as the ‘step size σ ’. Each scenario starts at an initial parameter value of 10.0 which would be considered an extreme variation. For the case where $\sigma = 0.1$, it is clear to see that the chain takes a long time to reach the expected region of the parameter. This indicates that this chain would have a large burn-in period and does not converge to the stationary distribution until step ~ 500 . Furthermore, whilst the chain does move towards the expected region, each step is significantly correlated with the previous. Considering the case where $\sigma = 5.0$, the chain approaches the expected parameter region almost instantly meaning that the burn-in period is not significant. However, there are clearly large regions of steps where the chain does not move. This is likely due to the chain proposing steps in the tails of the distribution which have a low probability of being accepted. Consequently, this chain would take a significant number of steps to fully span the allowable parameter region. For the final scenario, where $\sigma = 0.5$, you can see a relatively small burn-in period of approximately 100 steps. Once the chain reaches the stationary distribution, it moves throughout the expected region of parameter values many times, sufficiently sampling the full parameter region. This example is a single parameter varying across a continuous distribution and does not fully reflect the difficulties in the many-hundred multi-variate parameter distribution used within this analysis. However, it does give a conceptual idea of the importance of selecting the proposal function and associated step size.

As discussed, step size tuning directly correlates to the average step acceptance rate. If the step size is too small, many steps will be accepted but the chain moves slowly. If the opposite is true, many steps will be rejected as the chain proposes steps in the tails of the distribution. Discussion in [128] suggests that the ‘ideal’ acceptance rate of a high dimension MCMC chain should be approximately $\sim 25\%$. An “ideal” step size [128] of

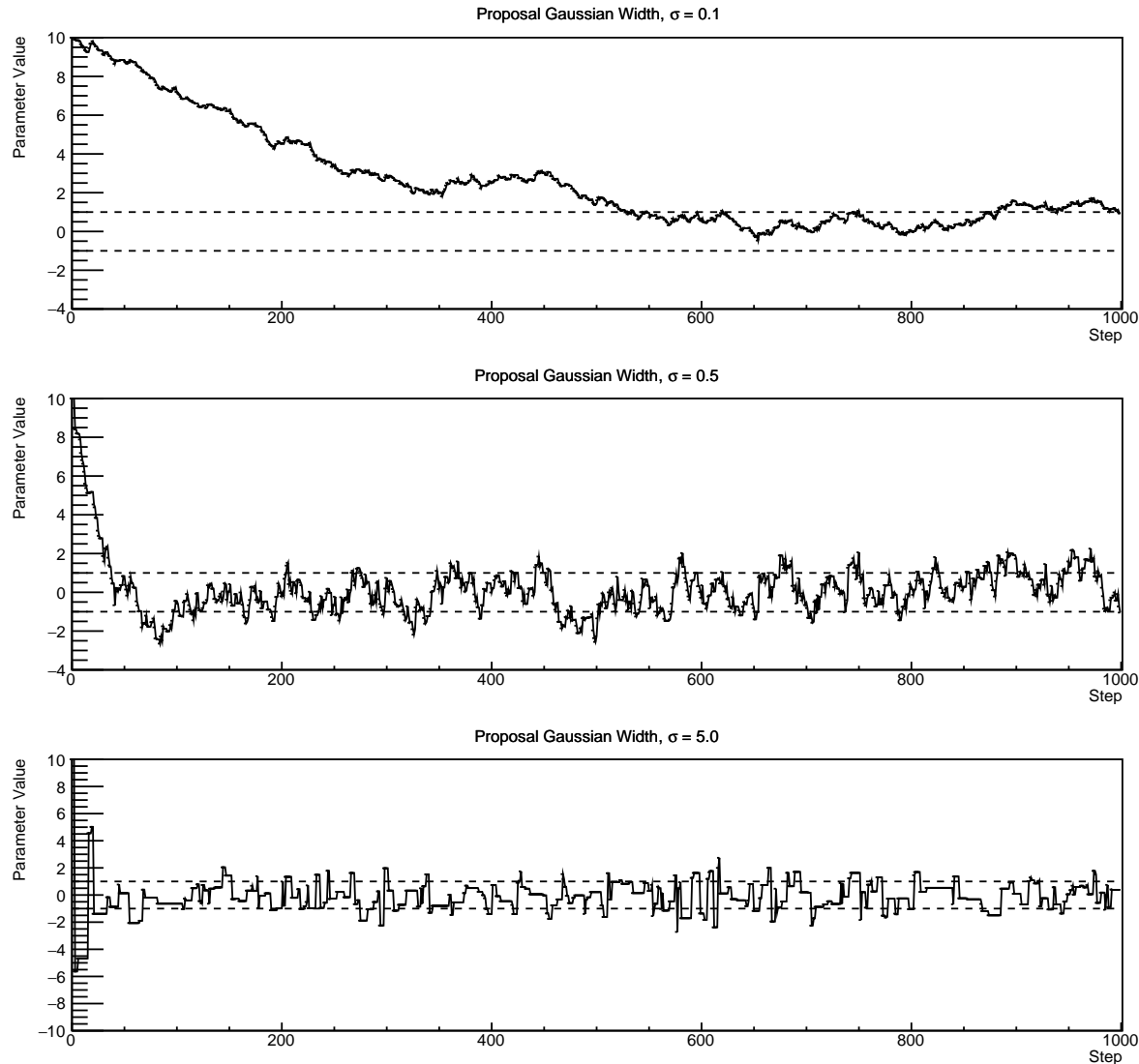


Figure 3.3: Three MCMC chains, each with a stationary distribution equal to a Gaussian centered at 0 and width 1 (As indicated by the black dotted lines). All of the chains use a Gaussian proposal function but have different widths (or ‘step size σ ’). The top panel has $\sigma = 0.1$, middle panel has $\sigma = 0.5$ and the bottom panel has $\sigma = 5.0$.

$$\sigma = \frac{2.4}{N_p}, \quad (3.6)$$

where N_p is the number of parameters included in the MCMC fit. However, the complex correlations between systematics mean that some parameters have to be hand

1066 tuned and many efforts have been taken to select a set of parameter-by-parameter step
1067 sizes to approximately reach the ideal acceptance rate.

1068 Figure 3.3 highlights the likelihood as calculated by the fit in [DB: Link to AsimovA](#)
1069 [Sensitivity Section](#) as a function of the number of steps in each chain. In practice,
1070 many independent MCMC chains are run simultaneously to parallelise the task of
1071 performing the fit. This figure overlays the distribution found in each chain. As seen,
1072 the likelihood decreases from its initial value and converges towards a stationary
1073 distribution after $\sim 1 \times 10^5$ steps. Each fit (whether it be different asimov fits or data
1074 fit) will have a different set of preferred parameter values which results in a different
1075 stationary distribution. For each fit presented in this thesis, a burn-in period of 1×10^5
1076 steps was found to be sufficient.

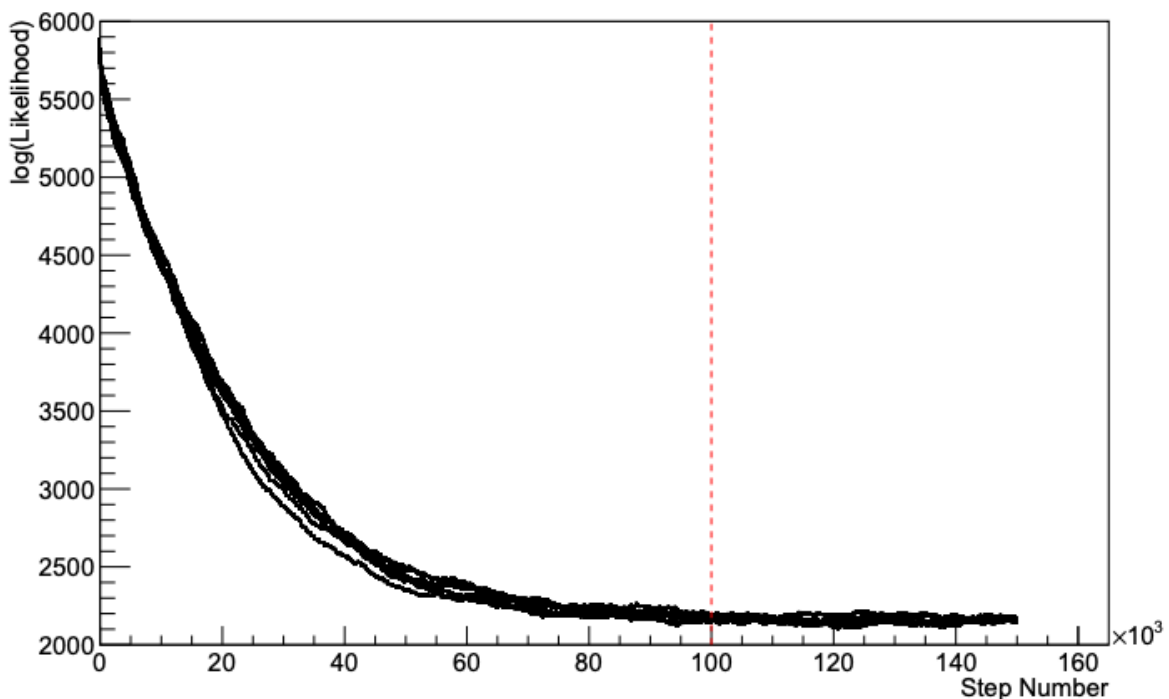


Figure 3.4: The log-likelihood from the fit detailed in [DB: Link to AsimovA](#) [Sensitivity Section](#) as a function of the number of steps accumulated in each fit. Many independent MCMC chains were run in parallel and overlaid on this plot. The red line indicates the 1×10^5 step burn-in period after which the log-likelihood becomes stable.

1077 3.3 Understanding the MCMC Results

1078 Whilst section 3.1 and section 3.2 describe how to interpret Bayesian statistics and
1079 explains the MCMC techniques used within this analysis, there is no mention of
1080 how to interpret the output of the chain. The posterior distribution output from the
1081 chain is a high dimension object, with as many dimensions as there are parameters
1082 included in the fit. However, this multi-dimensional object is difficult to conceptualize
1083 so parameter estimations are often presented in one or two-dimensional projections
1084 of this probability distribution. To do this, we invoke the marginalisation technique
1085 highlighted in subsection 3.3.1.

1086 3.3.1 Marginalisation

1087 The output of the MCMC chain is a highly dimensional probability distribution
1088 which is very difficult to interpret. From the standpoint of an oscillation analysis
1089 experiment, the one or two-dimensional ‘projections’ of the oscillation parameters of
1090 interest are most relevant. Despite this, the best fit values and uncertainties on the
1091 oscillation parameters of interest should correctly encapsulate the correlations to the
1092 other systematic uncertainties (colloquially called ‘nuisance’ parameters). For this joint
1093 beam and atmospheric analysis, the oscillation parameters of interest are $\sin^2(\theta_{23})$,
1094 $\sin^2(\theta_{13})$, Δm_{23}^2 , and δ_{CP} . All other parameters (Including the oscillation parameter
1095 this fit is insensitive to) are deemed nuisance parameters. To generate these projections,
1096 we rely upon integrating the posterior distribution over all nuisance parameters. This
1097 is called marginalisation. A simple example of this technique is to imagine the scenario
1098 where two coins are flipped. To determine the probability that the first coin returned
1099 a ‘head’, the exact result of the second coin flip is disregarded and simply integrated

1100 over. For the parameters of interest, $\vec{\theta}_i$, we can calculate the marginalised posterior by
1101 integrating over the nuisance parameters, $\vec{\theta}_n$. In this case, Equation 3.2 becomes

$$P(\vec{\theta}_i|D) = \frac{\int P(D|\vec{\theta}_i, \vec{\theta}_n)P(\vec{\theta}_i, \vec{\theta}_n)d\vec{\theta}_n}{\int P(D|\vec{\theta})P(\vec{\theta})d\vec{\theta}} \quad (3.7)$$

1102 Where $P(\vec{\theta}_i, \vec{\theta}_n)$ encodes the prior knowledge about the uncertainty and correlations
1103 between the parameters of interest and the nuisance parameters. In practice, this
1104 is simply taking the one or two-dimensional projection of the multi-dimensional
1105 probability distribution.

1106 Whilst in principle an easy solution to a complex problem, correlations between the
1107 interesting and nuisance parameters can bias the marginalised results. A similar effect
1108 is found when the parameters being marginalised over have non-Gaussian probability
1109 distributions. For example, Figure 3.5 highlights the marginalisation bias in the
1110 probability distribution found for a parameter when requiring a correlated parameter
1111 to have a positive parameter value. Due to the complex nature of this oscillation
1112 parameter fit presented in this thesis, there are certainly correlations occurring between
1113 the oscillation parameters of interest and the other nuisance parameters included in
1114 the fit.

1115 3.3.2 Parameter Estimation and Credible Intervals

1116 The purpose of this analysis is to determine the best fit values for the oscillation
1117 parameters that the beam and atmospheric samples are sensitive to; $\sin^2(\theta_{23})$, $\sin^2(\theta_{13})$
1118, Δm_{23}^2 , and δ_{CP} . Typically, the results presented take the form of one or two-dimension
1119 marginalised probability distributions for the appearance ($\sin^2(\theta_{13})$ and δ_{CP}) and

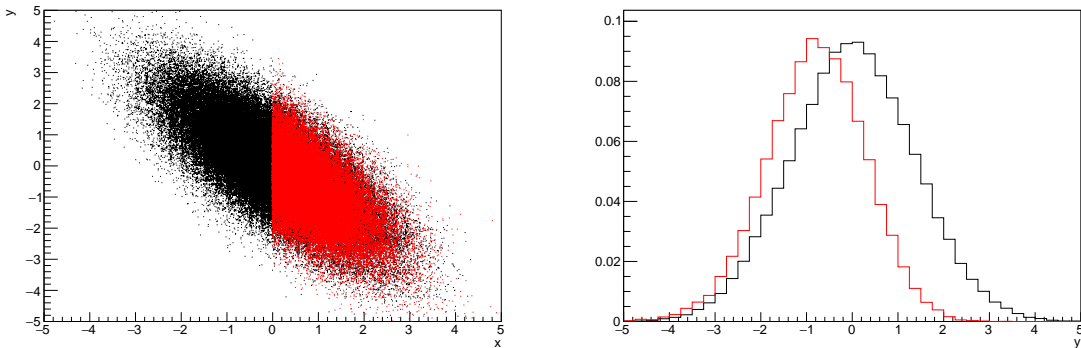


Figure 3.5: Left: The two dimensional probability distribution for two correlated parameters x and y . The red distribution shows the two dimensional probability distribution when $0 \leq x \leq 5$. Right: The marginalised probability distribution for the y parameter found when requiring the x to be bound between $-5 \leq x \leq 5$ and $0 \leq x \leq 5$ for the black and red distribution, respectively.

disappearance ($\sin^2(\theta_{23})$ and Δm_{23}^2) parameters. The posterior probability density taken from the output MCMC chain is binned in these parameters. The parameter best-fit point is then taken to be the value that has the highest posterior probability. This is performed in both one and two-dimensional projections.

However, the single best-fit point in a given parameter is not of much use on its own. We would also like to determine the uncertainty, or credible interval, on that best-fit point. The definition of the 1σ credible interval is that we have 68% belief that the parameter is within those bounds. For a more generalised definition, the credible interval is the region of the posterior distribution that contains a specific fraction of the total probability, such that

$$\int P(\theta|D)d\theta = \alpha \quad (3.8)$$

Where θ is the parameter on which we calculate the credible interval. This technique then calculates the $\alpha \times 100\%$ credible interval.

In practice, this analysis uses the highest posterior density (HPD) credible intervals which are calculated through the following method. First, the probability distribution is area-normalised such that it has an integrated area equal to 1.0. The bins of probability are then summed from the highest to lowest until the sum exceeds the 1σ level (0.68 in this example). This process is repeated for a range of credible intervals, notably the 1σ , 2σ and 3σ along with other levels where the critical values for each level can be found in [129]. This process can be repeated for the two-dimensional probability distributions by creating two-dimensional contours of credible intervals rather than a one-dimensional result.

3.3.3 Application of Bayes' Theorem

Due to the matter resonance, this analysis has some sensitivity to the mass hierarchy of neutrino states (whether Δm_{23}^2 is positive or negative) and the octant of $\sin^2(\theta_{23})$. The Bayesian approach utilised within this analysis gives an intuitive method of model comparison by determining which hypothesis is most favourable. Taking the ratio of Equation 3.3 for the two hypotheses of normal hierarchy, NH , and inverted hierarchy, IH , gives

$$\frac{P(\vec{\theta}_{NH}|D)}{P(\vec{\theta}_{IH}|D)} = \frac{P(D|\vec{\theta}_{NH})}{P(D|\vec{\theta}_{IH})} \times \frac{P(\vec{\theta}_{NH})}{P(\vec{\theta}_{IH})}. \quad (3.9)$$

The middle term defines the Bayes factor which is a data-driven interpretation of how strong the data prefers one hierarchy to the other. For this analysis, equal priors on both mass hierarchy hypotheses are chosen ($P(\vec{\theta}_{NH}) = P(\vec{\theta}_{IH}) = 0.5$). In practice, the MCMC chain proposes a value of $|\Delta m_{23}^2|$ and then applies a 50% probability that the value is sign flipped. Consequently, the Bayes factor can be calculated from

1153 the ratio of the probability density in either hypothesis. This equates to counting the
1154 number of steps taken in the normal and inverted hierarchies and taking the ratio. The
1155 same approach can be taken to compare the upper octant (UO) compared to the lower
1156 octant (LO) hypothesis of $\sin^2(\theta_{23})$.

1157 Whilst the value of the Bayes factor should always be shown, the Jeffreys scale [130]
1158 (highlighted in Table 3.1) gives an indication of the strength of preference for one model
1159 compared to the other. Other interpretations of the strength of preference of a model
1160 exist, e.g. the Kass and Raferty Scale [131].

$\log_{10}(B_{AB})$	B_{AB}	Strength of Preference
< 0.0	< 1	No preference for hypothesis A (Supports hypothesis B)
0.0 – 0.5	1.0 – 3.16	Preference for hypothesis A is weak
0.5 – 1.0	3.16 – 10.0	Preference for hypothesis A is substantial
1.0 – 1.5	10.0 – 31.6	Preference for hypothesis A is strong
1.5 – 2.0	31.6 – 100.0	Preference for hypothesis A is very strong
> 2.0	> 100.0	Decisive preference for hypothesis A

Table 3.1: Jeffreys scale for strength of preference for two models A and B as a function of the calculated Bayes factor ($B_{AB} = B(A/B)$) between the two models [130]. The original scale is given in terms of $\log_{10}(B(A/B))$ but converted to linear scale for easy comparison throughout this thesis.

1161 3.3.4 Comparison of MCMC Output to Expectation

1162 Whilst not important for the extraction of oscillation parameters, understanding how
1163 the data constrains the model parameters is important to the understanding of this
1164 analysis. A simple method of doing this is to perform a comparison in the fitting
1165 parameters (For instance, the reconstructed neutrino energy and lepton direction for
1166 T2K far detector beam samples) of the spectra generated by the MCMC chain to ‘data’.
1167 This ‘data’ could be true data or some variation of Monte Carlo prediction. This allows
1168 easy comparison of the MCMC probability distribution to the data. To perform this, N

1169 steps from the post burn-in MCMC chain are randomly selected (Where for all plots
1170 of this style in this thesis, $N = 3000$). From these, the Monte Carlo prediction at each
1171 step is generated by reweighting the model parameters to the values specified at that
1172 step. Due to the probability density being directly correlated with the density of steps
1173 in a certain region, parameter values close to the best fit value are most likely to be
1174 selected.

1175 In practice, for each bin of the fitting parameters has a probability distribution
1176 of event rates, with one entry per sampled MCMC step. This distribution is binned
1177 where the bin with the highest probability is selected as the mean and an error on
1178 the width of this probability distribution is calculated using the approach highlighted
1179 in subsection 3.3.2. Consequently, the best fit distribution in the fit parameter is not
1180 necessarily that which would be attained by reweighting the Monte Carlo prediction
1181 to the most probable parameter values.

1182 A similar study can be performed to illustrate the freedom of the model parameter
1183 space prior to the fit. This can be done by throwing parameter values from the prior
1184 uncertainty of each parameter. This becomes troublesome for parameters with no
1185 prior uncertainty as the range is technically infinite. Where applicable solutions to
1186 remove these have been addressed.

₁₁₈₇ **Chapter 4**

₁₁₈₈ **Simulation, Reconstruction and Event Se-**
₁₁₈₉ **lections**

₁₁₉₀ **4.1 Simulation**

₁₁₉₁ In order to generate a Monte Carlo prediction of the expected event rate at the far
₁₁₉₂ detector for both sets of samples, all the processes in the beamline, atmospheric flux,
₁₁₉₃ neutrino interaction, and detector need to be modeled. The beamline simulation
₁₁₉₄ consists of three distinct parts; initial hadron interaction modeling, target station
₁₁₉₅ geometry and particle tracking and hadronic re-interactions. These are modeled by
₁₁₉₆ FLUKA [132], JNUBEAM [133, 134], and GCALOR [135], respectively. FLUKA is
₁₁₉₇ not very adaptable but matches external cross-section measurements in the region of
₁₁₉₈ interest better than GCALOR ($O(10)$ GeV). Thus a small simulation is built to model
₁₁₉₉ the interactions in the target and the output is then passed to JNUBEAM and GCALOR
₁₂₀₀ for propagation. The hadronic interactions are tuned to data from the NA61/SHINE
₁₂₀₁ [136–138] and HARP [139] experiments. The tuning is done by reweighting the FLUKA
₁₂₀₂ and GCALOR predictions to match the external data multiplicity and cross-section
₁₂₀₃ measurements, based on final state particle kinematics [140]. The predicted flux for
₁₂₀₄ neutrino and antineutrino beam modes is illustrated in Figure 2.7.

₁₂₀₅ The atmospheric neutrino flux predictions are simulated by the HKKM model
₁₂₀₆ [40, 42], where the primary cosmic ray flux is tuned to AMS [141] and BESS [142]

external data assuming the US-standard atmosphere '76 [143] density profile and includes geomagnetic field effects. Secondary interactions of pions and muons are handled by DPMJET-III [144] for energies above 32GeV and JAM [42, 145] for energies below that value. These hadronic interactions are tuned to external data [146, 147] using the same methodology as the tuning of the beamline simulation. The energy and cosine zenith predictions of $\nu_e, \bar{\nu}_e, \nu_\mu, \bar{\nu}_\mu$ flux are given in Figure 1.3 and Figure 1.5, respectively. The flux is approximately symmetrical and peaked around $\cos(\theta_Z) = 0.0$. This is because horizontally-going pions and kaons can travel further than their vertically-going counterparts resulting in a larger probability of decay to neutrinos. The symmetry is broken in low-energy neutrinos due to geomagnetic effects, which modify the track of the primary cosmic rays.

The neutrino interactions in all three detectors are simulated with NEUT [148, 149]. This simulates quasi-elastic (QE), meson exchange (MEC), single meson production (PROD), coherent pion production (COH), and deep inelastic scattering (DIS) interactions. These interaction categories can be further broken down by whether they were propagated via a W^\pm boson in Charged Current (CC) interactions or via a Z^0 boson in Neutral Current (NC) interactions. CC interactions have a charged lepton in the final state, which can be flavour-tagged in reconstruction to determine the flavour of the neutrino. In contrast, NC interactions have a neutrino in the final state so no flavour information can be determined from the observables in the detector. This is the reason why NC events are assumed to not oscillate within the analysis. Both CC and NC interactions are modeled for all the above interaction categories, other than MEC interactions which are only modeled for CC events. The SK detector is only sensitive to charged particles, so all charged current interactions are simulated whilst only neutral current processes that produce charged mesons (NCDIS, NCCOH, and NCPROD) are modeled. NC MEC interactions can only produce charged particles through secondary re-interactions which is a low cross-section process.

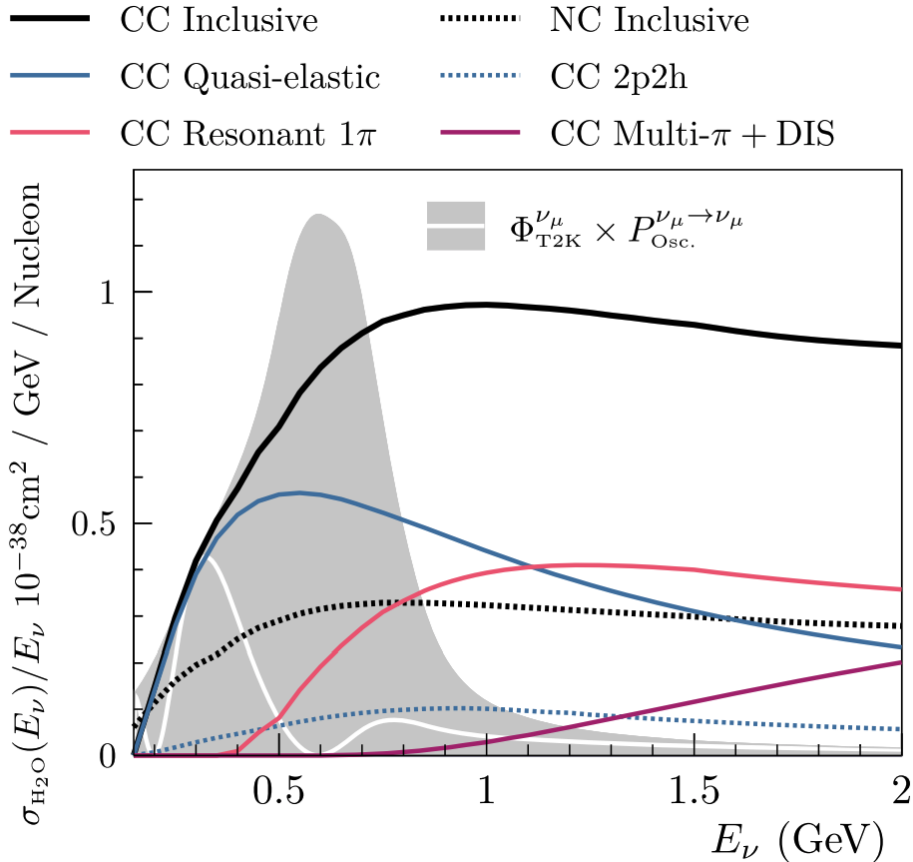


Figure 4.1: The NEUT prediction of the ν_μ -H₂O cross-section overlaid on the T2K ν_μ flux. The charged current (black, solid) and neutral current (black, dashed) inclusive, charged current quasi-elastic (blue, solid), charged current 2p2h (blue, dashed), charged current single pion production (pink), and charged current multi- π and DIS (Purple) cross-sections are illustrated. Taken from [148].

As illustrated in Figure 4.1, QE interactions dominate the low-energy cross-section of neutrino interactions. The NEUT implementation adopts the Llewellyn Smith [150] model for neutrino-nucleus interactions, where the nuclear ground state of any bound nucleons (neutrino-oxygen interactions) is approximated by a spectral-function [151] model that simulates the effects of Fermi momentum and Pauli blocking. The cross-section of QE interactions are controlled by vector and axial-vector form factors parameterised by the BBBA05 [152] model and a dipole form factor with $M_A^{QE} = 1.21 \text{ GeV}$ fit to external data [153], respectively. QE interactions only account for single-nucleon interactions whereas multi-nucleon interactions (or MEC) can contribute significantly to the overall cross-section. NEUT implements the Valencia [154] model

1244 to simulate MEC events, where two nucleons and two holes in the nuclear target are
1245 produced (Often called 2p2h interactions due to this effect).

1246 For neutrinos of energy $O(1)\text{GeV}$, PROD interactions become dominant. These
1247 predominantly produce charged and neutral pions although γ , kaon, and η production
1248 is also considered. To simulate these interactions, the Berger-Sehgal [155] model is
1249 implemented within NEUT. It simulates the excitation of a nucleon from a neutrino
1250 interaction, production of an intermediate baryon, and the consequential decay to a
1251 single meson or γ . Pions can also be produced through COH interactions, which occur
1252 when the incoming neutrino interacts with the entire oxygen nuclei target leaving a
1253 single pion outside of the nucleus. NEUT utilises the Berger-Sehgal [156] model to
1254 simulate these interactions.

1255 DIS and multi- π producing interactions become the most dominant for energies
1256 $> O(5)\text{GeV}$. PYTHIA [157] is used to simulate any interaction with invariant mass,
1257 $W > 2\text{GeV}/c^2$, which produces at least one meson. For any interaction which produces
1258 at least two mesons but has $W < 2\text{GeV}/c^2$, the Bronner model is invoked [158].
1259 Both of these models use Parton distribution functions based on the Bodek-Yang
1260 model [159–161].

1261 Any pion which is produced within the nucleus can re-interact through final state
1262 interactions before it exits, as illustrated by the scattering, absorption, production, and
1263 exchange interactions in Figure 4.2. These re-interactions alter the observable particles
1264 within the detector. For instance, if the charged pion from a CC PROD interaction
1265 is absorbed, the observables would mimic a CC QE interaction. To simulate these
1266 effects, NEUT uses a semi-classical intranuclear cascade model [148]. This cascade
1267 functions by stepping the pion through the nucleus in fixed-length steps equivalent
1268 to $dx = R_N/100$, where R_N is the radius of the nucleus. At each step, the Monte
1269 Carlo allows the pion to interact through scattering, charged exchange, absorption, or

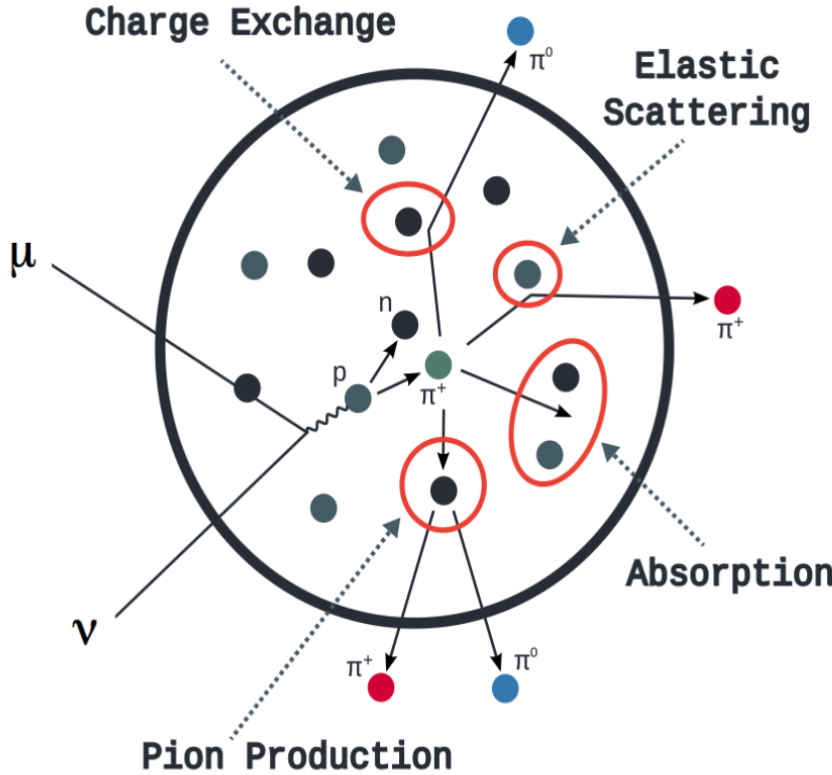


Figure 4.2: Illustration of the various processes which a pion can undergo before exiting the nucleus. Taken from [162].

1270 production with an interaction-dependent probability calculated from a fit to external
1271 data [163]. This cascade continues until the pion is absorbed or exits the nucleus.

1272 Once the outgoing particle kinematics have been determined from NEUT, they
1273 are passed into the detector simulation. The near detectors ND280 and INGRID are
1274 simulated using a GEANT4 package [107, 164] to simulate the detector geometry and
1275 particle tracking. The response of the detectors is simulated using the elecSim pack-
1276 age. The far detector simulation is based upon the original Kamiokande experiment
1277 software which uses the GEANT3-based SKDETSIM [107, 165] package. This controls
1278 the interactions of particles in the water as well as Cherenkov light production. The
1279 water quality and PMT calibration measurements detailed in subsection 2.1.2 are also
1280 used within this simulation to make accurate predictions of the detector response.

¹²⁸¹ 4.2 Event Reconstruction at SK

¹²⁸² Any above Cherenkov threshold event which occurs in SK will be recorded by the
¹²⁸³ PMT array, where each PMT records the time and accumulated charge is measured.
¹²⁸⁴ This is shown in the event displays illustrated in Figure 4.3. To be useful for physics
¹²⁸⁵ analyses, this series of PMT hit information needs to be reconstructed to determine the
¹²⁸⁶ particle’s identity and kinematics. This is because the charge and timing distribution
¹²⁸⁷ of photons generated by a particular particle in an event is dependent upon its initial
¹²⁸⁸ vertex position, time, direction, and momentum of the particle.

¹²⁸⁹ For the purposes of this analysis, the `fitQun` reconstruction algorithm is utilised.
¹²⁹⁰ Its core function is to compare a prediction of the accumulated charge and timing
¹²⁹¹ distribution from each PMT, generated for a particular particle hypothesis, to that
¹²⁹² observed in the neutrino event. It determines the best particle hypothesis by min-
¹²⁹³ imising a likelihood function which includes information from PMTs which were hit
¹²⁹⁴ and those that were not hit. This improves upon the `APFit` reconstruction algorithm
¹²⁹⁵ which has been used for many previous SK analyses. `APFit` only includes information
¹²⁹⁶ from PMTs within the 43 deg Cherenkov cone and then sequentially fits the kinematic
¹²⁹⁷ parameters and particle configuration. Conversely, `fitQun` performs a simultaneous
¹²⁹⁸ fit, improving both the accuracy of the fit parameters and the rejection of neutral
¹²⁹⁹ current π^0 events [166, 167]. The `fitQun` algorithm is based on the key concepts
¹³⁰⁰ on the MiniBooNE reconstruction algorithm [168] and is described in [169] which is
¹³⁰¹ summarised below.

¹³⁰² An event in SK can consist of multiple “sub-events”. For example, a muon neutrino
¹³⁰³ interaction will generate a muon which will subsequently decay into an electron.
¹³⁰⁴ Both the muon and electron can generate Cherenkov photons but both subevents
¹³⁰⁵ need to be reconstructed separately. Therefore, to avoid assigning photons generated

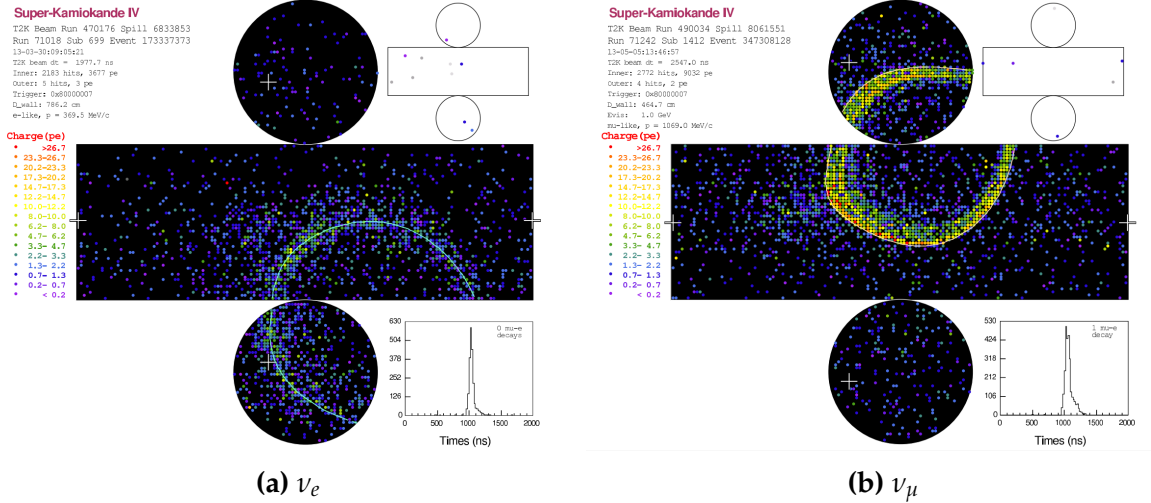


Figure 4.3: Event displays from Super Kamiokande illustrating the “crisp” ring from a muon and the typically “fuzzy” electron ring. Each pixel represents a PMT and the color scheme denotes the accumulated charge deposited on that PMT. Figures taken from [170].

1306 by the decay-electron to the muon, each event is divided into time clusters, termed
 1307 “subevents”, where subevent is defined to contain at most one hit for each PMT. To
 1308 find the subevents, a vertex goodness metric is calculated for some vertex position \vec{x}
 1309 and time t ,

$$G(\vec{x}, t) = \sum_i^{\text{hit PMTs}} \exp \left(-\frac{1}{2} \left(\frac{T_{Res}^i(\vec{x}, t)}{\sigma} \right)^2 \right) \quad (4.1)$$

1310 where

$$T_{Res}^i(\vec{x}, t) = t_i - t - |R_{PMT}^i - \vec{x}| / c_n \quad (4.2)$$

1311 is the residual hit time, R_{PMT}^i is the position of the i^{th} PMT, c_n is the speed of light in
 1312 water and $\sigma = 4\text{ns}$ which is comparable to the time resolution of the PMT. When the fit

values of time and vertex are close to the true values, $T_{Res}^i(\vec{x}, t)$ tends to zero resulting in subevents appearing as spikes in the goodness metric. The fit vertex and time are grid-scanned, and the values which maximise the goodness metric are selected as the “pre-fit vertex”. Whilst this predicts a vertex for use in the clustering algorithm, the final vertex is fit using the higher-precision maximum likelihood method described below.

Once the pre-fit vertex has been determined, the goodness metric is scanned as a function of t to determine the number of delayed peaks. A peak-finding algorithm is then used on the goodness metric, requiring the goodness metric to exceed some threshold and drop below a reduced threshold before any delayed additional peaks are considered. The thresholds are set such that the rate of false peak finding is minimised while still attaining good data to Monte Carlo agreement. To improve performance, the pre-fit vertex for each delayed subevent is re-calculated after PMT hits from the primary subevent are masked. This improves the decay-electron tagging performance. Once all subevents have been determined, the time window around each subevent is then defined by the earliest and latest time which satisfies $-180 < T_{Res}^i < 800\text{ns}$. The subevents and associated time windows are then used as seeds for further reconstruction.

For a given subevent, `fiTQun` constructs a likelihood based on the accumulated charge q_i and time information t_i from the i^{th} PMT,

$$L(\Gamma, \vec{\theta}) = \prod_j^{\text{unhit}} P_j(\text{unhit}|\Gamma, \vec{\theta}) \prod_i^{\text{hit}} \{1 - P_i(\text{unhit}|\Gamma, \vec{\theta})\} f_q(q_i|\Gamma, \vec{\theta}) f_t(t_i|\Gamma, \vec{\theta}), \quad (4.3)$$

where $\vec{\theta}$ defines the track parameters; vertex position, direction vector and momenta, and Γ represents the particle hypothesis. $P_i(\text{unhit}|\Gamma, \vec{\theta})$ defines the probability

₁₃₃₅ of the i^{th} tube to not register a hit given the track parameters and particle hypothesis.
₁₃₃₆ The charge likelihood, $f_q(q_i|\Gamma, \vec{\theta})$, and time likelihood, $f_t(t_i|\Gamma, \vec{\theta})$, represent the probability density function of observing charge q_i and time t_i on the i^{th} PMT given track parameters $\vec{\theta}$ and particle hypothesis Γ .

₁₃₃₉ As the generation and propagation of the optical photons are independent of the
₁₃₄₀ PMT and electronics response, it is natural to split the calculation into two. Firstly,
₁₃₄₁ calculating the expected number of photoelectrons (or predicted charge), μ_i , at the
₁₃₄₂ i^{th} PMT, and then calculating the likelihood based on this value. This substitution
₁₃₄₃ allows the charge likelihood density $f_q(q_i|\mu_i)$ and unhit probability $P_i(\text{unhit}|\mu_i)$ to be
₁₃₄₄ expressed via quantities that are only dependent on the response of the PMT.

₁₃₄₅ The predicted charge is calculated based on contributions from both the direct
₁₃₄₆ light and the scattered light. The direct light contribution is determined based on the
₁₃₄₇ integration of the Cherenkov photon profile along the track. PMT angular acceptance
₁₃₄₈ and water quality and calibration measurements discussed in subsection 2.1.2 are
₁₃₄₉ included to accurately model the detector's response. The scattered light is calculated
₁₃₅₀ in a similar way although it includes a scattering function that depends on the vertex
₁₃₅₁ of the particle and the position of the PMT. The charge likelihood is calculated by
₁₃₅₂ comparing the prediction to the observed charge in the PMT, where the prediction
₁₃₅₃ assumes photoelectron generation obeys a Poisson distribution.

₁₃₅₄ The time likelihood is approximated to depend on the vertex \vec{x} , direction \vec{d} , and
₁₃₅₅ time t of the track parameters as well as the particle hypothesis. The expected time
₁₃₅₆ for PMT hits is calculated by assuming unscattered photons being emitted from the
₁₃₅₇ midpoint of the track, S_{mid} ,

$$t_i^{exp} = t + S_{mid}/c + |R_{PMT}^i - \vec{x} - S_{mid}\vec{d}|/c_n, \quad (4.4)$$

where c is the speed of light in a vacuum. The time likelihood is then expressed in terms of the residual difference between the PMT hit time and the expected hit time, $t_i^{Res} = t_i - t_i^{exp}$. As the first photon hit defines the PMT hit time, the time likelihood density profile is narrower for higher momenta particles which introduces a dependence on the predicted charge. The particle hypothesis and momentum also affect the Cherenkov photon distribution which modifies the shape of the time likelihood density since in reality not all photons are emitted at the midpoint of the track. As with the charge likelihood, the contributions from both the direct and scattered light to the time likelihood density are calculated separately, which are both calculated from particle gun studies.

The track parameters, $\vec{\theta}$, which maximise $L(\Gamma|\vec{\theta})$ are defined the best fit parameters. In practice MINUIT [171] is used to minimise the value of $-\ln L(\Gamma, \vec{\theta})$. The particle hypothesis is determined by the comparison of $L(\Gamma, \vec{\theta})$ across all viable hypotheses, Γ . The fit considers an electron-like, muon-like, and charged pion-like hypothesis. The particle's identity is determined by taking the ratio of the likelihood of each of the hypotheses. For instance, electrons and muons are distinguished by considering the value of $\ln(L_e/L_\mu)$ as illustrated in Figure 4.4.

Alongside the three hypotheses which have a single final state particle generating optical photons, denoted “single-ring” particle hypotheses, the `fitQun` algorithm also considers a π^0 hypothesis. To do this, it performs a fit looking for two standard electron-hypothesis tracks which point to the same vertex position and time. This assumes the electron tracks are generated from photon-conversion so the electron tracks actually appear offset from the proposed π^0 vertex. For these fits, the conversion length, direction, and momenta of each photon are also considered as track parameters which are then fit in the same methodology as the standard single-ring hypotheses.

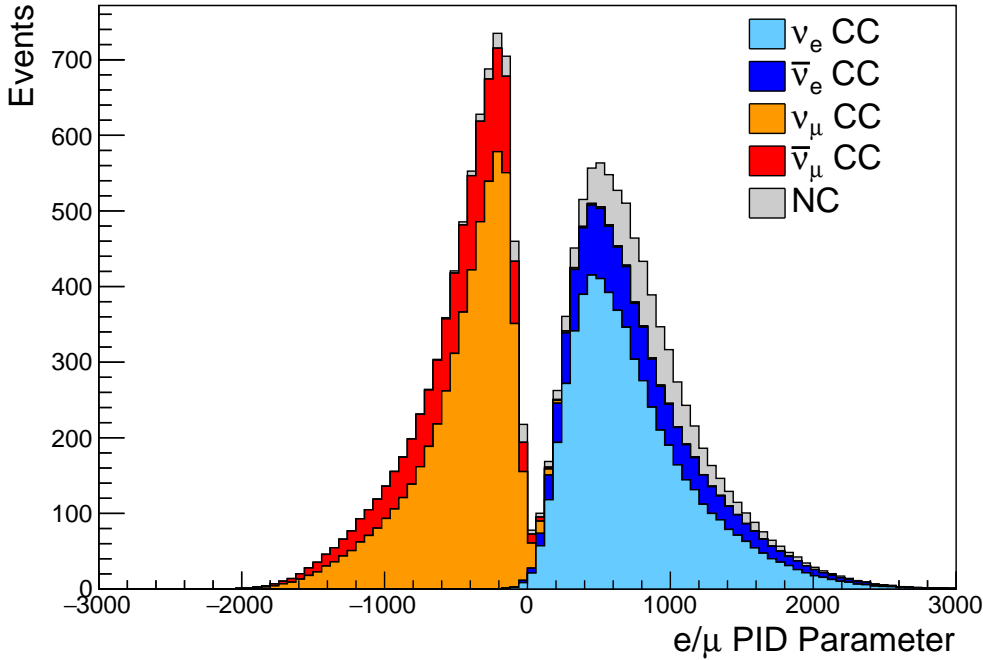


Figure 4.4: The electron/muon PID separation parameter for all sub-GeV single-ring events in SK-IV. The charged current (CC) component is broken down in four flavours of neutrino ($\nu_\mu, \bar{\nu}_\mu, \nu_e$ and $\bar{n}u_e$). Events with positive values of the parameter are determined to be electron-like.

The previous discussion pertains to a single final state particle that generates optical photons. However, the higher energy atmospheric neutrino events can generate final states with multiple particles which generate Cherenkov photons. These “multi-ring” hypotheses are also considered in the `fitQun` algorithm, but only for the first subevent in each ring to reduce computational cost. When calculating the charge likelihood density, the predicted charge associated with each ring is calculated separately and then merged to calculate the total accumulated charge on each PMT. Similarly, the time likelihood for the multi-ring hypothesis is calculated assuming each ring is independent. However, each track is then time-ordered based on the time of flight from the center of the track to the PMT, and the direct light from any ring incident on the PMT arrives before any scattered light. To reduce computational resources required for a fit, the multi-ring fits only consider electron-like and charged pion-like rings as the pion fit can be used as a proxy for a muon fit due to their similar mass.

1396 Typically, multi-ring fits have the largest likelihood because of the additional
 1397 degrees of freedom introduced. Multi-ring fits proceed by proposing another ring
 1398 to the previous fit and then fitting the parameters in the method described above.
 1399 The additional ring is only added if the ratio of likelihoods between the n and $n + 1$
 1400 passes the criteria. The criteria values for single-ring and multi-ring separation have
 1401 been determined to be 9.35(11.83) based on Monte-Carlo studies, for hypotheses with
 1402 electron-like(muon-like) the first ring.

1403 As an example of how the reconstruction depends on the detector conditions, the
 1404 author of this thesis assessed the quality of event reconstruction for SK-V data. The
 1405 detector systematics invoked within the T2K-only oscillation analysis are determined
 1406 using data to Monte Carlo comparisons using the SK-IV data [172]. Due to tank-open
 1407 maintenance occurring between SK-IV and SK-V, the dark rate of each PMT was
 1408 observed to increase due to light exposure for a significant time during the repairs.
 1409 This can be seen in Figure 4.5. Run-10 of the T2K experiment was conducted in the SK-
 1410 V period, so the consistency of SK-IV and SK-V data needs to be studied to determine
 1411 whether the SK-IV defined systematics can be applied to the run-10 data. This study
 1412 was performed using the stopping muon data set for both the SK-IV and SK-V periods.
 1413 This data is used due to the high rate of interactions, $O(200)$ events per hour, as well
 1414 as having similar energies to muons from CCQE ν_μ interactions. The rate of cosmic
 1415 muons does depend on the solar activity cycle [173]. This has been neglected in this
 1416 comparison study as it is the shape of the distributions which is important for the
 1417 purposes of being compared to the detector systematics. 2398.42 and 626.719 hours of
 1418 SK-IV and SK-V are used which equates to 686743 and 192504 events respectively.

1419 The predicted charge used in the `fitQun` charge likelihood calculation for each
 1420 PMT includes the photoelectron emission contribution from the dark rate of the PMT.
 1421 Therefore, the increase in the dark rate needs to be accounted for. In practice, the

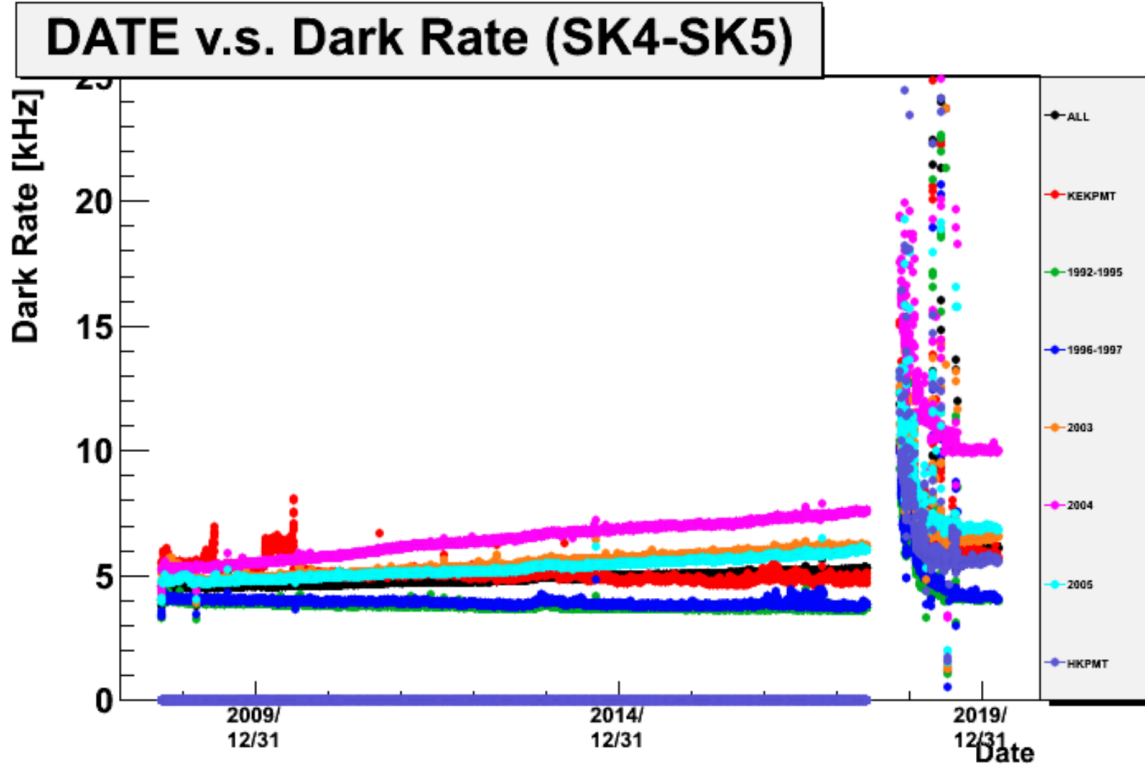


Figure 4.5: The variation of the measured dark rate as a function of date, broken down by PMT type. The SK-IV and SK-V periods span September 2008 to May 2018 and January 2019 to July 2020 respectively. The break in measurement between 2018 corresponds to the period of tank repair and refurbishment. Figure adapted from [172].

reconstruction algorithm takes the average dark rate for all PMTs for each SK period as an input and predicts the associated charge from this contribution. The dark rate was calculated by averaging the dark rate per run for each period separately, using the calibration measurements detailed in subsection 2.1.2. The average dark rate from SK-IV and SK-V were found to be 4.57kHz and 6.30kHz , respectively. The associated charge with the muon and decay electron subevents are illustrated in Figure 4.6. As expected, the increase in dark rate is not observed in the muon subevent which is of typically higher energy. However, it has a clear effect on the decay electron subevent which is lower energy.

The energy scale systematic for the SK-IV period was determined to be 2.1% [174]. It is defined to be equal to the difference between data and Monte Carlo prediction

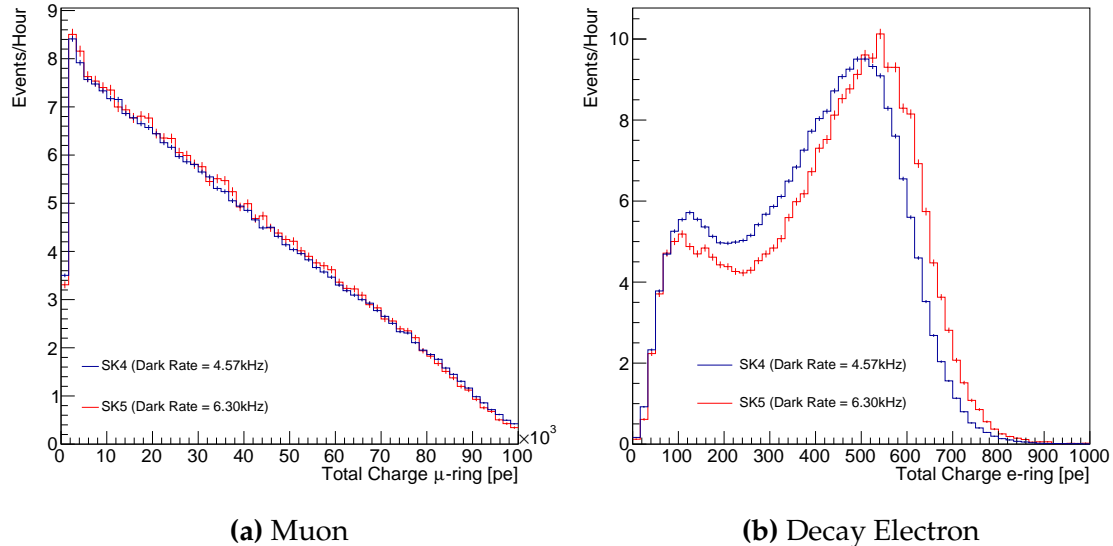


Figure 4.6: Comparison of the measured raw charge deposited per event from the stopping muon data samples between SK-IV (Blue) and SK-V (Red), split by the primary muon subevent and the associated decay electron subevent.

in the stopping muon data sample. To determine the consistency of the SK-IV and SK-V with respect to the energy scale systematic, the muon momentum distribution is compared between the two SK periods. The distribution of Cherenkov photons is dependent upon the momentum of the particle. This is then integrated along the track length of the particle to determine the PMT hit probability for each PMT. Consequently, the reconstructed momentum divided by track length is compared between SK-IV and SK-V as illustrated in Figure 4.7.

The consistency between these distributions has been computed in two ways.

Firstly, a Gaussian is fit to each distribution separately. The mean of which is found to be $(2.272 \pm 0.003)\text{MeV/cm}$ and $(2.267 \pm 0.006)\text{MeV/cm}$ for SK-IV and SK-V respectively. The ratio of these is equal to 1.002 ± 0.003 . The mean of the Gaussian's is consistent with the expected stopping power of a minimum ionising muon for a target material (water) with $Z/A \sim 0.5$ [175]. The second consistency check is performed by introducing a nuisance parameter, α , which modifies the SK-V distribution. The value of α which minimises the χ^2 between the SK-IV and SK-V is determined by

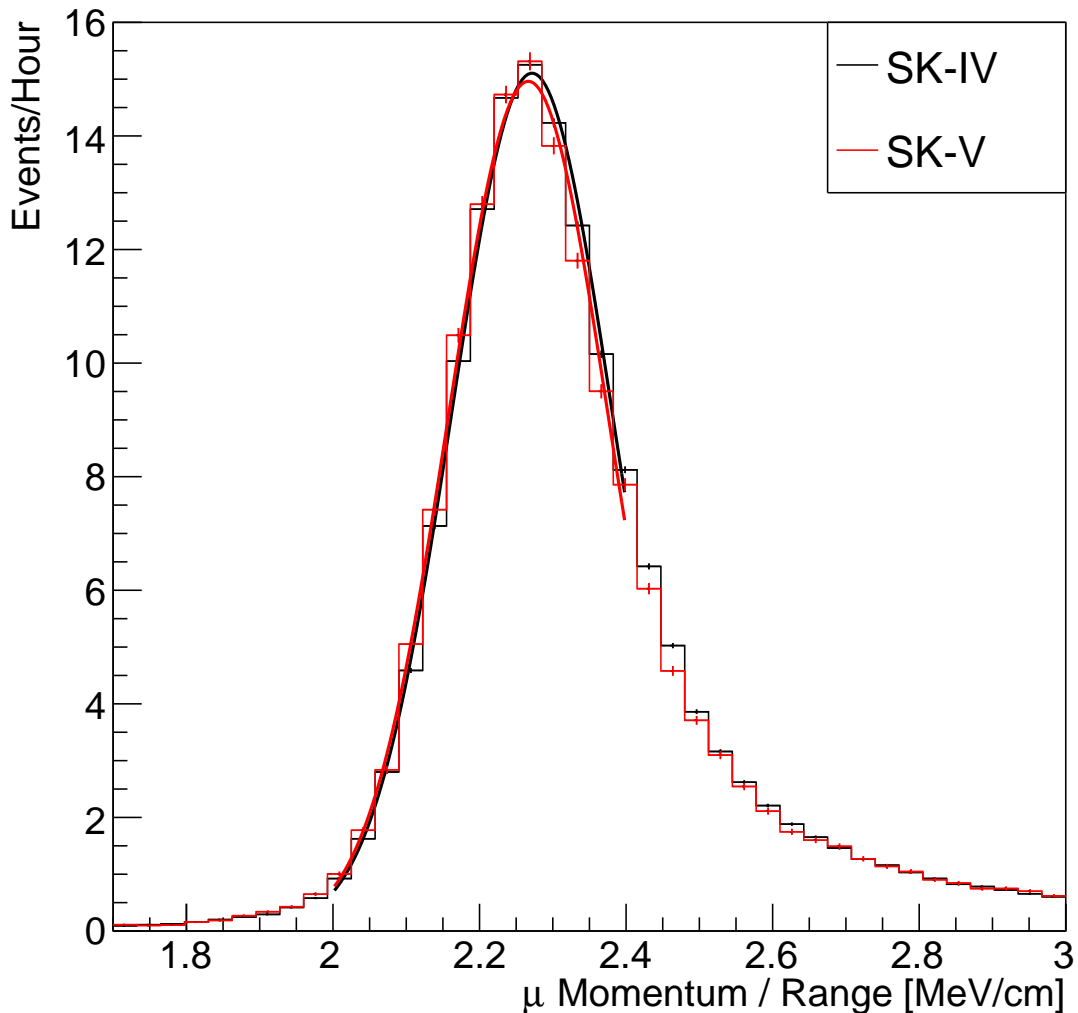


Figure 4.7: The distribution of the reconstructed momentum from the muon ring divided by the distance between the reconstructed muon and decay electron vertices as found in the stopping muon data sets of SK-IV (Black) and SK-IV (Red). Only events with one tagged decay electron and considered. A Gaussian fit is considered in the range [2.0, 2.4] MeV/cm and illustrated as the solid curve.

scanning across a range of values. This is repeated by applying α as a multiplicative factor and an additive shift. The χ^2 distributions for different values of α is illustrated in Figure 4.8. The values which minimise the χ^2 are found to be 0.0052 and 1.0024 for the additive and multiplicative implementations respectively. No evidence of shifts larger than the 2.1% uncertainty on the energy scale systematic has been found in the reconstructed momentum distribution of SK-IV and SK-V.

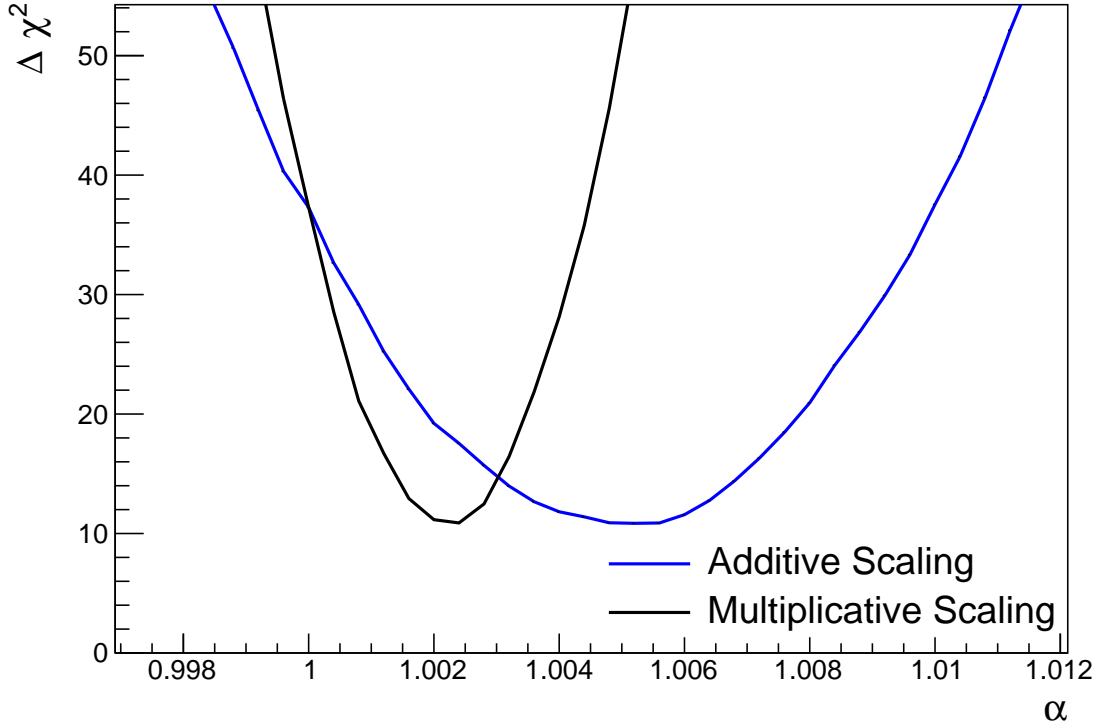


Figure 4.8: The χ^2 difference between the SK-IV and SK-V reconstructed muon momentum divided by range when the SK-V is modified by the scaling parameter α . Both additive (Blue) and multiplicative (Black) scaling factors have been considered. In practice, the additive scaling factor actually uses the value of $(\alpha - 1.0)$.

¹⁴⁵⁴ 4.3 Event Selection at SK

¹⁴⁵⁵ Atmospheric neutrino events observed in the SK detector are categorised into three
¹⁴⁵⁶ different types of samples; fully contained (FC), partially contained (PC) and up-
¹⁴⁵⁷ going muon (Up- μ), using signatures in the inner and outer detector (ID and OD,
¹⁴⁵⁸ respectively). To identify FC neutrino events, it is required that the neutrino interacts
¹⁴⁵⁹ inside the fiducial volume of the ID such that no significant OD activity is observed.
¹⁴⁶⁰ For this analysis, an event is defined to be in the fiducial volume providing the
¹⁴⁶¹ event vertex is at least 0.5m away from the ID walls. PC events have the same ID
¹⁴⁶² requirements but can have a larger signal present inside the OD. Typically these events
¹⁴⁶³ are higher energy muon interactions that penetrate the ID walls. The Up- μ sample

¹⁴⁶⁴ contains events where muons are created in the OD water or rock below the tank
¹⁴⁶⁵ and then propagate upwards through the detector. The reason downward-going
¹⁴⁶⁶ muons generated from neutrino interactions above the tank are neglected is due to
¹⁴⁶⁷ the difficulty in separating their signature from the cosmic muon shower background.
¹⁴⁶⁸ The sample categories are visually depicted in Figure 4.9.

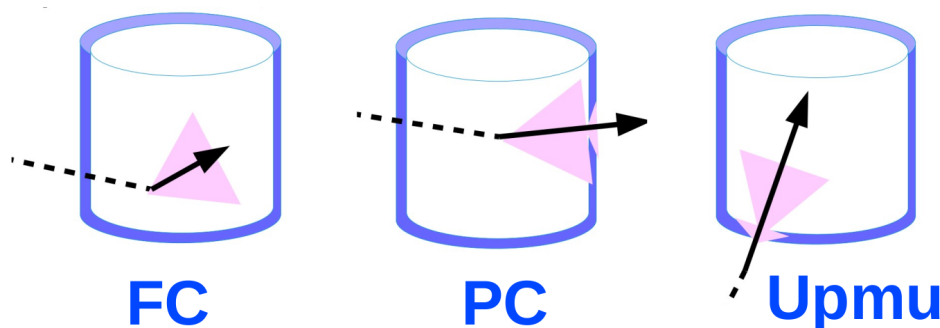


Figure 4.9: A depiction of the topology patterns for fully-contained (FC), partially-contained (PC) and up-going muon ($\text{Up-}\mu$) samples included in this analysis.

¹⁴⁶⁹ Based on the event characteristics as defined by the `fitQun` event reconstruction
¹⁴⁷⁰ software, the FC events are further divided up by

- ¹⁴⁷¹ • **Visible Energy:** equal to the sum of the reconstructed kinetic energy above the
¹⁴⁷² Cerenkov threshold for all rings present in the event. The purpose is to separate
¹⁴⁷³ events into sub-GeV and multi-GeV categories.
- ¹⁴⁷⁴ • **Number of observed Cerenkov rings.** The purpose is to separate single-ring and
¹⁴⁷⁵ multi-ring events, where single-ring events predominantly consist of quasi-elastic
¹⁴⁷⁶ interactions and multi-ring events are resonant pion production or deep inelastic
¹⁴⁷⁷ scattering events.
- ¹⁴⁷⁸ • **Particle identification parameter of the most energetic ring:** A value deter-
¹⁴⁷⁹ mined from the maximum likelihood value based on `fitQun`'s electron, muon, or
¹⁴⁸⁰ pion hypothesis. The purpose is to separate electron-like and muon-like events.

- **Number of sub-events:** Based on optimised time cuts, this quantity determines the number of observed decay electrons associated with an event. The main purpose is to separate quasi-elastic events (which have one decay electron emitted from the muon decay) and resonant pion production events (which have two decay electrons emitted from the muon and pion).

The PC and Up- μ categories are broken down into “through-going” and “stopping” samples depending on whether the muon left the detector. This is because the stopping events deposited the entire energy of the interaction into the detector, resulting in better reconstruction. Through-going Up- μ samples are further broken down by whether any hadronic showering was observed in the event which would be mostly likely due to DIS interactions. The expected neutrino energy for the different categories is given in Figure 4.10. FC sub-GeV and multi-GeV events peak around 0.7GeV and 3GeV respectively, with slightly different peak energies for $\nu_x \rightarrow \nu_e$ and $\nu_x \rightarrow \nu_\mu$. PC and Up- μ are almost entirely comprised of $\nu_x \rightarrow \nu_\mu$ events and peak around 7GeV and 100GeV respectively.

In data-taking operation, the SK detector observes many background events alongside the beam and atmospheric neutrino signal events of physics interest. Cosmic ray muons and flasher events, which is the spontaneous discharge of a given PMTm contribute the largest amount of background events in the energy range relevant to oscillation analyses. Lower energy analyses like DSNB searches are also subject to radioactive backgrounds [176]. Therefore the data recorded is reduced with the aim of removing these background events. The reduction process is detailed in [44, 81] and briefly summarised below.

The first two steps in the FC reconstruction remove most cosmic ray muons by requiring a significant amount of ID activity compared to that measured in the OD. This is done by counting the total number of photoelectrons recorded in the ID as

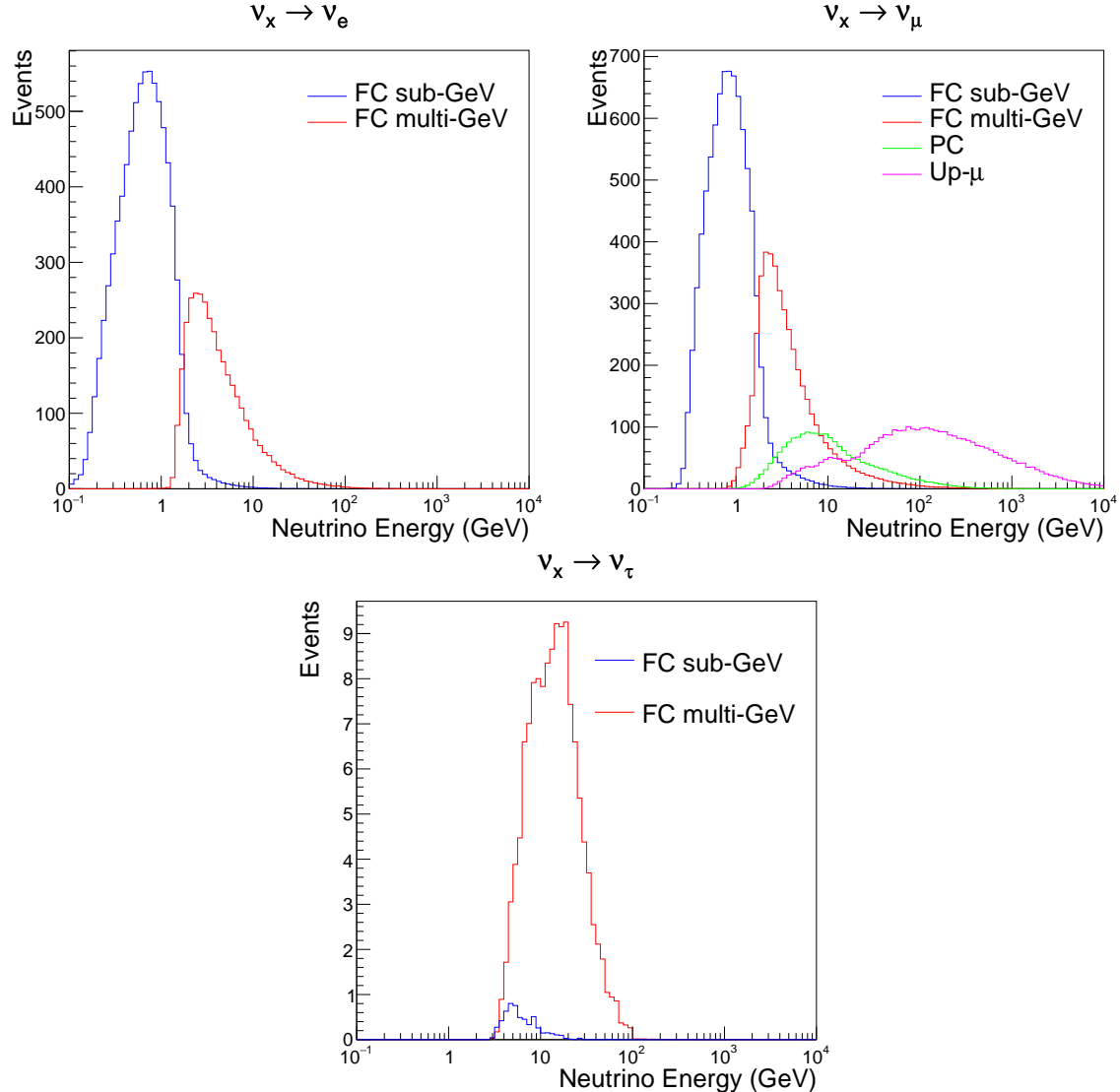


Figure 4.10: The predicted neutrino flux of the fully contained (FC) sub-GeV and multi-GeV, partially contained (PC) and upward-going muon (Up- μ) events. The prediction is broken down by the $\nu_x \rightarrow \nu_e$ prediction (top left), $\nu_x \rightarrow \nu_\mu$ prediction (top right) and $\nu_x \rightarrow \nu_\tau$ prediction (bottom). All systematic dials are set to their nominal values and the Asimov A oscillation parameters are assumed.

well as the number of hits in the OD. A third reduction step is then applied to select cosmic-ray muons that pass the initial reduction. These are typically high momentum muons or events which leave only a small number of hits in the OD. A purpose-built cosmic muon fitter is used to determine the entrance (or exit) position of the muon from the OD and a cut is applied to OD activity contained within 8m of this position. Flasher events are removed in the fourth reduction step which is based on the close

1513 proximity of PMT hits surrounding the PMT producing the flash. Events that pass the
1514 reduction stage to this point are reconstructed using the more accurate APFit algorithm
1515 and the fifth step of the reduction uses the information from this more accurate fitter
1516 to repeat the third and fourth reduction steps using tighter cuts. This particularly
1517 targets invisible muons which are below the Cherenkov threshold resulting in no
1518 OD activity but whose decay electrons generate light inside the ID. The final cuts
1519 require the event vertex to be within the fiducial volume (0.5m from the wall although
1520 the nominal distance is 2.0m), visible energy $E_{vis} > 30\text{MeV}$ and fewer than 16 hits
1521 within the higher energy OD cluster. The culmination of the fully contained reduction
1522 results in 8.09 events/day in the nominal fiducial volume [177]. The uncertainty in the
1523 reconstruction is calculated by comparing Monte Carlo prediction to data. The largest
1524 discrepancy is found to be 1.3% in the fourth reduction step.

1525 The PC and Up- μ events are also processed through their own reduction processes
1526 detailed in [44]. Both of these samples are reconstructed with the APFit algorithm
1527 rather than `fiTQun`. This is because the efficiency of reconstructing events that leave
1528 the detector has not been sufficiently studied for reliable systematic uncertainties. 0.66
1529 and 1.44 events/day are found after the final step of reduction for the PC and Up- μ
1530 samples respectively.

₁₅₃₁ **Chapter 5**

₁₅₃₂ **Oscillation Probability Calculation**

₁₅₃₃ The calculation of the oscillation probability is crucial to the reliability of the sensitivity
₁₅₃₄ measurements of the analysis presented within this thesis. Firstly, it is important to
₁₅₃₅ understand how and where the sensitivity to the oscillation parameters comes from
₁₅₃₆ for both atmospheric and beam samples. An overview of how these sets of samples
₁₅₃₇ observe changes in δ_{CP} , Δm_{23}^2 , and $\sin^2(\theta_{23})$ as well as how the atmospheric samples
₁₅₃₈ have an increased sensitivity to mass hierarchy determination is given in section 5.1.
₁₅₃₉ It also explains the additional complexities involved when including atmospheric
₁₅₄₀ neutrinos as compared to a beam-only analysis.

₁₅₄₁ Without additional techniques, atmospheric sub-GeV upward-going neutrinos can
₁₅₄₂ artificially inflate the sensitivity to δ_{CP} due to the quickly varying oscillation probabil-
₁₅₄₃ ity in this region. Therefore, a “sub-sampling” approach has been developed to reduce
₁₅₄₄ these biases ensuring accurate and reliable sensitivity measurements. This technique
₁₅₄₅ ensures that small-scale unresolvable features of the oscillation probability have been
₁₅₄₆ averaged over whilst the large-scale resolvable features in the oscillation probability
₁₅₄₇ have been kept. The documentation of this technique is found in section 5.2 alongside
₁₅₄₈ the validation of the choices which have been made. The CUDAProb3 implementation
₁₅₄₉ choice made within the fitting framework, as detailed in section 5.3, ensures that the
₁₅₅₀ analysis can be done in a timely manner.

₁₅₅₁ Whilst the beam neutrinos are assumed to propagate through a constant density
₁₅₅₂ slab of material, the density variations through the Earth result in more complex
₁₅₅₃ oscillation patterns Furthermore, the uncertainty in the electron density can modify

1554 the oscillation probability for the denser core layers of the Earth. section 5.4 details
1555 the model of the Earth used within this analysis. This includes the official SK-only
1556 methodology as well as relatively straightforward improvements that can be made to
1557 more closely approximate the PREM model. Another quirk of atmospheric neutrinos
1558 oscillation studies is that the height of production in the atmosphere is not known
1559 on an event-by-event analysis. An analytical averaging technique that approximates
1560 the uncertainty of the oscillation probability has been followed, with the author of
1561 this thesis being responsible for the implementation and validation. This technique is
1562 illustrated in section 5.5 alongside the variation in oscillation probability which would
1563 be an expected effect in the down-going and horizontal-going neutrinos.

1564 5.1 Overview

1565 The analysis presented within this thesis focuses on the determination of oscillation
1566 parameters from atmospheric and beam neutrinos. Whilst subject to the same oscil-
1567 lation probability, the way in which the two sets of samples have sensitivity to the
1568 different oscillation parameters differs quite significantly.

1569 Atmospheric neutrinos have a varying baseline, or “path length”, such that the
1570 distance each neutrino travels before interacting is dependent upon the zenith angle.
1571 Therefore the oscillation probability can be represented as a two-dimensional “oscillo-
1572 gram” as shown in Figure 5.1. For this calculation, four layers of fixed density were
1573 used to model the Earth with values taken from an approximation of the PREM model.
1574 These can be seen in the distinct discontinuities in the oscillogram as a function of the
1575 zenith angle.

1576 Another complexity of atmospheric neutrino oscillation probability calculation is
1577 the uncertainty in the height at which a neutrino was produced, termed the “produc-

tion height". Primary cosmic rays, which contribute most of the neutrino flux, can interact anywhere between the Earth's surface and ~ 50 km above that. The baseline, L , for a neutrino generated with zenith angle, θ , and production height, h , can be calculated as

$$L = \sqrt{(R_E + h)^2 - R_E^2 (1 - \cos^2(\theta))} - R_E \cos(\theta), \quad (5.1)$$

where $R_E = 6,371$ km is the Earth's radius.

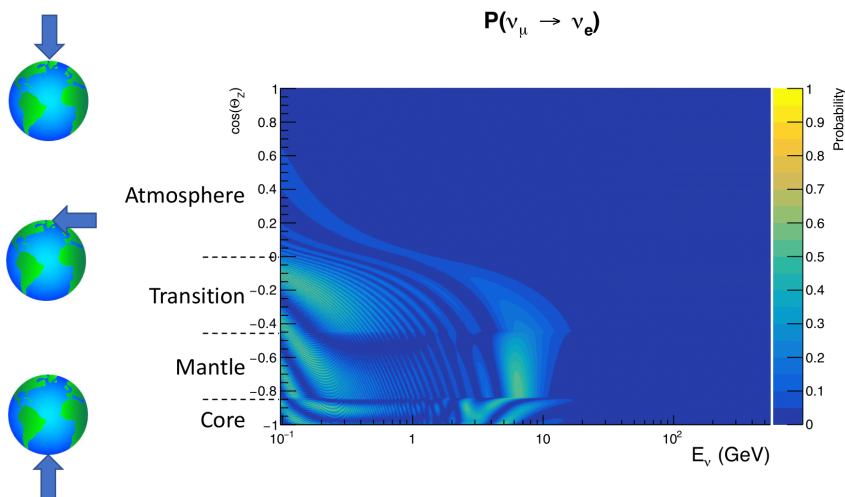


Figure 5.1: An "Oscillogram" that depicts the $P(\nu_\mu \rightarrow \nu_e)$ oscillation probability as a function of neutrino energy and cosine of the zenith angle. The zenith angle is defined such that $\cos(\theta_Z) = 1.0$ represents neutrinos that travel from directly above the detector. The four-layer constant density PREM model approximation is used and Asimov A oscillation parameters are assumed.

Atmospheric neutrinos do have some sensitivity to δ_{CP} through a normalisation term. Figure 5.2 illustrates the difference in oscillation probability between CP-conserving and CP-violating δ_{CP} values. The result is a complicated oscillation pattern in the appearance probability for sub-GeV upgoing neutrinos. The detector does not have sufficient resolution to resolve these individual patterns so the sensi-

tivity to δ_{CP} for atmospheric neutrinos comes via the overall normalisation of the sub-GeV upgoing events. The presence of matter means that the effect δ_{CP} has on the oscillation probability is not equal between neutrinos and antineutrinos which would be expected when propagating through a vacuum. This is further extenuated by the fact that SK can not distinguish neutrinos and antineutrinos well and that the cross-section neutrino interaction is larger than that for antineutrinos. Finally, sample selections (discussed in [DB: Link to selection chapter](#)) targeting different neutrino interaction modes (charge current quasi-elastic and single pion production) result in an imbalance in the percentage of neutrinos to anti-neutrinos in these samples due to pion capture. Negatively charged pions from antineutrino interactions are more likely to be captured by a nucleus compared to a positively charged pion emitted from a neutrino interaction. This all culminates in atmospheric neutrinos having a very complex sensitivity to δ_{CP} .

Atmospheric neutrinos are subject to matter effects as they travel through the dense matter in the Earth. The vacuum and matter oscillation probabilities for $P(\nu_e \rightarrow \nu_e)$ and $P(\bar{\nu}_e \rightarrow \bar{\nu}_e)$ are presented in Figure 5.3. The oscillation probability for both neutrinos and antineutrinos are affected in the presence of matter but the resonance (Effects around $E_\nu \sim 5\text{GeV}$) only occurs for neutrinos in normal mass hierarchy and antineutrinos for inverse mass ordering. The exact position and amplitude of the resonance depend on $\sin^2(\theta_{23})$ meaning that the atmospheric neutrinos have sensitivity to the octant of θ_{23} .

As the T2K beam flux is centered at the first oscillation maximum, the sensitivity to δ_{CP} is predominantly observed as a change in the event-rate of e-like samples in $\nu/\bar{\nu}$ modes. Figure 5.4 illustrates the $P(\nu_\mu \rightarrow \nu_e)$ oscillation probability for a range of δ_{CP} values. A circular modulation of the oscillation peak (in both magnitude and position) is observed when varying throughout the allowable values of δ_{CP} . The CP-

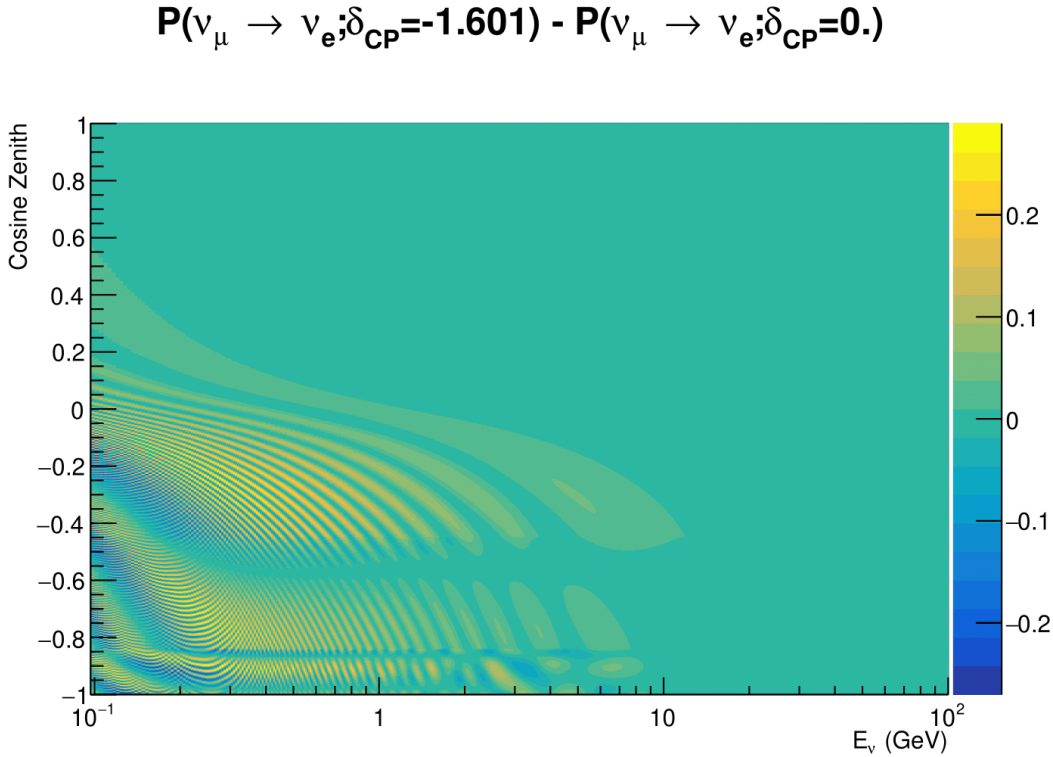


Figure 5.2: The effect of δ_{CP} for atmospheric neutrinos given in terms of the neutrino energy and zenith angle. The oscillogram compares the $P(\nu_\mu \rightarrow \nu_e)$ oscillation probability for a CP conserving ($\delta_{CP} = 0.0$) and CP violating ($\delta_{CP} = -1.601$) value of δ_{CP} . The other oscillation parameters assume the “Asimov A” oscillation parameter set given in Table 5.1.

conserving values of $\delta_{CP} = 0, \pi$ have a lower(higher) oscillation maximum than the CP-violating values of $\delta_{CP} = -\pi/2 (\delta_{CP} = \pi/2)$ leading to a $\sin(\delta_{CP})$ type sensitivity. A sub-dominant shift in the energy of the oscillation peak is also present to aid in separating the two CP-conserving values of δ_{CP} .

T2K’s sensitivity to the atmospheric oscillation parameters is more of a shape-based variation of the muon-like samples, as illustrated in Figure 5.4. The value of Δm_{32}^2 laterally shifts the position of the oscillation dip (around $E_\nu \sim 0.6$ GeV) in the $P(\nu_\mu \rightarrow \nu_\mu)$ oscillation probability. A variation of $\sin^2(\theta_{23})$ is predominantly observed as a vertical shift of the oscillation dip with second-order horizontal shifts being due to matter effects. The beam neutrinos have limited sensitivity to matter effects due

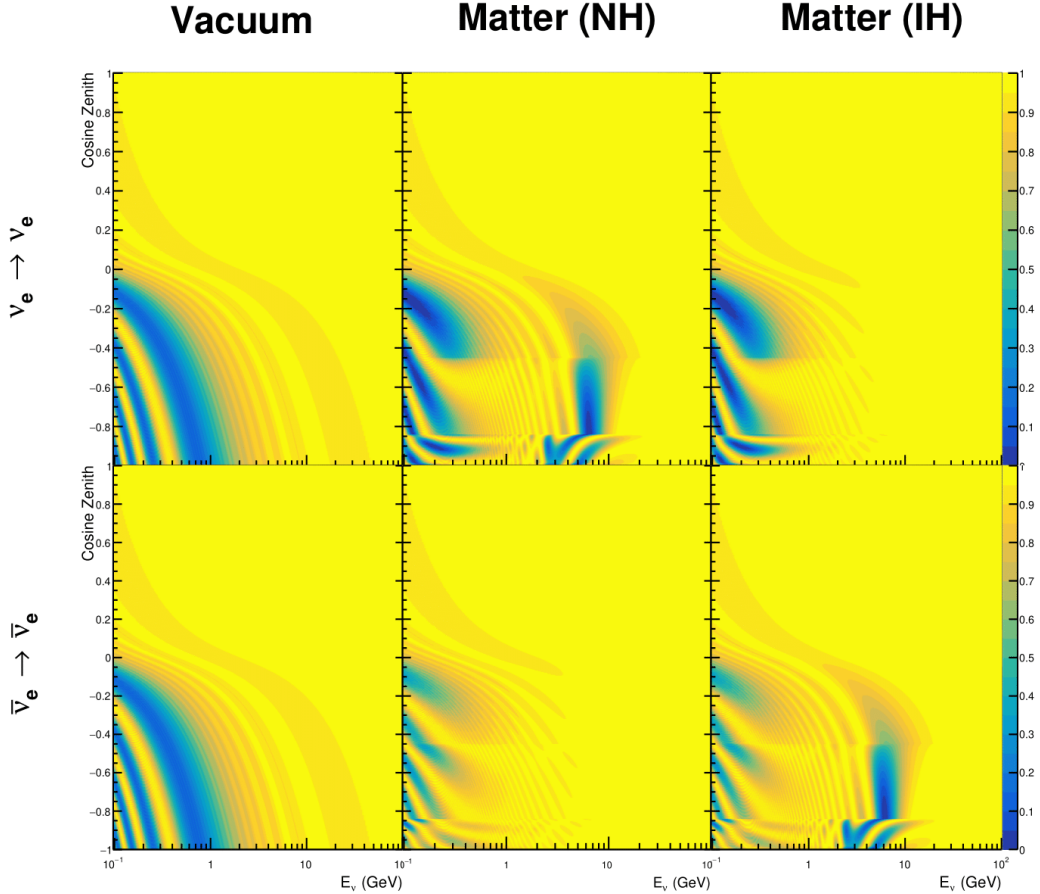


Figure 5.3: An illustration of the matter-induced effects on the oscillation probability, given as a function of neutrino energy and zenith angle. The top row of panels gives the $P(\nu_e \rightarrow \nu_e)$ oscillation probability and the bottom row illustrates the $P(\bar{\nu}_e \rightarrow \bar{\nu}_e)$ oscillation probability. The left column highlights the oscillation probability in a vacuum, whereas the middle and right column represents the oscillation probabilities when the four layer fixed density PREM model is assumed. All oscillation probabilities assume the “Asimov A” set given in Table 5.1, but importantly, the right column sets an inverted mass hierarchy. The “matter resonance” effects at $E_\nu \sim 5\text{GeV}$ can be seen in the $P(\nu_e \rightarrow \nu_e)$ for normal mass hierarchy and $P(\bar{\nu}_e \rightarrow \bar{\nu}_e)$ for inverted hierarchy.

to the shorter baseline as well as the Earth’s mantle is relatively low-density material
 (as compared to the Earth’s core). For some values of δ_{CP} , the degeneracy in the number of e-like events allows the mass hierarchy to be resolved. This leads to a δ_{CP} -dependent mass hierarchy sensitivity which can be seen in Figure 5.5.

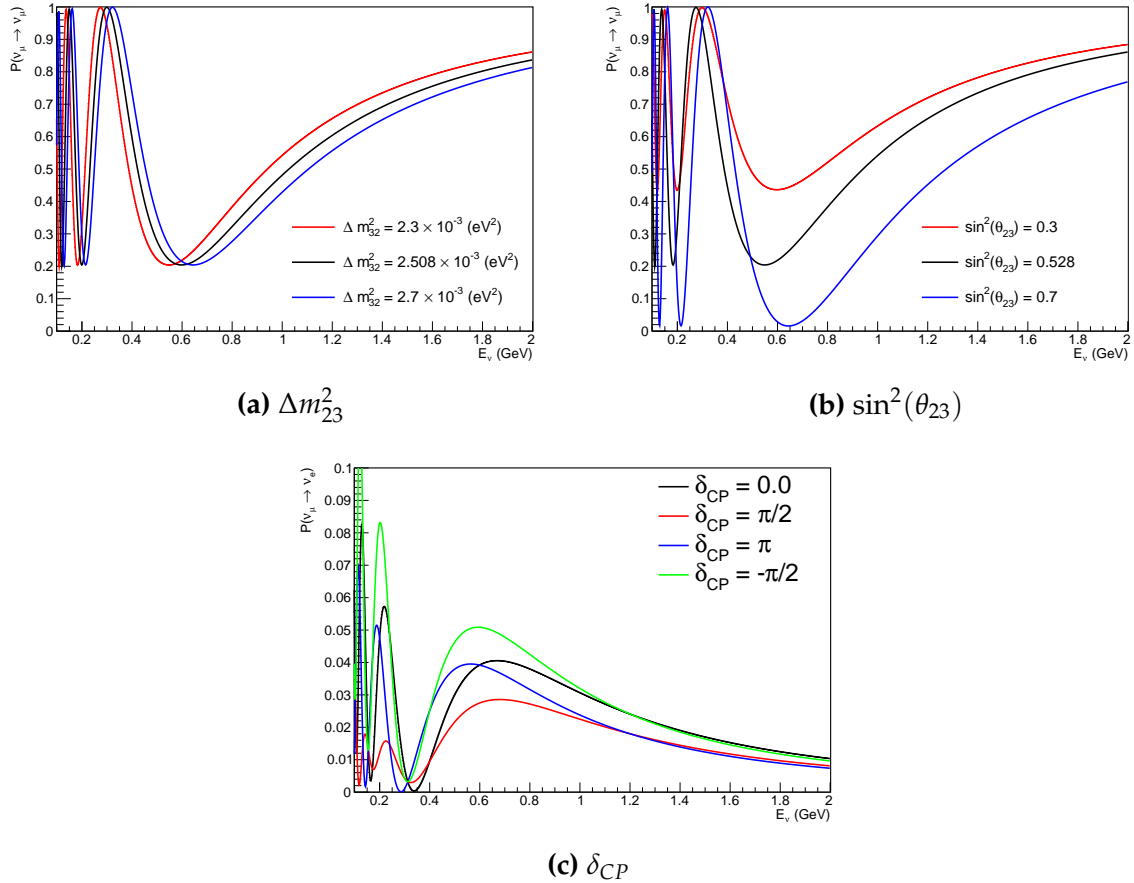


Figure 5.4: The oscillation probability for beam neutrino events given as a function of neutrino energy. All oscillation parameters assume the “Asimov A” set given in Table 5.1 unless otherwise stated. Each panel represents a change in one of the oscillation parameters whilst keeping the remaining parameters fixed.

Whilst all oscillation channels should be included for completeness, the computational resources required to run a fit are limited and any reasonable approximations which reduce the number of oscillation probability calculations that need to be made should be applied. The $\nu_e \rightarrow \nu_{e,\mu,\tau}$ (and antineutrino equivalent) oscillations can be ignored for beam neutrinos as the $\nu_e/\bar{\nu}_e$ fluxes being approximately two orders of magnitude smaller than the corresponding $\nu_\mu/\bar{\nu}_\mu$ flux. Furthermore, as the peak neutrino energy of the beam is well below the threshold for τ production ($E_\nu \sim 3$ GeV [178]) only a small proportion of the neutrinos produced in the beam have the required energy. For the few neutrinos that have sufficient energy, the oscillation probability is very small due to the short baseline. Whilst these approximations can be made for the

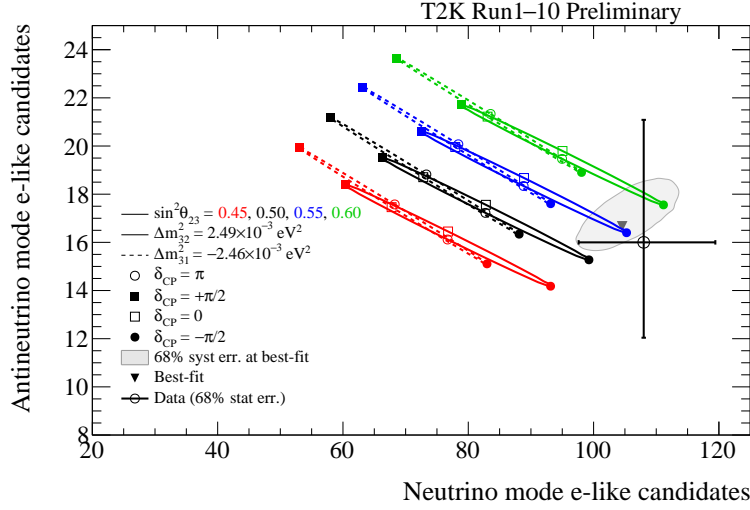


Figure 5.5: The number of electron-like events in the FHC and RHC operating mode of the beam, as a function of the oscillation probabilities. Both normal hierarchy (Solid) and inverse hierarchy (Dashed) values of Δm_{23}^2 are given.

₁₆₃₈ beam neutrinos, the atmospheric flux of ν_e is of the same order of magnitude as the ν_μ
₁₆₃₉ flux and the energy distribution of atmospheric neutrinos extends well above the tau
₁₆₄₀ production threshold.

₁₆₄₁ Throughout this thesis, several spectra predictions, Asimov fits, and contour com-
₁₆₄₂ parisons are presented which require oscillation parameters to be assumed. Table 5.1
₁₆₄₃ defines two sets of oscillation parameters, with “Asimov A” set being close to the pre-
₁₆₄₄ ferred values from a previous T2K-only fit [179] and “Asimov B” being CP-conserving
₁₆₄₅ and further from maximal θ_{23} mixing.

Parameter	Asimov A	Asimov B
Δm_{12}^2	$7.53 \times 10^{-5} \text{ eV}^2$	
Δm_{32}^2	$2.509 \times 10^{-3} \text{ eV}^2$	
$\sin^2(\theta_{12})$	0.304	
$\sin^2(\theta_{13})$	0.0219	
$\sin^2(\theta_{23})$	0.528	0.45
δ_{CP}	-1.601	0.0

Table 5.1: Reference values of the neutrino oscillation parameters for two different oscillation parameter sets.

1646 5.2 Treatment of Fast Oscillations

1647 As shown in Figure 5.6, atmospheric neutrino oscillations have a significantly more
1648 complex structure for upgoing neutrinos with energy below 1GeV. This is because the
1649 L/E dependence of the oscillation probability in this region induces rapid variations
1650 for small changes in L or E . As discussed in section 5.1, this is also the region in which
1651 atmospheric neutrinos have sensitivity to δ_{CP} . In practice, the direction between
1652 the detector and a neutrino's production vertex is inferred from the direction of any
1653 secondary particles created in the detector target. For low-energy neutrinos, this
1654 inference can be rather poor and introduces a distinct difference to beam neutrinos
1655 where the direction to production vertex is very well known.

1656 As a consequence of the poor detector resolution, an average oscillation probability
1657 is observed in this region. This creates a computational problem as a significantly
1658 large amount of MC statistics would be required to accurately predict the number
1659 of events in each bin if MC averaging was the only technique used. This section
1660 describes the 'sub-sampling' approach developed for this analysis and compares it to
1661 the methodology used within the SK-only analysis.

1662 The official SK-only analysis uses the osc3++ oscillation parameter fitter [180]. To
1663 perform the fast oscillation averaging, it uses a 'nearest-neighbour' technique. For a
1664 given neutrino MC event, the nearest neighbours in reconstructed lepton momentum
1665 and zenith angle are found and a distribution of neutrino energies is built. This
1666 distribution is then used to compute an average oscillation probability for the given
1667 neutrino MC event.

1668 For the i^{th} event, the oscillation weight is calculated as

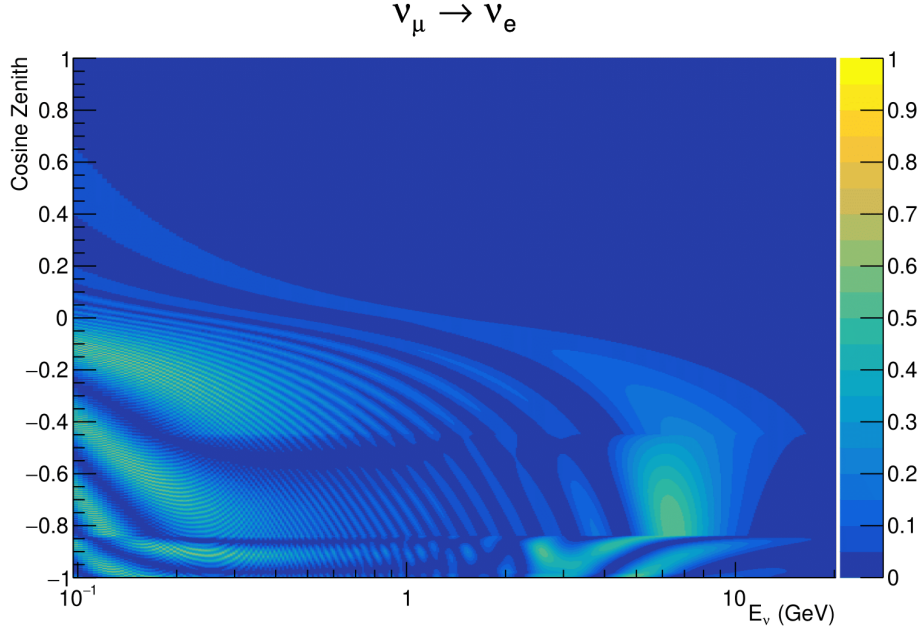


Figure 5.6: The oscillation probability $P(\nu_\mu \rightarrow \nu_e)$, given as a function of neutrino energy and zenith angle, which highlights an example of the “fast” oscillations in the sub-GeV upgoing region.

$$W_i = \frac{1}{5}P(E_i, \bar{L}_i) + \frac{1}{5} \sum_{\beta=-1,-0.5,0.5,1} P(E_i + \beta\sigma_i, L_\beta), \quad (5.2)$$

where $P(E, L)$ is the oscillation probability calculation for neutrino energy E and path length L , σ_i is the RMS of the energy distribution for the given event, and the two path lengths, \bar{L}_i and L_β are discussed below. In practice, twenty of the nearest neighbours are used to generate the neutrino energy distribution. All of the oscillation probability calculations are performed with a fixed zenith angle (and therefore have same matter density profile).

The uncertainty in the production height is controlled by using an “average” production height. \bar{L}_i represents the average path length computed using twenty production heights taken from the Honda flux model’s prediction [42] for a fixed zenith angle, where the production heights are sampled in steps of 5% of their cumulative

1679 distribution function. L_β values are similarly calculated but instead use different
1680 combinations of four production heights (sampled in the same way),

$$\begin{aligned} L_{-1.0} &= \frac{1}{4}L(45, 50, 55, 60), \\ L_{-0.5} &= \frac{1}{4}L(35, 40, 65, 70), \\ L_{+0.5} &= \frac{1}{4}L(25, 30, 75, 68), \\ L_{+1.0} &= \frac{1}{4}L(15, 20, 85, 89). \end{aligned} \tag{5.3}$$

1681 This averaging works well because of the correlation between the true neutrino
1682 zenith angle and the inferred direction from secondary particles in the detector. For
1683 low-energy neutrinos, where the resolution of the true neutrino direction is poor, σ_i
1684 will be large, resulting in significant averaging effects. Contrary to this, the inferred
1685 direction of high-energy neutrinos will be much closer to the true value, meaning that
1686 σ_i will be smaller.

1687 In practice, this technique is performed before the fit in order to deal with the
1688 computational cost. Oscillation probabilities are pre-calculated on a 4D grid. This
1689 is possible as the Osc3++ framework uses binned oscillation parameters rather than
1690 continuous so the oscillation parameters used in the fit are known prior to run-time.
1691 The framework used in the analysis presented within this thesis uses continuous
1692 oscillation parameters. Due to the MCMC technique invoked within the fitter (see
1693 chapter 3), there is no way to know which oscillation parameter values will be selected
1694 in each step at run-time. Therefore, the oscillation parameter calculation would have
1695 to be performed at run-time which is very expensive for event-by-event reweighting.
1696 Having to compute five oscillation probabilities per event would require far too many

1697 computational resources to be viable so the SK technique can not be used within this
1698 analysis. However, the concept of the averaging technique can be taken from it.

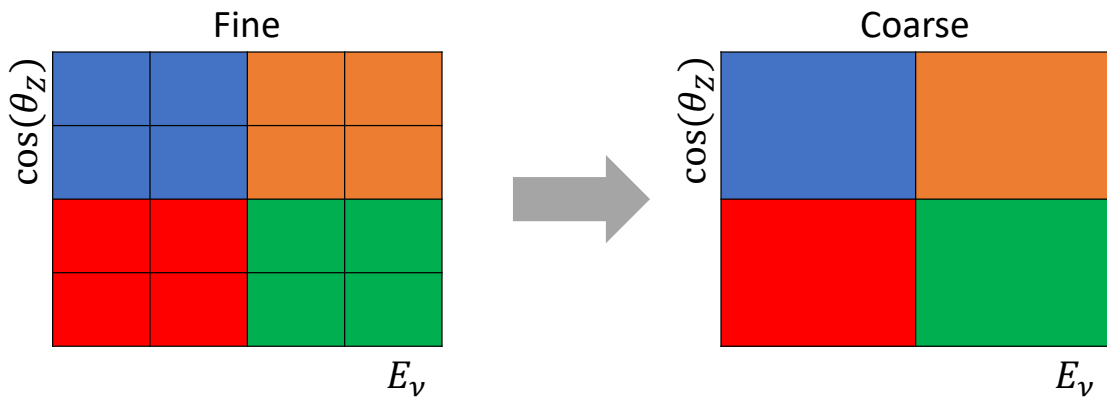


Figure 5.7: Illustration of the averaging procedure for $N = 2$. The oscillation probabilities calculated on the finer left binning are averaged to obtain the oscillation probabilities in the coarser right binning. These averaged oscillation probabilities with the coarser binning are then applied to each event during the fit.

1699 This analysis uses a binned oscillogram in which oscillation probabilities for a given
1700 event are selected based on that event's attributes. To perform a similar averaging as
1701 the SK analysis, a sub-sampling approach has been devised. The technique can be
1702 explained by considering a "fine" and "coarse" oscillogram. The fine oscillograms
1703 are used to define the array of cosine zeniths and energies for the neutrino oscillation
1704 engine. The coarse oscillograms cover the same phase-space as the fine oscillograms
1705 but have fewer bins in that range. Then, for a given coarse oscillogram bin, the value
1706 of that bin will be taken as the average of all the oscillation probabilities of all the fine
1707 oscillogram bins which fall into that coarse oscillogram bin.

1708 The binning which is used to calculate the oscillation probabilities, known as the
1709 'fine' binning, has $N \times N$ subdivisions per coarse bin. The value assigned to a coarse
1710 bin is the linear average (flat prior in E_ν and $\cos(\theta_Z)$) of all the oscillation probabilities
1711 calculated at the center of each fine bin contained within that coarse bin. Figure 5.7
1712 illustrates the $N = 2$ example where the assigned value to a coarse bin is the linear

₁₇₁₃ average of the four fine bins which fall in that coarse bin. Whilst the coarse bin edges
₁₇₁₄ are not linear on either axis, the sub-division of the fine bins is linear over the range
₁₇₁₅ of a coarse bin. The alignment of the fine and coarse binning edges is checked at
₁₇₁₆ run-time.

₁₇₁₇ The coarse binning is defined with 67×52 bins in true neutrino energy \times cosine
₁₇₁₈ zenith. In general, the binning is logarithmically spaced in neutrino energy but has
₁₇₁₉ some hand-picked bin edges. Firstly, the bin density around the matter resonance is
₁₇₂₀ smoothly increased around the matter resonance region. This is to avoid smearing
₁₇₂₁ this region which can be well sampled by the Monte Carlo. Secondly, bin edges
₁₇₂₂ are selected to hit $0.4, 0.6, 1, 10, 30, 50, 100\text{GeV}$. This is to ensure that the Coloumb
₁₇₂₃ correction systematic and the atmospheric flux systematics definitions in neutrino
₁₇₂₄ energy can be hit. The cosine zenith binning is approximately linearly spaced across
₁₇₂₅ the allowable range but the values of layer transitions are hit precisely; -0.8376
₁₇₂₆ (core-mantle) and -0.4464 (mantle/transition zone). Bins are spread further apart for
₁₇₂₇ downgoing events as this is a region unaffected by the fast oscillation wavelengths
₁₇₂₈ and reduces the total number of calculations required to perform the reweight (Not
₁₇₂₉ the number required to perform the oscillation calculation).

₁₇₃₀ The choice of N is justified based on two studies. Firstly, the variation of event
₁₇₃₁ rates of each sample is studied as a function of the number of subdivisions. For
₁₇₃₂ a given set of oscillation parameters thrown from the PDG prior constraints, the
₁₇₃₃ oscillation probabilities are calculated using a given value of N . Each sample is re-
₁₇₃₄ weighted and the event rate is stored. The value of N is scanned from 1, which
₁₇₃₅ corresponds to no averaging, to 24, which corresponds to the largest computationally
₁₇₃₆ viable subdivision binning. The event rate of each sample at large N is expected to
₁₇₃₇ converge to a stationary value due to the fine binning fully sampling the small-scale

1738 structure. Figure 5.8 illustrates this behaviour for the SubGeV_elike_0dcy sample for
 1739 30 different throws of the oscillation parameters.

SubGeV-elike-0dcy

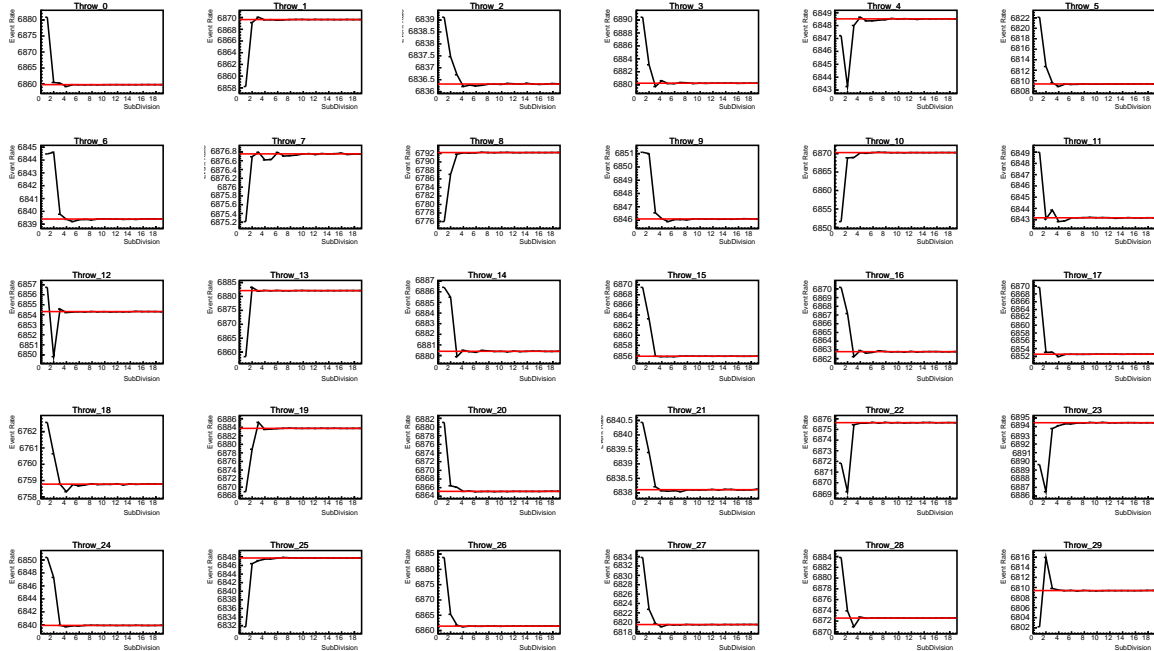


Figure 5.8: Event rate of the SubGeV_elike_0dcy sample as a function of the number of subdivisions per coarse bin. Each subplot represents the event rate of the sample at a different oscillation parameter set (thrown from the PDG priors). The red line in each subplot represents the mean of the event rate over the different values of sub-divisions for that particular oscillation parameter throw.

1740 Denoting the event rate for one sample for a given throw t at each N by $\lambda_t^{(N)}$, the
 1741 average over all considered N values ($\bar{\lambda}_t = \frac{1}{24} \sum_{N=1}^{24} \lambda_t^{(N)}$) is computed. The variance
 1742 in the event rate at each N is then calculated from

$$\text{Var}[\lambda^{(N)}] = \frac{1}{N_{\text{throws}}} \sum_{t=1}^{N_{\text{throws}}} \left(\lambda_t^{(N)} - \bar{\lambda}_t \right)^2 - \left[\frac{1}{N_{\text{throws}}} \sum_{t=1}^{N_{\text{throws}}} \left(\lambda_t^{(N)} - \bar{\lambda}_t \right) \right]^2. \quad (5.4)$$

1743 The aim of the study is to find the lowest value of N such that this variance is
 1744 below 0.001. This is the typical threshold used by T2K fitters to validate systematic
 1745 implementation so is just as applicable to the oscillation probability calculation. The
 1746 results of this study for each atmospheric sample used within this thesis are illustrated
 1747 in Figure 5.9 for 2000 throws of the oscillation parameters. As can be seen, the variance
 1748 is below the threshold at $N = 10$, and is driven primarily by the SubGeV_mulike_1dcy
 1749 and SubGeV_elike_0dcy selections.

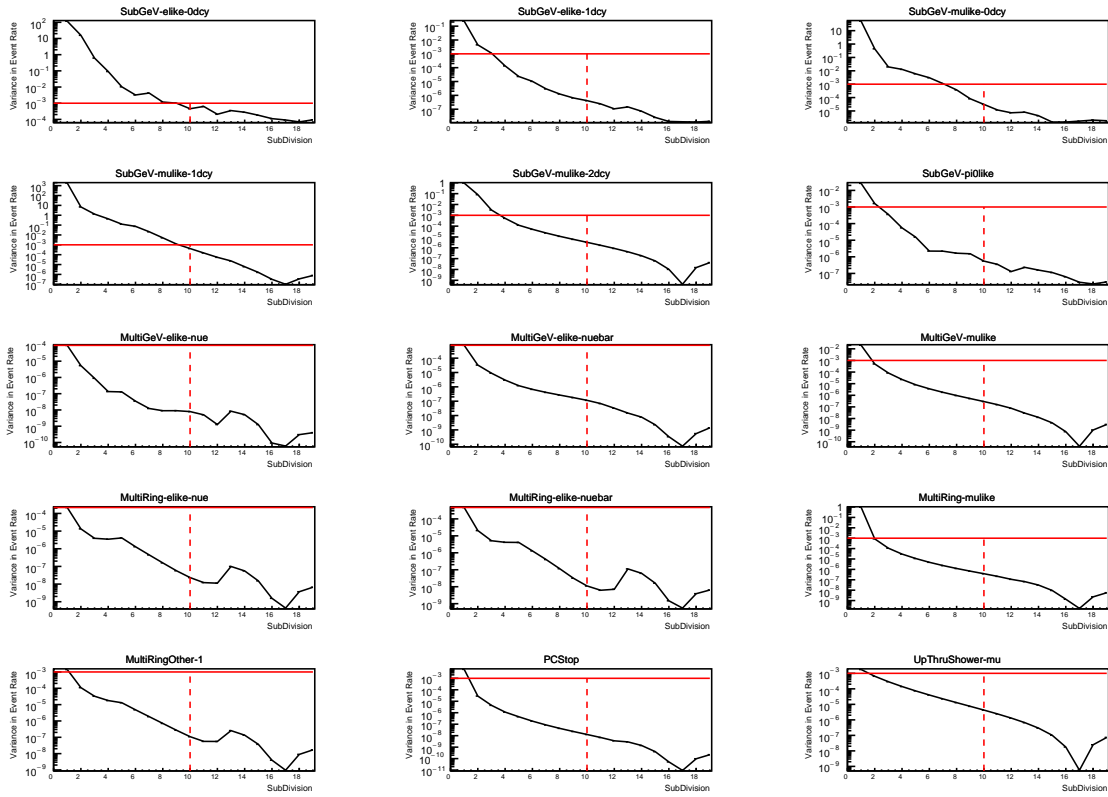


Figure 5.9: Variance of event rate for each atmospheric sample as a function of the number of sub-divisions per coarse bin. The solid red line indicates the 0.1% threshold and the dashed red line is a graphical indication of the variance at a sub-division $N = 10$.

1750 The second study to determine the value of N is as follows. The likelihood for
 1751 each sample is computed against an Asimov data set created with oscillation pa-
 1752 rameters from “Asimov A” in Table 5.1. Following Equation 5.4, the variance of the
 1753 log-likelihood over all considered N is computed. The results are shown in Figure 5.10.

1754 This tests the impact of the averaging on each sample's binning by reconstructed
 1755 momentum and/or zenith angle and also provides a scale for the calculation errors
 1756 compared to their statistical uncertainties.

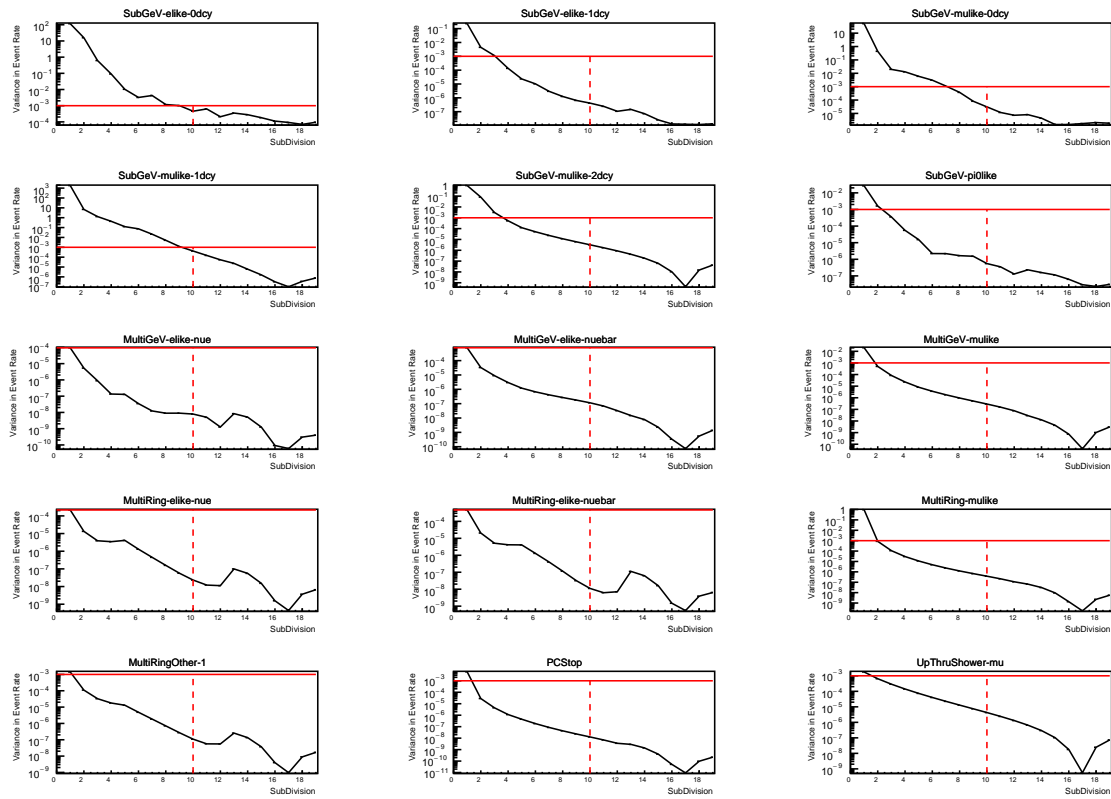


Figure 5.10: Variance of sample likelihood, when compared to 'Asimov data' set at Asimov A, for each atmospheric sample as a function of the number of sub-divisions per coarse bin. The solid red line indicates the 0.1% threshold and the dashed red line is a graphical indication of the variance at a sub-division $N = 10$.

1757 A choice of N sub-divisions per coarse bin has a variance in both event rate and
 1758 log-likelihood residuals less than the required threshold of 0.001. The event rate test is
 1759 the more stringent test. For the variance of log-likelihood residuals, the largest value is
 1760 of order 10^{-7} , corresponding to an error on the log-likelihood of about 3×10^{-4} , small
 1761 enough to be negligible for the oscillation analysis.

₁₇₆₂ In practice Figure 5.11 illustrates the effect of the smearing using $N = 10$. The fast
₁₇₆₃ oscillations in the sub-GeV upgoing region have been replaced with a normalisation
₁₇₆₄ effect whilst the large matter resonance structure remains.

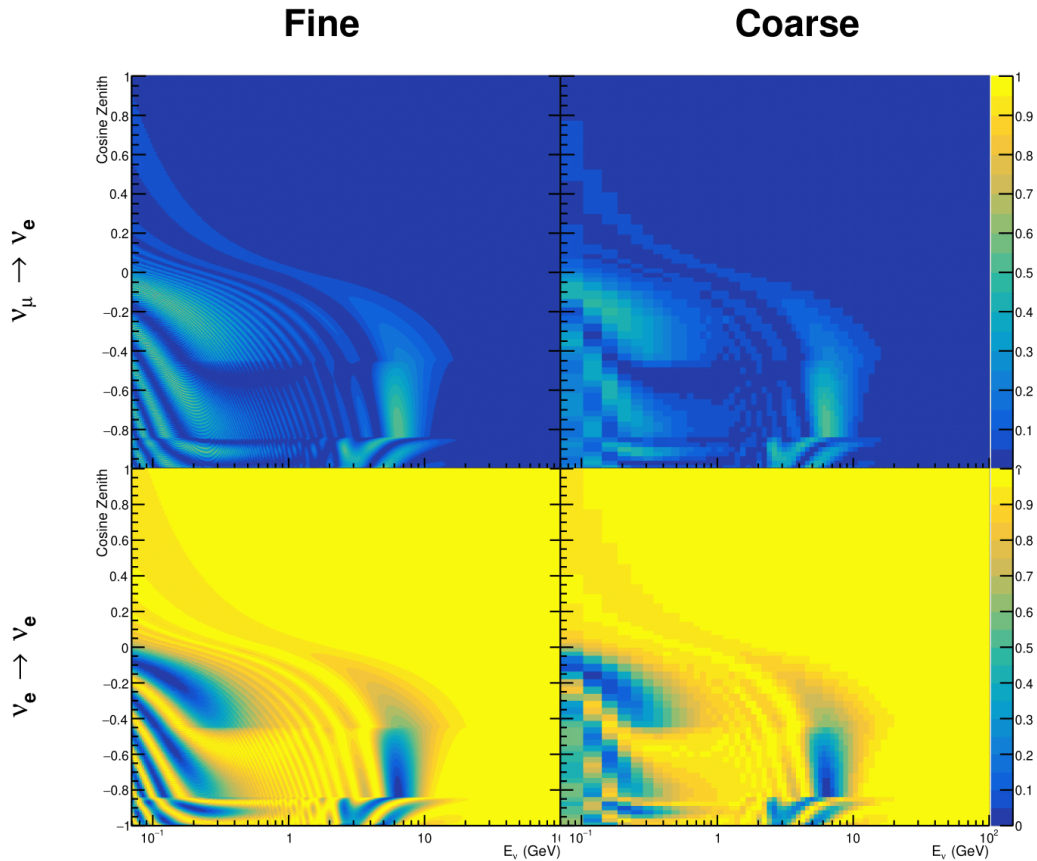


Figure 5.11: The oscillation probability, $P(\nu_\mu \rightarrow \nu_e)$ (top row) and $P(\nu_e \rightarrow \nu_e)$ (bottom row), given as a function of neutrino energy and zenith angle. The left column gives the “fine” binning used to calculate the oscillation probabilities and the right column illustrates the “coarse” binning used to reweight the MC events. The fine binning choice is given with $N = 10$, which was determined to be below threshold from Figure 5.9 and Figure 5.10.

1765 5.3 Calculation Engine

1766 As previously discussed in section 5.2, the calculation of oscillation probabilities is per-
1767 formed at run-time due to utilising continuous oscillation parameters. Consequently,
1768 the time per calculation is crucial for fit performance. The fitting framework used for
1769 this analysis was developed with ProbGPU [181]. This is a GPU-only implementation
1770 of the prob3 engine [182]. It is primarily designed for neutrino propagation in a beam
1771 experiment (single layer of constant density) with the atmospheric propagation code
1772 not being used prior to the analysis in this thesis.

1773 Another engine, CUDAProb3 [183], has been implemented within the fitting frame-
1774 work used within this analysis. It has been specifically optimised for atmospheric
1775 neutrino oscillation calculation so unfortunately does not contain the code to replace
1776 the beam oscillation calculation. Based on the benefits shown by the implementation
1777 in this chapter, efforts are being placed into including linear propagation for beam
1778 neutrino propagation into the engine [184]. The engine utilises object-orientated tech-
1779 niques as compared to the functional implementation of ProbGPU. This allows the
1780 energy and cosine zenith arrays to be kept on GPU memory, rather than having to
1781 load these arrays onto GPU memory for each calculation. General memory interfacing
1782 is one of the slowest tasks which GPUs can do, so being able to eliminate this signifi-
1783 cantly reduces the time required for calculation. This can be seen in Figure 5.12, where
1784 the GPU implementation of CUDAProb3 is approximately three times faster than the
1785 ProbGPU engine.

1786 Another significant advantage of CUDAProb3 is that it contains a CPU multithreaded
1787 implementation which is not possible with the ProbGPU or prob3 engines. This elimi-
1788 nates the requirement for GPU resources when submitting jobs to batch systems. As
1789 illustrated in Figure 5.12, the calculation speed depends on the number of available

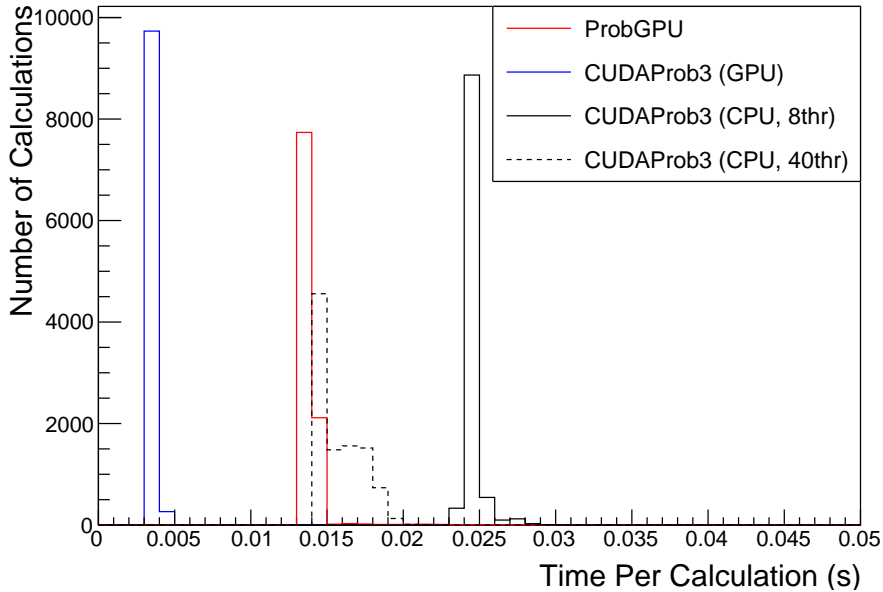


Figure 5.12: The calculation time taken to both calculate the oscillation probabilities and fill the “coarse” oscillograms, following the technique given in section 5.2, for the CUDAProb3 and ProbGPU (Red) calculation engines. CUDAProb3 has both a GPU (Blue) and CPU (Black) implementation, where the CPU implementation is multithreaded. Therefore, 8-threads (solid) and 40-threads (dashed) configurations have been used. Prob3, which is a CPU single-thread implementation has a mean step time of 1.142s.

1790 threads. Using 8 threads (which is typical of the batch systems being used) is ap-
 1791 proximately twice as slow as the ProbGPU engine implementation, but would allow
 1792 the fitting framework to be run on many more resources. This fact is utilised for any
 1793 SK-only fits but GPU resources are required for any fits which include beam samples
 1794 due to the ProbGPU requirement.

1795 5.4 Matter Density Profile

1796 For an experiment observing atmospheric neutrinos propagating through the Earth,
 1797 such as the studies presented in this thesis, a model of the Earth’s density and layering
 1798 is required. The model used within this analysis is the Preliminary Reference Earth
 1799 Model (PREM) [185]. This model provides piecewise cubic polynomials as a function

of radius which results in the density profile illustrated in Figure 5.13. As will be discussed in section 5.5, the propagator used within the calculation engine requires constant density layers. To follow the official SK-only analysis [180], the average density of each layer has been taken from the PREM model. Table 5.2 documents the density and radii of the layers used within this approximation.

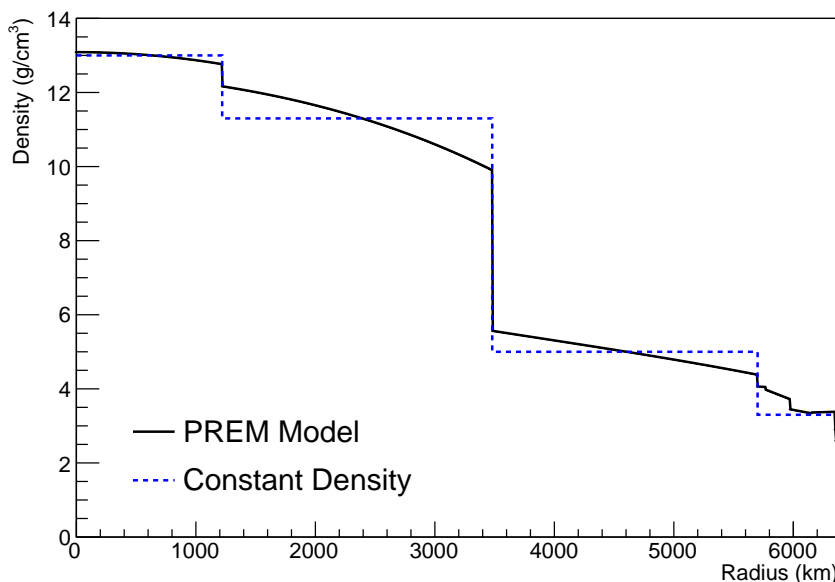


Figure 5.13: The density of the Earth given as a function of the radius, as given by the PREM model (Black) and the constant density four-layer approximation (Blue), as used in the official SK-only analysis.

Layer	Outer Radius [km]	Density [g/cm ³]	Chemical composition (Z/A)
Inner Core	1220	13	0.468 ± 0.029
Outer Core	3480	11.3	0.468 ± 0.029
Lower Mantle	5701	5.0	0.496
Transition Zone	6371	3.3	0.496

Table 5.2: Description of the four layers of the Earth invoked within the average constant density approximation of the PREM model [185].

The density measurements provided in the PREM model are provided in terms of mass density, whereas neutrino oscillations are sensitive to the electron number density. This value can be computed as the product of the chemical composition, or

1808 the Z/A value, and the mass density of each layer. Currently, the only way to calculate
 1809 this value for layers close to the Earth's core is through neutrino oscillations. The
 1810 chemical composition of the upper layers of the Earth's Mantle and the Transition
 1811 zone is well known due to it being predominantly pyrolite which has a chemical
 1812 composition value of 0.496 [186]. The components of the Earth's core region are less
 1813 well known. Consequently, the chemical composition dial for the core layers is set
 1814 to a value of 0.468 [187]. This value is assigned a Gaussian error with a standard
 1815 deviation equivalent to the difference in chemical composition in core and mantle
 1816 layers. Figure 5.14 illustrates the effect of moving from the $Z/A = 0.5$ method which
 1817 is used in the official SK-only analysis [180] to more precise values recorded by other
 1818 neutrino experiments.

1819 The beam oscillation probability in this thesis uses a baseline of 295km, density
 1820 2.6g/cm^3 [188], and chemical composition 0.5 as is done by the official T2K-only
 1821 analysis.

1822 Whilst the propagator requires a fixed density layer model of the Earth, the density
 1823 only has to be fixed for a specific neutrino energy $\times \cos(\theta_Z)$ bin in a given layer (I.e.
 1824 set of values at which to calculate the oscillation probability). As the density is a
 1825 function of radius, which is a function of the direction in which a neutrino propagates,
 1826 a better approximation of the PREM model can be made if a $\cos(\theta_Z)$ -specific density is
 1827 calculated.

1828 To achieve this, the average density, $\langle \rho \rangle_i$, in the i^{th} layer, is calculated as the density,
 1829 ρ , integrated over the track a given $\cos(\theta_Z)$,

$$\langle \rho \rangle_i = \frac{1}{t_{i+1} - t_i} \int_{t_i}^{t_{i+1}} \rho(t) dt \quad (5.5)$$

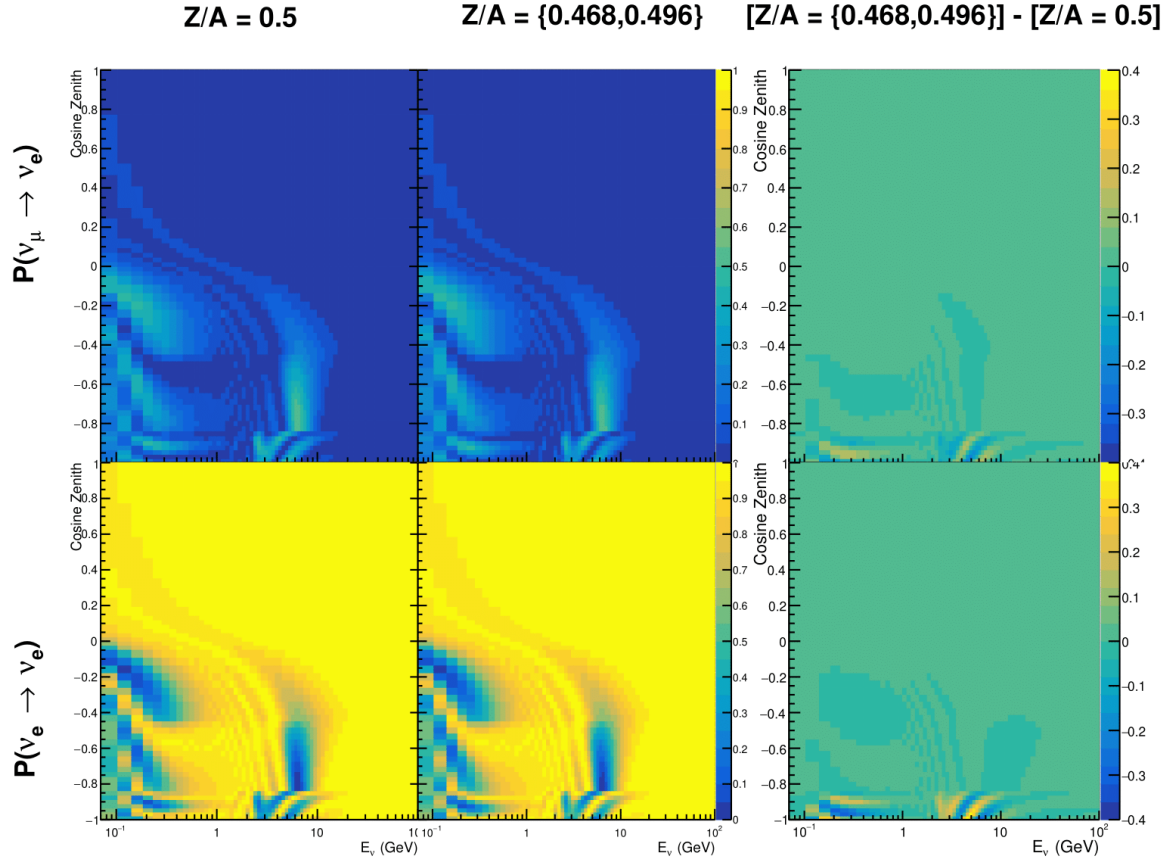


Figure 5.14: The oscillation probability, $P(\nu_\mu \rightarrow \nu_e)$ (top row) and $P(\nu_e \rightarrow \nu_\mu)$ (bottom row), given as a function of neutrino energy and zenith angle. The left column gives probabilities where the constant $Z/A = 0.5$ approximation which is used in the official SK-only analysis. The middle column gives the probabilities where the more accurate $Z/A = [0.468, 0.498]$ values as given in Table 5.2. The right column illustrates the difference in oscillation probability between the two different techniques.

1830 where t_i are the intersection points between each layer and t is the path length of
 1831 the trajectory across the layer which is dependent upon $\cos(\theta_Z)$.

1832 The oscillation probability calculation speed is approximately linear in the number
 1833 of layers invoked within the Earth model. Therefore a four-layer model is still utilized
 1834 with the only difference to the above example being that the four-layer model used for
 1835 each value of $\cos(\theta_Z)$ is different. Following the method outlined in [189], a four-layer
 1836 piecewise quadratic polynomial is fit to the PREM model for the four layers defined in

¹⁸³⁷ Table 5.2. This fit was not performed by the author of the thesis and is documented
¹⁸³⁸ in [190]. The coefficients of the quadratic fit to each layer are given in Table 5.3 with
¹⁸³⁹ the final distribution illustrated in Figure 5.15. The quadratic approximation is clearly
¹⁸⁴⁰ much closer to the PREM model as compared to the constant density approximation.

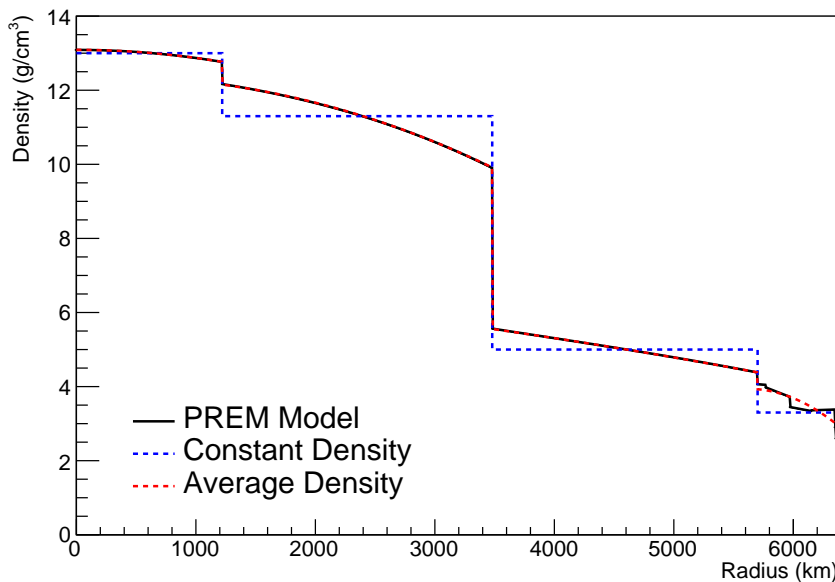


Figure 5.15: The density of the Earth given as a function of the radius, as given by the PREM model (Black), the constant density four-layer approximation (Blue), as used in the official SK-only analysis, and the quadratic approximation of the PREM model (Red).

Layer	Outer Radius [km]	Density [g/cm ³]
Inner Core	1220	$13.09 - 8.84x^2$
Outer Core	3480	$12.31 + 1.09x - 10.02x^2$
Lower Mantle	5701	$6.78 - 1.56x - 1.25x^2$
Transition Zone	6371	$-50.42 + 123.33x - 69.95x^2$

Table 5.3: The quadratic polynomial fits to the PREM model for four assumed layers of the PREM model. The fit to calculate the coefficients is given in [190], where $x = R/R_{Earth}$.

¹⁸⁴¹ The effect of using the average density per $\cos(\theta_Z)$ model is highlighted in Fig-
¹⁸⁴² ure 5.16. The slight discontinuity in the oscillation probability around $\cos(\theta_Z) \sim -0.45$
¹⁸⁴³ in the fixed density model, which is due to the transition to mantle layer boundary, has

₁₈₄₄ been reduced. This is expected as the difference in the density across this boundary is
₁₈₄₅ significantly smaller in the average density model as compared to the constant density
₁₈₄₆ model. Whilst the difference in density across the other layer transitions is reduced,
₁₈₄₇ there is still a significant difference. This means the discontinuities in the oscillation
₁₈₄₈ probabilities remain but are significantly reduced. However, as the average density
₁₈₄₉ approximation matches the PREM model well in this region, these discontinuities are
₁₈₅₀ due to the Earth model rather than an artifact of the oscillation calculation.

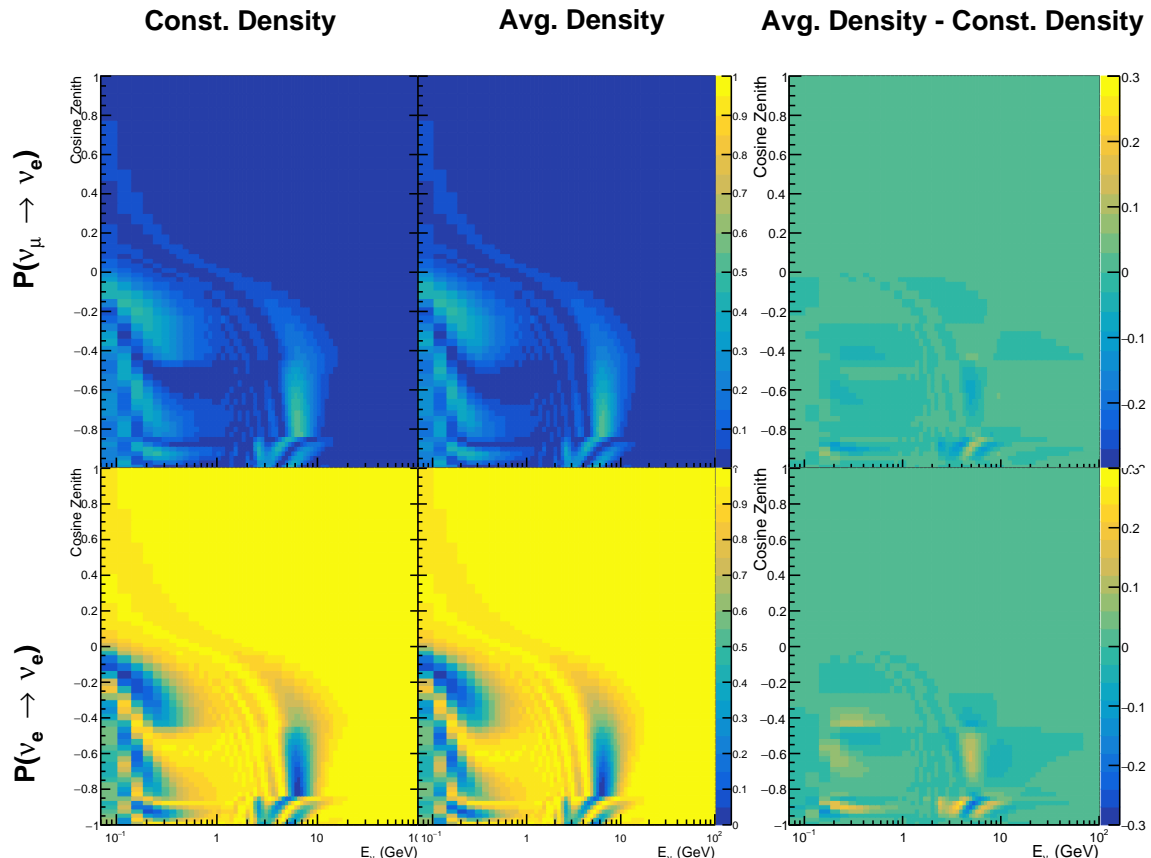


Figure 5.16: The oscillation probability, $P(\nu_\mu \rightarrow \nu_e)$ (top row) and $P(\nu_e \rightarrow \nu_\mu)$ (bottom row), given as a function of neutrino energy and zenith angle. The left column gives probabilities where the four-layer constant density approximation is used. The middle column gives the probabilities where the density is integrated over the trajectory, using the quadratic PREM approximation, for each $\cos(\theta_Z)$ is used. The right column illustrates the difference in oscillation probability between the two different techniques.

1851 5.5 Production Height Averaging

1852 As discussed in section 5.1, the height at which the cosmic ray flux interacts in the
1853 atmosphere is not known on an event-by-event basis. The production height can
1854 vary from the Earth's surface to 50km above that. The SK-only analysis methodol-
1855 ogy (described in section 5.2) for including the uncertainty on the production height
1856 is to include variations from the Honda model when pre-calculating the oscillation
1857 probabilities prior to the fit. This technique is not possible for this analysis which
1858 uses continuous oscillation parameters that can not be known prior to the fit. Conse-
1859 quently, an analytical averaging technique was developed in [190]. The author of this
1860 thesis was not responsible for the derivation of the technique but has performed the
1861 implementation and validation of the technique for this analysis alone.

1862 The oscillation probability used within this analysis is based on [191]. The neutrino
1863 wavefunction in the vacuum Hamiltonian evolves in each layer of constant matter
1864 density via

$$i \frac{d\psi_j(t)}{dt} = \frac{m_j^2}{2E_\nu} \psi_j(t) - \sum_k \sqrt{2} G_F N_e U_{ej} U_{ke}^\dagger \psi_k(t), \quad (5.6)$$

1865 where m_j^2 is the square of the j^{th} vacuum eigenstate mass, E_ν is the neutrino energy,
1866 G_F is Fermi's constant, N_e is the electron number density and U is the PMNS matrix.
1867 $N_e \rightarrow -N_e$ and $\delta_{CP} \rightarrow -\delta_{CP}$ for antineutrino propagation.

1868 Using the 20 production heights per MC neutrino event, provided as 5% percentiles
1869 from the Honda flux model, a production height distribution $p_j(h|E_\nu, \cos \theta_Z)$ is built
1870 for each neutrino flavour $j = \nu_e, \bar{\nu}_e, \nu_\mu, \bar{\nu}_\mu$. In practice, a histogram is filled with 20
1871 evenly spaced bins in production height h between 0 and 50km. The neutrino energy

¹⁸⁷² and cosine zenith binning is the same as that provided in section 5.2. The average
¹⁸⁷³ production height, $\bar{h} = \int dh \frac{1}{4} \sum_j p_j(h|E_\nu, \cos(\theta_Z))$, is calculated. The production height
¹⁸⁷⁴ binning of this histogram is then translated into $\delta t(h) = t(z, \bar{h}) - t(z, h)$, where $t(z, h)$
¹⁸⁷⁵ is the distance travelled along the trajectory.

¹⁸⁷⁶ For the i^{th} traversed layer, the transition amplitude, $D_i(t_{i+1}, t_i)$, is computed. The
¹⁸⁷⁷ time ordered product of these is then used as the overall transition amplitude via

$$A(t_{n+1}, t_0) = D_n(t_{n+1}, t_n) \dots D_1(t_2, t_1) D_0(t_1, t_0), \quad (5.7)$$

¹⁸⁷⁸ where,

$$\begin{aligned} D_n(t_{n+1}, t_n) &= \exp[-iH_n(t_{n+1} - t_n)] \\ &= \sum_{k=1}^3 C_k \exp[ia_k \delta t] \end{aligned} \quad (5.8)$$

¹⁸⁷⁹ is expressed as a diagonalised time-dependent solution to the schrodinger equation.
¹⁸⁸⁰ The 0^{th} layer is the propagation through the atmosphere and is the only term which
¹⁸⁸¹ depends on the production height. Using the subsitution $t_0 = t(\bar{h}) - \delta t(h)$, it can be
¹⁸⁸² shown that

$$D_0(t_1, t_0) = D_0(t_1, \bar{h}) D_0(\delta t). \quad (5.9)$$

¹⁸⁸³ Thus Equation 5.7 becomes

$$\begin{aligned}
A(t_{n+1}, t_0) &= D_n(t_{n+1}, t_n) \dots D_1(t_2, t_1) D_0(t_1, \bar{h}) D(\delta t) \\
&= A(t_{n+1}, \bar{h}) \sum_{k=1}^3 C_k \exp[i a_k \delta t], \\
&= \sum_{k=1}^3 B_k \exp[i a_k \delta t].
\end{aligned} \tag{5.10}$$

1884 The oscillation probability averaged over production height is calculated as

$$\begin{aligned}
\bar{P}(\nu_j \rightarrow \nu_i) &= \int d(\delta t) p_j(\delta t | E_\nu, \cos \theta_Z) P(\nu_j \rightarrow \nu_i) \\
&= \int d(\delta t) p_j(\delta t | E_\nu, \cos \theta_Z) A(t_{n+1}, t_0) A^*(t_{n+1}, t_0) \\
&= \sum_{km} (B_k)_{ij} (B_m)_{ij}^* \int d(\delta t) p_j(\delta t | E_\nu, \cos \theta_Z) \exp[i(a_k - a_m)\delta t]
\end{aligned} \tag{5.11}$$

1885 In practice, implementation in CUDAProb3 [183] is relatively straightforward as
1886 the majority of these terms are already calculated in the standard oscillation calculation.
1887 Figure 5.17 illustrates the results of the production height averaging. As expected,
1888 the main effect is observed in the low-energy downward-going and horizontal-going
1889 events. Upward-going events have to travel the radius of the Earth, $R_E = 6371\text{km}$,
1890 where the production height uncertainty is a small fraction of the total path length.

1891

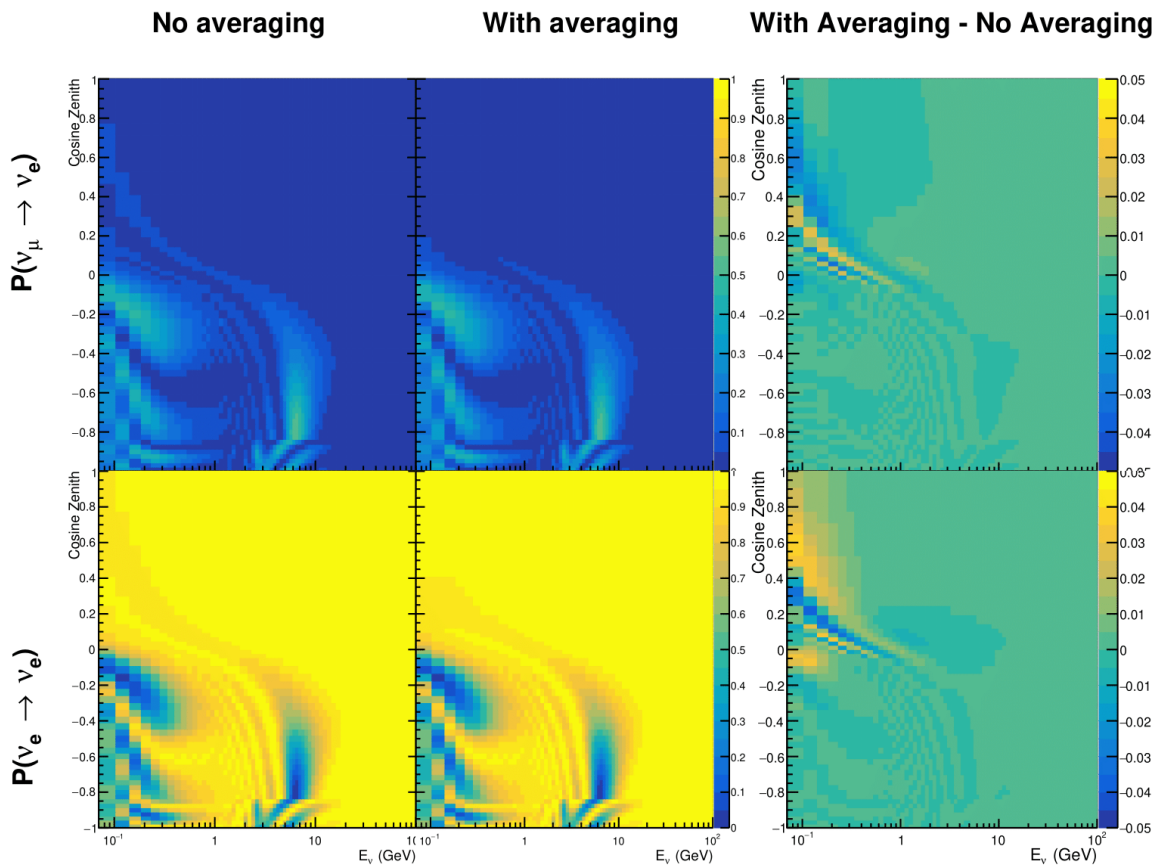


Figure 5.17: The oscillation probability, $P(\nu_\mu \rightarrow \nu_e)$ (top row) and $P(\nu_e \rightarrow \nu_e)$ (bottom row), given as a function of neutrino energy and zenith angle. The left column gives probabilities where a fixed production height of 25km is used. The middle column gives the probabilities where the production height is analytically averaged. The right column illustrates the difference in oscillation probability between the two different techniques.

₁₈₉₂ **Bibliography**

- ₁₈₉₃ [1] J. Chadwick, Verhandl. Dtsc. Phys. Ges. **16**, 383 (1914).
- ₁₈₉₄ [2] C. D. Ellis and W. A. Wooster, Proc. R. Soc. Lond. A Math. Phys. Sci. **117**, 109 (1927).
- ₁₈₉₅
- ₁₈₉₆ [3] W. Pauli, Phys. Today **31N9**, 27 (1978).
- ₁₈₉₇ [4] E. Fermi, Z. Phys. **88**, 161 (1934).
- ₁₈₉₈ [5] F. Reines and C. L. Cowan, Phys. Rev. **92**, 830 (1953).
- ₁₈₉₉ [6] C. L. Cowan, F. Reines, F. B. Harrison, H. W. Kruse, and A. D. McGuire, Science **124**, 103 (1956), <http://science.sciencemag.org/content/124/3212/103.full.pdf>.
- ₁₉₀₀
- ₁₉₀₁ [7] G. Danby *et al.*, Phys. Rev. Lett. **9**, 36 (1962).
- ₁₉₀₂ [8] K. Kodama *et al.*, Physics Letters B **504**, 218 (2001).
- ₁₉₀₃ [9] LSND, A. Aguilar-Arevalo *et al.*, Phys. Rev. **D64**, 112007 (2001), hep-ex/0104049.
- ₁₉₀₄ [10] MiniBooNE Collaboration, A. A. Aguilar-Arevalo *et al.*, Phys. Rev. Lett. **110**, 161801 (2013).
- ₁₉₀₅
- ₁₉₀₆ [11] and P. A. R. Ade *et al.*, Astronomy and Astrophysics **594**, A13 (2016).
- ₁₉₀₇ [12] B. Pontecorvo, Sov. Phys. JETP **26**, 984 (1968), [Zh. Eksp. Teor. Fiz. 53, 1717 (1967)].
- ₁₉₀₈ [13] B. Pontecorvo, Sov. Phys. JETP **7**, 172 (1958), [Zh. Eksp. Teor. Fiz. 34, 247 (1957)].
- ₁₉₀₉ [14] M. Kobayashi and T. Maskawa, Progress of Theoretical Physics **49**, 652 (1973).
- ₁₉₁₀ [15] N. Cabibbo, Phys. Rev. Lett. **10**, 531 (1963).
- ₁₉₁₁ [16] A. Y. Smirnov, (2003).
- ₁₉₁₂ [17] S. Mikheyev and A. Smirnov, Soviet Journal of Nuclear Physics **42**, 913 (1985).
- ₁₉₁₃ [18] L. Wolfenstein, Phys. Rev. D **17**, 2369 (1978).
- ₁₉₁₄ [19] The Super-Kamiokande Collaboration, Y. Ashie *et al.*, Phys. Rev. Lett. **93**, 101801 (2004).
- ₁₉₁₅
- ₁₉₁₆ [20] SNO Collaboration, Q. R. Ahmad *et al.*, Phys. Rev. Lett. **89**, 011301 (2002).

- [21] 2015 Nobel prize in Physics as listed by Nobelprize.org, https://www.nobelprize.org/nobel_prizes/physics/laureates/2015/, Accessed: 22-06-2022.
- [22] J. A. Formaggio and G. P. Zeller, Rev. Mod. Phys. **84**, 1307 (2012), 1305.7513.
- [23] A. Bellerive, Int. J. Mod. Phys. A **19**, 1167 (2004).
- [24] R. Davis, D. S. Harmer, and K. C. Hoffman, Phys. Rev. Lett. **20**, 1205 (1968).
- [25] N. Vinyoles *et al.*, Astrophys. J. **835**, 202 (2017).
- [26] V. Gribov and B. Pontecorvo, Phys. Lett. B **28**, 493 (1969).
- [27] K. S. Hirata *et al.*, Phys. Rev. Lett. **63**, 16 (1989).
- [28] W. Hampel *et al.*, Phys. Lett. B **447**, 127 (1999).
- [29] SAGE Collaboration, J. N. Abdurashitov *et al.*, Phys. Rev. C **60**, 055801 (1999).
- [30] Q. R. Ahmad *et al.*, Phys. Rev. Lett. **89** (2002).
- [31] Borexino Collaboration, Nature **562**, 505 (2018).
- [32] B. Aharmim *et al.*, Astrophys. J. **653**, 1545 (2006).
- [33] M. Agostini *et al.*, (2020).
- [34] S. Andringa *et al.*, Adv. High Energy Phys. **2016**, 1 (2016).
- [35] J. F. Beacom *et al.*, Chin. phys. C **41**, 023002 (2017).
- [36] F. An *et al.*, J. Phys. G Nucl. Part. Phys. **43**, 030401 (2016).
- [37] J. Aalbers *et al.*, (2020), 2006.03114.
- [38] T. K. Gaisser and M. Honda, (2002).
- [39] G. D. Barr, T. K. Gaisser, P. Lipari, S. Robbins, and T. Stanev, Physical Review D **70** (2004).
- [40] M. Honda, T. Kajita, K. Kasahara, S. Midorikawa, and T. Sanuki, Physical Review D **75** (2007).
- [41] M. Honda, T. Kajita, K. Kasahara, and S. Midorikawa, Phys. Rev. D **70**, 043008 (2004).

- 1943 [42] M. Honda, T. Kajita, K. Kasahara, and S. Midorikawa, Phys. Rev. D **83**, 123001
1944 (2011).
- 1945 [43] A. Fasso, A. Ferrari, P. R. Sala, and J. Ranft, (2001).
- 1946 [44] Y. Ashie *et al.*, Physical Review D **71** (2005).
- 1947 [45] F. Reines *et al.*, Phys. Rev. Lett. **15**, 429 (1965).
- 1948 [46] D. Casper *et al.*, Phys. Rev. Lett. **66**, 2561 (1991).
- 1949 [47] K. S. Hirata *et al.*, Phys. Lett. B **280**, 146 (1992).
- 1950 [48] Z. Li *et al.*, Physical Review D **98** (2018).
- 1951 [49] Kamiokande Collaboration *et al.*, (2017).
- 1952 [50] T2K Collaboration, Nature **580**, 339 (2020).
- 1953 [51] M. A. Acero *et al.*, Phys. Rev. Lett. **123**, 151803 (2019).
- 1954 [52] M. G. Aartsen *et al.*, Phys. Rev. Lett. **120** (2018).
- 1955 [53] P. Adamson *et al.*, Phys. Rev. Lett. **112** (2014).
- 1956 [54] M. S. Athar *et al.*, Progress in Particle and Nuclear Physics **124**, 103947 (2022).
- 1957 [55] G. Danby *et al.*, Phys. Rev. Lett. **9**, 36 (1962).
- 1958 [56] K. Abe *et al.*, Physical Review D **87** (2013).
- 1959 [57] MINOS Collaboration, D. G. Michael *et al.*, Phys. Rev. Lett. **97**, 191801 (2006).
- 1960 [58] G. Danby *et al.*, Phys. Rev. Lett. **9**, 36 (1962).
- 1961 [59] NOvA Collaboration, M. A. Acero *et al.*, Phys. Rev. Lett. **123**, 151803 (2019).
- 1962 [60] B. Abi, R. Acciarri, M. A. Acero, and G. e. a. Adamov, Eur. Phys. J. C Part. Fields
1963 **80** (2020).
- 1964 [61] Hyper-Kamiokande Proto-Collaboration *et al.*, Prog. Theor. Exp. Phys. **2015**,
1965 53C02 (2015).
- 1966 [62] C. Blanco, D. Hooper, and P. Machado, Physical Review D **101** (2020).
- 1967 [63] MicroBooNE Collaboration *et al.*, Search for an Excess of Electron Neutrino
1968 Interactions in MicroBooNE Using Multiple Final State Topologies, 2021.

- 1969 [64] KARMEN Collaboration, B. Armbruster *et al.*, Phys. Rev. D **65**, 112001 (2002).
- 1970 [65] S.-B. Kim, T. Lasserre, and Y. Wang, Adv. High Energy Phys. **2013**, 1 (2013).
- 1971 [66] M. Sajjad Athar *et al.*, Prog. Part. Nucl. Phys. **124**, 103947 (2022), 2111.07586.
- 1972 [67] K. Abe *et al.*, Nucl. Instrum. Methods Phys. Res. A **1027**, 166248 (2022).
- 1973 [68] F. P. An *et al.*, Phys. Rev. Lett. **108**, 171803 (2012).
- 1974 [69] RENO Collaboration, J. K. Ahn *et al.*, Phys. Rev. Lett. **108**, 191802 (2012).
- 1975 [70] Double Chooz Collaboration, Y. Abe *et al.*, Phys. Rev. Lett. **108**, 131801 (2012).
- 1976 [71] J. Collaboration *et al.*, TAO Conceptual Design Report: A Precision Measurement
1977 of the Reactor Antineutrino Spectrum with Sub-percent Energy Resolution, 2020,
1978 2005.08745.
- 1979 [72] for the RENO Collaboration, New results from RENO and the 5 MeV excess,
1980 AIP Publishing LLC, 2015.
- 1981 [73] Y. Abe *et al.*, Journal of High Energy Physics **2014** (2014).
- 1982 [74] Daya Bay Collaboration, D. Adey *et al.*, Phys. Rev. Lett. **123**, 111801 (2019).
- 1983 [75] M. P. Decowski, Nucl. Phys. B. **908**, 52 (2016).
- 1984 [76] The KamLAND Collaboration, A. Gando *et al.*, Phys. Rev. D **83**, 052002 (2011).
- 1985 [77] Y. Fukuda *et al.*, Phys. Rev. Lett. **81**, 1562 (1998).
- 1986 [78] K. Abe *et al.*, Nuclear Instruments and Methods in Physics Research Section
1987 A: Accelerators, Spectrometers, Detectors and Associated Equipment **737**, 253
1988 (2014).
- 1989 [79] S. Fukuda *et al.*, Nucl. Instrum. Methods Phys. Res. A **501**, 418 (2003).
- 1990 [80] Y. Itow *et al.*, (2001).
- 1991 [81] M. Jiang *et al.*, Prog. Theor. Exp. Phys. **2019** (2019).
- 1992 [82] S. Fukuda *et al.*, Nuclear Instruments and Methods in Physics Research Section
1993 A: Accelerators, Spectrometers, Detectors and Associated Equipment **501**, 418
1994 (2003), <http://www.sciencedirect.com/science/article/pii/S016890020300425X>.
- 1995 [83] Y. Nakano *et al.*, Nucl. Instrum. Methods Phys. Res. A **977**, 164297 (2020).

- 1996 [84] Hamamatsu, Hamamatsu Photonics Photomultiplier Tubes Handbook.
- 1997 [85] K. Abe *et al.*, Nucl. Instrum. Methods Phys. Res. A **1027**, 166248 (2022).
- 1998 [86] J. F. Beacom and M. R. Vagins, Phys. Rev. Lett. **93**, 171101 (2004).
- 1999 [87] L. Marti *et al.*, Nucl. Instrum. Methods Phys. Res. A **959**, 163549 (2020).
- 2000 [88] L. Marti *et al.*, (2019).
- 2001 [89] G. Carminati, Phys. Procedia **61**, 666 (2015).
- 2002 [90] T. Tanimori *et al.*, IEEE Transactions on Nuclear Science **36**, 497 (1989).
- 2003 [91] Super-Kamiokande Collaboration, J. Hosaka *et al.*, Phys. Rev. D **73**, 112001 (2006).
- 2005 [92] H. Nishino *et al.*, Nucl. Instrum. Methods Phys. Res. A **610**, 710 (2009).
- 2006 [93] S. Yamada *et al.*, IEEE Transactions on Nuclear Science **57**, 428 (2010).
- 2007 [94] S. Yamada, Y. Hayato, Y. Obayashi, and M. Shiozawa, New online system
2008 without hardware trigger for the Super-Kamiokande experiment, in *2007 IEEE*
2009 *Nuclear Science Symposium Conference Record*, IEEE, 2007.
- 2010 [95] P. A. Čerenkov, Phys. Rev. **52**, 378 (1937).
- 2011 [96] I. Frank and I. Tamm, Coherent visible radiation of fast electrons passing
2012 through matter, in *Selected Papers*, pp. 29–35, Springer Berlin Heidelberg, Berlin,
2013 Heidelberg, 1991.
- 2014 [97] The T2K Collaboration, KEK Proposal (2001),
2015 <http://neutrino.kek.jp/jhfnu/loi/loi.v2.030528.pdf>.
- 2016 [98] Y. Itow *et al.*, (2001), hep-ex/0106019.
- 2017 [99] The K2K Collaboration and S. H. Ahn, (2001), hep-ex/0103001.
- 2018 [100] The T2K Collaboration, KEK Proposal (2006), http://j-parc.jp/researcher/Hadron/en/pac_0606/pdf/p11-Nishikawa.pdf.
- 2020 [101] T2K Collaboration, K. Abe *et al.*, Phys. Rev. Lett. **112**, 061802 (2014),
2021 <https://link.aps.org/doi/10.1103/PhysRevLett.112.061802>.
- 2022 [102] NINJA Collaboration, T. Fukuda *et al.*, Proposal for precise measurement of

- 2023 neutrino-water cross-section in NINJA physics run, Proposal for J-PARC and
2024 KEK, 2017.
- 2025 [103] T. Ovsianikova *et al.*, Physics of Particles and Nuclei **48**, 1014 (2017),
2026 <https://doi.org/10.1134/S1063779617060478>.
- 2027 [104] M. Antonova *et al.*, Journal of Instrumentation **12**, C07028 (2017),
2028 <http://stacks.iop.org/1748-0221/12/i=07/a=C07028>.
- 2029 [105] The T2K Collaboration, K. Abe *et al.*, Phys. Rev. D **102**, 012007 (2020).
- 2030 [106] K. Abe *et al.*, Progress of Theoretical and Experimental Physics **2021** (2021).
- 2031 [107] The T2K Collaboration, K. Abe *et al.*, Nuclear Instruments
2032 and Methods in Physics Research Section A: Accelerators, Spec-
2033 trometers, Detectors and Associated Equipment **659**, 106 (2011),
2034 <http://www.sciencedirect.com/science/article/pii/S0168900211011910>.
- 2035 [108] K. Matsuoka *et al.*, Nuclear Instruments and Methods in Physics Research Section
2036 A: Accelerators, Spectrometers, Detectors and Associated Equipment **624**, 591
2037 (2010), <http://www.sciencedirect.com/science/article/pii/S016890021002098X>.
- 2038 [109] K. Abe *et al.*, Phys. Rev. D. **103** (2021).
- 2039 [110] T. Vladislavljevic, *Predicting the T2K neutrino flux and measuring oscillation parame-*
2040 tersSpringer theses, 1 ed. (Springer Nature, Cham, Switzerland, 2020).
- 2041 [111] D. Beavis, A. Carroll, and I. Chiang, (1995).
- 2042 [112] P.-A. Amaudruz *et al.*, Nuclear Instruments and Methods in Physics Research
2043 Section A: Accelerators, Spectrometers, Detectors and Associated Equipment
2044 **696**, 1 (2012).
- 2045 [113] N. Abgrall *et al.*, Nuclear Instruments and Methods in Physics Research Section
2046 A: Accelerators, Spectrometers, Detectors and Associated Equipment **637**, 25
2047 (2011).
- 2048 [114] S. Assylbekov *et al.*, Nuclear Instruments and Methods in Physics Research
2049 Section A: Accelerators, Spectrometers, Detectors and Associated Equipment
2050 **686**, 48 (2012).
- 2051 [115] D. Allan *et al.*, Journal of Instrumentation **8**, P10019 (2013).

- 2052 [116] F. Vannucci, Advances in High Energy Physics **2014**, 1 (2014).
- 2053 [117] UA1 magnet sets off for a second new life, 2022.
- 2054 [118] S. Aoki *et al.*, Nuclear Instruments and Methods in Physics Research Section
2055 A: Accelerators, Spectrometers, Detectors and Associated Equipment **698**, 135
2056 (2013).
- 2057 [119] M. Yokoyama *et al.*, Nuclear Instruments and Methods in Physics Research
2058 Section A: Accelerators, Spectrometers, Detectors and Associated Equipment
2059 **622**, 567 (2010).
- 2060 [120] K. Suzuki *et al.*, Progress of Theoretical and Experimental Physics **2015**, 53C01
2061 (2015).
- 2062 [121] S. Brooks, A. Gelman, G. L. Jones, and X.-L. Meng, *Handbook of Markov Chain
Monte Carlo* (CRC Press, 2011).
- 2064 [122] W. R. Gilks, S. Richardson, and D. J. Spiegelhalter, *Markov Chain Monte Carlo in
Practice* (Chapman & Hall/CRC Interdisciplinary Statistics, 1995).
- 2066 [123] C. Wret, *Minimising systematic uncertainties in the T2K experiment using near-
detector and external data*, PhD thesis, Imperial College London, 2018.
- 2068 [124] K. E. Duffy, *Measurement of the Neutrino Oscillation Parameters $\sin^2 \theta_{23}$, Δm_{32}^2 ,
2069 $\sin^2 \theta_{13}$, and δ_{CP} in Neutrino and Antineutrino Oscillation at T2K*, PhD thesis, Oriel
2070 College, University of Oxford, 2016.
- 2071 [125] T. Bayes, Rev. Phil. Trans. Roy. Soc. Lond. **53**, 370 (1764).
- 2072 [126] N. Metropolis, A. W. Rosenbluth, M. N. Rosenbluth, A. H. Teller, and E. Teller,
2073 Journal of Chemical Physics **21** (1970).
- 2074 [127] W. K. Hastings, Biometrika **57** (1970).
- 2075 [128] J. Dunkley, M. Bucher, P. G. Ferreira, K. Moodley, and C. Skordis, Mon. Not. R.
2076 Astron. Soc. **356**, 925 (2005).
- 2077 [129] Particle Data Group *et al.*, Prog. Theor. Exp. Phys. **2020** (2020).
- 2078 [130] H. Jeffreys, *The Theory of Probability* Oxford Classic Texts in the Physical Sciences
2079 (, 1939).
- 2080 [131] R. E. Kass and A. E. Raftery, J. Am. Stat. Assoc. **90**, 773 (1995).

- 2081 [132] T. Böhlen *et al.*, Nuclear Data Sheets **120**, 211 (2014),
2082 <http://www.sciencedirect.com/science/article/pii/S0090375214005018>.
- 2083 [133] R. Brun *et al.*, *GEANT: Detector Description and Simulation Tool; Oct 1994*CERN
2084 Program Library (CERN, Geneva, 1993), <http://cds.cern.ch/record/1082634>,
2085 Long Writeup W5013.
- 2086 [134] T2K Collaboration, K. Abe *et al.*, Phys. Rev. D **87**, 012001 (2013).
- 2087 [135] C. Zeitnitz and T. Gabriel, Nuclear Instruments and Meth-
2088 ods in Physics Research Section A: Accelerators, Spectrom-
2089 eters, Detectors and Associated Equipment **349**, 106 (1994),
2090 <http://www.sciencedirect.com/science/article/pii/0168900294906130>.
- 2091 [136] N. Abgrall *et al.*, Physical Review C **84** (2011).
- 2092 [137] N. Abgrall *et al.*, Physical Review C **85** (2012).
- 2093 [138] N. Abgrall *et al.*, Nuclear Instruments and Methods in Physics Research Section
2094 A: Accelerators, Spectrometers, Detectors and Associated Equipment **701**, 99
2095 (2013), <http://www.sciencedirect.com/science/article/pii/S016890021201234X>.
- 2096 [139] HARP Collaboration, M. Apollonio *et al.*, Phys. Rev. C **80**, 035208 (2009),
2097 <https://link.aps.org/doi/10.1103/PhysRevC.80.035208>.
- 2098 [140] A. Fiorentini *et al.*, T2K Technical Note **217** (2017).
- 2099 [141] B. Blau *et al.*, Nuclear Physics B - Proceedings Supplements **113**, 125 (2002).
- 2100 [142] S. Haino *et al.*, Physics Letters B **594**, 35 (2004).
- 2101 [143] NASA, U.S. Standard Atmosphere, 1976, 1976.
- 2102 [144] S. Roesler, R. Engel, and J. Ranft, The Monte Carlo Event Generator DPMJET-III,
2103 in *Advanced Monte Carlo for Radiation Physics, Particle Transport Simulation and*
2104 *Applications*, pp. 1033–1038, Springer Berlin Heidelberg, 2001.
- 2105 [145] K. Niita *et al.*, Radiation Measurements **41**, 1080 (2006).
- 2106 [146] T. Sanuki *et al.*, Physics Letters B **541**, 234 (2002).
- 2107 [147] P. Achard *et al.*, Physics Letters B **598**, 15 (2004).
- 2108 [148] Y. Hayato and L. Pickering, The European Physical Journal Special Topics **230**,

- ²¹⁰⁹ 4469 (2021).
- ²¹¹⁰ [149] Y. Hayato, *Acta Physica Polonica B* **40** (2009).
- ²¹¹¹ [150] C. L. Smith, *Physics Reports* **3**, 261 (1972),
²¹¹² <http://www.sciencedirect.com/science/article/pii/0370157372900105>.
- ²¹¹³ [151] O. Benhar, A. Fabrocini, and S. Fantoni, *Nuclear Physics A* **497**, 423 (1989).
- ²¹¹⁴ [152] R. Bradford, A. Bodek, H. Budd, and J. Arrington, *Nu-*
²¹¹⁵ *clear Physics B - Proceedings Supplements* **159**, 127 (2006),
²¹¹⁶ <http://www.sciencedirect.com/science/article/pii/S0920563206005184>,
²¹¹⁷ *Proceedings of the 4th International Workshop on Neutrino-Nucleus Interac-*
²¹¹⁸ *tions in the Few-GeV Region.*
- ²¹¹⁹ [153] A. A. Aguilar-Arevalo *et al.*, *Physical Review D* **81** (2010).
- ²¹²⁰ [154] R. Gran, J. Nieves, F. Sanchez, and M. J. V. Vacas, *Phys. Rev. D* **88**, 113007 (2013),
²¹²¹ <https://link.aps.org/doi/10.1103/PhysRevD.88.113007>.
- ²¹²² [155] C. Berger and L. M. Sehgal, *Phys. Rev. D* **76**, 113004 (2007).
- ²¹²³ [156] C. Berger and L. M. Sehgal, *Phys. Rev. D* **79**, 053003 (2009),
²¹²⁴ <https://link.aps.org/doi/10.1103/PhysRevD.79.053003>.
- ²¹²⁵ [157] T. Sjöstrand, *Computer Physics Communications* **82**, 74 (1994).
- ²¹²⁶ [158] C. Bronner and M. Hartz, Tuning of the Charged Hadrons Multiplicities for Deep
²¹²⁷ Inelastic Interactions in NEUT, in *Proceedings of the 10th International Workshop on*
²¹²⁸ *Neutrino-Nucleus Interactions in Few-GeV Region (NuInt15)*, Journal of the Physical
²¹²⁹ Society of Japan, 2016.
- ²¹³⁰ [159] M. Glück, E. Reya, and A. Vogt, *The European Physical Journal C* **5**, 461 (1998).
- ²¹³¹ [160] A. Bodek and U.-k. Yang, Axial and Vector Structure Functions for Electron- and
²¹³² Neutrino- Nucleon Scattering Cross Sections at all Q^2 using Effective Leading
²¹³³ order Parton Distribution Functions, 2010.
- ²¹³⁴ [161] A. Bodek and U.-K. Yang, (2010).
- ²¹³⁵ [162] S. Gollapinni, (2016).
- ²¹³⁶ [163] E. S. P. Guerra *et al.*, *Phys. Rev. D* **99**, 052007 (2019).

- ²¹³⁷ [164] GEANT4, S. Agostinelli *et al.*, Nucl. Instrum. Meth. **A506**, 250 (2003).
- ²¹³⁸ [165] R. Brun, F. Bruyant, M. Maire, A. C. McPherson, and P. Zanarini, (1987).
- ²¹³⁹ [166] K. Abe *et al.*, Physical Review Letters **121** (2018).
- ²¹⁴⁰ [167] K. Abe *et al.*, Physical Review D **91** (2015).
- ²¹⁴¹ [168] R. Patterson *et al.*, Nuclear Instruments and Methods in Physics Research Section A: Accelerators, Spectrometers, Detectors and Associated Equipment **608**, 206 (2009).
- ²¹⁴²
- ²¹⁴³
- ²¹⁴⁴ [169] e. a. S. Berkman, T2K Technical Note **146** (2013).
- ²¹⁴⁵ [170] e. a. A. Himmel, T2K Technical Note **219** (2015).
- ²¹⁴⁶ [171] F. a. James, (1998), CERN Program Library Long Writeups.
- ²¹⁴⁷ [172] e. a. D. Barrow, T2K Technical Note **326** (2020).
- ²¹⁴⁸ [173] A. Maghrabi, A. Aldosari, and M. Almutairi, Advances in Space Research **68**, 2941 (2021).
- ²¹⁴⁹
- ²¹⁵⁰ [174] Super-Kamiokande Collaboration, K. Abe *et al.*, Phys. Rev. D **97**, 072001 (2018), <https://link.aps.org/doi/10.1103/PhysRevD.97.072001>.
- ²¹⁵¹
- ²¹⁵² [175] Particle Data Group, J. Beringer *et al.*, Phys. Rev. D **86**, 010001 (2012).
- ²¹⁵³ [176] Y. N. and, Journal of Physics: Conference Series **888**, 012191 (2017).
- ²¹⁵⁴ [177] M. Jiang, *Study of the neutrino mass hierarchy with the atmospheric neutrino data collected in Super-Kamiokande IV*, PhD thesis, Kyoto University, 2019.
- ²¹⁵⁵
- ²¹⁵⁶ [178] P. Machado, H. Schulz, and J. Turner, Physical Review D **102** (2020).
- ²¹⁵⁷ [179] T2K Collaboration, K. Abe *et al.*, Phys. Rev. Lett. **112**, 181801 (2014).
- ²¹⁵⁸ [180] R. Wendell, *Three Flavor Oscillation Analysis of Atmospheric Neutrinos in Super-Kamiokande*, PhD thesis, University of North Carolina, 2008.
- ²¹⁵⁹
- ²¹⁶⁰ [181] R. G. Calland, A. C. Kaboth, and D. Payne, **9**, P04016 (2014).
- ²¹⁶¹ [182] R. Wendell, <http://www.phy.duke.edu/raw22/public/Prob3++/>.
- ²¹⁶² [183] F. Kallenborn, C. Hundt, S. Böser, and B. Schmidt, Computer Physics Communications **234**, 235 (2019).
- ²¹⁶³

- ²¹⁶⁴ [184] L. Warsame, MaCh3 Analysis Progress.
- ²¹⁶⁵ [185] A. M. Dziewonski and D. L. Anderson, Phys. Earth Planet. Inter. **25**, 297 (1981).
- ²¹⁶⁶ [186] S. Bourret, J. A. B. Coelho, and V. V. E. and, Journal of Physics: Conference Series **888**, 012114 (2017).
- ²¹⁶⁷
- ²¹⁶⁸ [187] C. Rott, A. Taketa, and D. Bose, Scientific Reports **5** (2015).
- ²¹⁶⁹ [188] K. Hagiwara, N. Okamura, and K. ichi Senda, Journal of High Energy Physics **2011** (2011).
- ²¹⁷⁰
- ²¹⁷¹ [189] D. Typinski, Earth Gravity, <http://www.typnet.net/Essays/EarthGravGraphics/EarthGrav.pdf>, Accessed: 24-06-2022.
- ²¹⁷²
- ²¹⁷³ [190] e. a. D. Barrow, T2K Technical Note **425** (2022).
- ²¹⁷⁴ [191] V. D. Barger, K. Whisnant, S. Pakvasa, and R. J. N. Phillips, Phys. Rev. D **22**, 2718 (1980).
- ²¹⁷⁵

²¹⁷⁶ List of Figures

²¹⁷⁷ 1.1	The cross-section of neutrinos from various natural and man-made sources as a function of neutrino energy. Taken from [22]	9
²¹⁷⁸		
²¹⁷⁹ 1.2	The solar neutrino flux as a function of neutrino energy for various fusion reactions and decay chains as predicted by the Standard Solar Model. Taken from [23].	10
²¹⁸⁰		
²¹⁸¹ 1.3	Left panel: The atmospheric neutrino flux for different neutrino flavours as a function of neutrino energy as predicted by the 2007 Honda model (“This work”) [40], the 2004 Honda model (“HKKM04”) [41], the Bartol model [39] and the FLUKA model [43]. Right panel: The ratio of the muon to electron neutrino flux as predicted by all the quoted models. Both figures taken from [40].	12
²¹⁸²		
²¹⁸³		
²¹⁸⁴		
²¹⁸⁵		
²¹⁸⁶		
²¹⁸⁷		
²¹⁸⁸ 1.4	A diagram illustrating the definition of zenith angle as used in the Super Kamiokande experiment [44].	13
²¹⁸⁹		
²¹⁹⁰ 1.5	Prediction of $\nu_e, \bar{\nu}_e, \nu_\mu, \bar{\nu}_\mu$ fluxes as a function of zenith angle as calculated by the HKKM model [42]. The left, middle and right panels represent three values of neutrino energy, 0.32GeV, 1.0GeV and 3.2GeV respectively. Predictions for other models including Bartol [39], Honda [40] and FLUKA [43] are given in [44].	14
²¹⁹¹		
²¹⁹²		
²¹⁹³		
²¹⁹⁴		
²¹⁹⁵ 1.6	Constraints on the atmospheric oscillation parameters, $\sin^2(\theta_{23})$ and Δm_{23}^2 , from atmospheric and long baseline experiments: SK [49], T2K [50], NO ν A [51], IceCube [52] and MINOS [53]. Figure taken from [54].	15
²¹⁹⁶		
²¹⁹⁷		
²¹⁹⁸ 1.7	Reactor electron antineutrino fluxes for ^{235}U (Black), ^{238}U (Green), ^{239}Pu (Purple), and ^{241}Pu (Orange) isotopes. The inverse β -decay cross-section (Blue) and corresponding measurable neutrino spectrum (Red) are also given. Top panel: Schematic of Inverse β -decay interaction including the eventual capture of the emitted neutron. This capture emits a γ -ray which provides a second signal of the event. Taken from [66].	18
²¹⁹⁹		
²²⁰⁰		
²²⁰¹		
²²⁰²		
²²⁰³		
2.1	A schematic diagram of the Super-Kamiokande Detector. Taken from [80].	22
²²⁰⁴		

2205 2.2	The location of “standard PMTs” (red) inside the SK detector. Taken from [78].	26
2206		
2207 2.3	Schematic view of the data flow through the data acquisition and online system. Taken from [93].	29
2208		
2209 2.4	The cross-section view of the Tokai to Kamioka experiment illustrating the beam generation facility at J-PARC, the near detector situated at a baseline of 280m and the Super Kamiokande far detector situated 295km from the beam target.	32
2210		
2211		
2212		
2213 2.5	The near detector suite for the T2K experiment showing the ND280 and INGRID detectors. The distance between the detectors and the beam target is 280m.	33
2214		
2215		
2216 2.6	Top panel: Bird’s eye view of the most relevant part of primary and secondary beamline used within the T2K experiment. The primary beamline is the main-ring proton synchrotron, kicker magnet, and graphite target. The secondary beamline consists of the three focusing horns, decay volume, and beam dump. Figure taken from [107]. Bottom panel: The side-view of the secondary beamline including the focusing horns, beam dump and neutrino detectors. Figure taken from [108].	35
2217		
2218		
2219		
2220		
2221		
2222		
2223 2.7	The Monte Carlo prediction of the energy spectrum for each flavour of neutrino (ν_e , $\bar{\nu}_e$, ν_μ and $\bar{\nu}_\mu$) in the neutrino dominated beam FHC mode (Left) and antineutrino dominated beam RHC mode (Right) expected at SK. Taken from [109].	36
2224		
2225		
2226		
2227 2.8	Top panel: T2K muon neutrino disappearance probability as a function of neutrino energy. Middle panel: T2K electron neutrino appearance probability as a function of neutrino energy. Bottom panel: The neutrino flux distribution for three different off-axis angles (Arbitrary units) as a function of neutrino energy.	38
2228		
2229		
2230		
2231		
2232 2.9	The components of the ND280 detector. The neutrino beam travels from left to right. Taken from [107].	39
2233		
2234 2.10	Comparison of data to Monte Carlo prediction of integrated deposited energy as a function of track length for particles that stopped in FGD1. Taken from [112].	41
2235		
2236		

2237	2.11 Schematic design of a Time Projection Chamber detector. Taken from [113].	42
2238	2.12 The distribution of energy loss as a function of reconstructed momentum for charged particles passing through the TPC, comparing data to Monte Carlo prediction. Taken from [113].	42
2240		
2241	2.13 A schematic of the P0D side-view. Taken from [114].	44
2242	2.14 Left panel: The Interactive Neutrino GRID on-axis Detector. 14 modules are arranged in a cross-shape configuration, with the center modules being directly aligned with the on-axis beam. Right panel: The layout of a single module of the INGRID detector. Both figures are recreated from [107].	46
2243		
2244		
2245		
2246		
2247	3.1 Example of using Monte Carlo techniques to find the area under the blue line. The gradient and intercept of the line are 0.4 and 1.0 respectively. The area found to be under the curve using one thousand samples is 29.9 units.	51
2248		
2249		
2250		
2251	3.2 The area under a line of gradient 0.4 and intercept 1.0 for the range $0 \leq x \leq 10$ as calculated using Monte Carlo techniques as a function of the number of samples used in each repetition. The analytical solution to the area is 30 units as given by the red line.	52
2252		
2253		
2254		
2255	3.3 Three MCMC chains, each with a stationary distribution equal to a Gaussian centered at 0 and width 1 (As indicated by the black dotted lines). All of the chains use a Gaussian proposal function but have different widths (or ‘step size σ ’). The top panel has $\sigma = 0.1$, middle panel has $\sigma = 0.5$ and the bottom panel has $\sigma = 5.0$.	57
2256		
2257		
2258		
2259		
2260	3.4 The log-likelihood from the fit detailed in DB: Link to AsimovA Sensitivity Section as a function of the number of steps accumulated in each fit. Many independent MCMC chains were run in parallel and overlaid on this plot. The red line indicates the 1×10^5 step burn-in period after which the log-likelihood becomes stable.	58
2261		
2262		
2263		
2264		

2265 3.5	Left: The two dimensional probability distribution for two correlated parameters x and y . The red distribution shows the two dimensional probability distribution when $0 \leq x \leq 5$. Right: The marginalised probability distribution for the y parameter found when requiring the x to be bound between $-5 \leq x \leq 5$ and $0 \leq x \leq 5$ for the black and red distribution, respectively.	61
2271 4.1	The NEUT prediction of the ν_μ -H ₂ O cross-section overlaid on the T2K ν_μ flux. The charged current (black, solid) and neutral current (black, dashed) inclusive, charged current quasi-elastic (blue, solid), charged current 2p2h (blue, dashed), charged current single pion production (pink), and charged current multi- π and DIS (Purple) cross-sections are illustrated. Taken from [148].	67
2277 4.2	Illustration of the various processes which a pion can undergo before exiting the nucleus. Taken from [162].	69
2279 4.3	Event displays from Super Kamiokande illustrating the “crisp” ring from a muon and the typically “fuzzier” electron ring. Each pixel represents a PMT and the color scheme denotes the accumulated charge deposited on that PMT. Figures taken from [170].	71
2283 4.4	The electron/muon PID separation parameter for all sub-GeV single-ring events in SK-IV. The charged current (CC) component is broken down in four flavours of neutrino ($\nu_\mu, \bar{\nu}_\mu, \nu_e$ and $\bar{\nu}e$). Events with positive values of the parameter are determined to be electron-like.	75
2287 4.5	The variation of the measured dark rate as a function of date, broken down by PMT type. The SK-IV and SK-V periods span September 2008 to May 2018 and January 2019 to July 2020 respectively. The break in measurement between 2018 corresponds to the period of tank repair and refurbishment. Figure adapted from [172].	77
2292 4.6	Comparison of the measured raw charge deposited per event from the stopping muon data samples between SK-IV (Blue) and SK-V (Red), split by the primary muon subevent and the associated decay electron subevent.	78

2296	4.7	The distribution of the reconstructed momentum from the muon ring divided by the distance between the reconstructed muon and decay electron vertices as found in the stopping muon data sets of SK-IV (Black) and SK-IV (Red). Only events with one tagged decay electron and considered. A Gaussian fit is considered in the range [2.0, 2.4] MeV/cm and illustrated as the solid curve.	79
2297			
2298			
2299			
2300			
2301			
2302	4.8	The χ^2 difference between the SK-IV and SK-V reconstructed muon momentum divided by range when the SK-V is modified by the scaling parameter α . Both additive (Blue) and multiplicative (Black) scaling factors have been considered. In practice, the additive scaling factor actually uses the value of $(\alpha - 1.0)$	80
2303			
2304			
2305			
2306			
2307	4.9	A depiction of the topology patterns for fully-contained (FC), partially-contained (PC) and up-going muon (Up- μ) samples included in this analysis.	81
2308			
2309			
2310	4.10	The predicted neutrino flux of the fully contained (FC) sub-GeV and multi-GeV, partially contained (PC) and upward-going muon (Up- μ) events. The prediction is broken down by the $\nu_x \rightarrow \nu_e$ prediction (top left), $\nu_x \rightarrow \nu_\mu$ prediction (top right) and $\nu_x \rightarrow \nu_\tau$ prediction (bottom). All systematic dials are set to their nominal values and the Asimov A oscillation parameters are assumed.	83
2311			
2312			
2313			
2314			
2315			
2316	5.1	An “Oscillogram” that depicts the $P(\nu_\mu \rightarrow \nu_e)$ oscillation probability as a function of neutrino energy and cosine of the zenith angle. The zenith angle is defined such that $\cos(\theta_Z) = 1.0$ represents neutrinos that travel from directly above the detector. The four-layer constant density PREM model approximation is used and Asimov A oscillation parameters are assumed.	87
2317			
2318			
2319			
2320			
2321			
2322	5.2	The effect of δ_{CP} for atmospheric neutrinos given in terms of the neutrino energy and zenith angle. The oscillogram compares the $P(\nu_\mu \rightarrow \nu_e)$ oscillation probability for a CP conserving ($\delta_{CP} = 0.0$) and CP violating ($\delta_{CP} = -1.601$) value of δ_{CP} . The other oscillation parameters assume the “Asimov A” oscillation parameter set given in Table 5.1.	89
2323			
2324			
2325			
2326			

2327 5.3 An illustration of the matter-induced effects on the oscillation probability, given as a function of neutrino energy and zenith angle. The top row 2328 of panels gives the $P(\nu_e \rightarrow \nu_e)$ oscillation probability and the bottom 2329 row illustrates the $P(\bar{\nu}_e \rightarrow \bar{\nu}_e)$ oscillation probability. The left column 2330 highlights the oscillation probability in a vacuum, whereas the middle 2331 and right column represents the oscillation probabilities when the four 2332 layer fixed density PREM model is assumed. All oscillation probabilities 2333 assume the “Asimov A” set given in Table 5.1, but importantly, the right 2334 column sets an inverted mass hierarchy. The “matter resonance” effects 2335 at $E_\nu \sim 5\text{GeV}$ can be seen in the $P(\nu_e \rightarrow \nu_e)$ for normal mass hierarchy 2336 and $P(\bar{\nu}_e \rightarrow \bar{\nu}_e)$ for inverted hierarchy.	90
2338 5.4 The oscillation probability for beam neutrino events given as a function 2339 of neutrino energy. All oscillation parameters assume the “Asimov A” 2340 set given in Table 5.1 unless otherwise stated. Each panel represents a 2341 change in one of the oscillation parameters whilst keeping the remaining 2342 parameters fixed.	91
2343 5.5 The number of electron-like events in the FHC and RHC operating 2344 mode of the beam, as a function of the oscillation probabilities. Both 2345 normal hierarchy (Solid) and inverse hierarchy (Dashed) values of 2346 Δm_{23}^2 are given.	92
2347 5.6 The oscillation probability $P(\nu_\mu \rightarrow \nu_e)$, given as a function of neutrino 2348 energy and zenith angle, which highlights an example of the “fast” 2349 oscillations in the sub-GeV upgoing region.	94
2350 5.7 Illustration of the averaging procedure for $N = 2$. The oscillation 2351 probabilities calculated on the finer left binning are averaged to obtain 2352 the oscillation probabilities in the coarser right binning. These averaged 2353 oscillation probabilities with the coarser binning are then applied to 2354 each event during the fit.	96
2355 5.8 Event rate of the SubGeV_elike_0dcy sample as a function of the num- 2356 ber of sub-divisions per coarse bin. Each subplot represents the event 2357 rate of the sample at a different oscillation parameter set (thrown from 2358 the PDG priors). The red line in each subplot represents the mean of the 2359 event rate over the different values of sub-divisions for that particular 2360 oscillation parameter throw.	98

2361	5.9	Variance of event rate for each atmospheric sample as a function of the number of sub-divisions per coarse bin. The solid red line indicates the 0.1% threshold and the dashed red line is a graphical indication of the variance at a sub-division $N = 10$	99
2362			
2363			
2364			
2365	5.10	Variance of sample likelihood, when compared to ‘Asimov data’ set at Asimov A, for each atmospheric sample as a function of the number of sub-divisions per coarse bin. The solid red line indicates the 0.1% threshold and the dashed red line is a graphical indication of the variance at a sub-division $N = 10$	100
2366			
2367			
2368			
2369			
2370	5.11	The oscillation probability, $P(\nu_\mu \rightarrow \nu_e)$ (top row) and $P(\nu_e \rightarrow \nu_e)$ (bottom row), given as a function of neutrino energy and zenith angle. The left column gives the “fine” binning used to calculate the oscillation probabilities and the right column illustrates the “coarse” binning used to reweight the MC events. The fine binning choice is given with $N = 10$, which was determined to be below threshold from Figure 5.9 and Figure 5.10.	101
2371			
2372			
2373			
2374			
2375			
2376			
2377	5.12	The calculation time taken to both calculate the oscillation probabilities and fill the “coarse” oscillograms, following the technique given in section 5.2, for the CUDAProb3 and ProbGPU (Red) calculation engines. CUDAProb3 has both a GPU (Blue) and CPU (Black) implementation, where the CPU implementation is multithreaded. Therefore, 8-threads (solid) and 40-threads (dashed) configurations have been used. Prob3, which is a CPU single-thread implementation has a mean step time of 1.142s.	103
2378			
2379			
2380			
2381			
2382			
2383			
2384			
2385	5.13	The density of the Earth given as a function of the radius, as given by the PREM model (Black) and the constant density four-layer approximation (Blue), as used in the official SK-only analysis.	104
2386			
2387			

2388 5.14 The oscillation probability, $P(\nu_\mu \rightarrow \nu_e)$ (top row) and $P(\nu_e \rightarrow \nu_e)$ (bot-	106
2389 tom row), given as a function of neutrino energy and zenith angle.	
2390 The left column gives probabilities where the constant $Z/A = 0.5$	
2391 approximation which is used in the official SK-only analysis. The mid-	
2392 dle column gives the probabilities where the more accurate $Z/A =$	
2393 $[0.468, 0.498]$ values as given in Table 5.2. The right column illustrates	
2394 the difference in oscillation probability between the two different tech-	
2395 niques.	
2396 5.15 The density of the Earth given as a function of the radius, as given by	107
2397 the PREM model (Black), the constant density four-layer approxima-	
2398 tion (Blue), as used in the official SK-only analysis, and the quadratic	
2399 approximation of the PREM model (Red).	
2400 5.16 The oscillation probability, $P(\nu_\mu \rightarrow \nu_e)$ (top row) and $P(\nu_e \rightarrow \nu_e)$ (bot-	109
2401 tom row), given as a function of neutrino energy and zenith angle. The	
2402 left column gives probabilities where the four-layer constant density ap-	
2403 proximation is used. The middle column gives the probabilities where	
2404 the density is integrated over the trajectory, using the quadratic PREM	
2405 approximation, for each $\cos(\theta_Z)$ is used. The right column illustrates the	
2406 difference in oscillation probability between the two different techniques.	
2407 5.17 The oscillation probability, $P(\nu_\mu \rightarrow \nu_e)$ (top row) and $P(\nu_e \rightarrow \nu_e)$ (bot-	113
2408 tom row), given as a function of neutrino energy and zenith angle. The	
2409 left column gives probabilities where a fixed production height of 25km	
2410 is used. The middle column gives the probabilities where the produc-	
2411 tion height is analytically averaged. The right column illustrates the	
2412 difference in oscillation probability between the two different techniques.	

List of Tables

2414	2.1	The various SK periods and respective live-time. The SK-VI live-time is calculated until 1 st April 2022. SK-VII started during the writing of this thesis.	21
2417	2.2	The trigger thresholds and extended time windows saved around an event which were utilised throughout the SK-IV period. The exact thresholds can change and the values listed here represent the thresh- olds at the start and end of the SK-IV period.	30
2421	2.3	The threshold momentum and energy for a particle to generate Cherenkov light in ultrapure water, as calculated in Equation 2.2 in ultrapure water which has refractive index $n = 1.33$	31
2424	3.1	Jeffreys scale for strength of preference for two models A and B as a function of the calculated Bayes factor ($B_{AB} = B(A/B)$) between the two models [130]. The original scale is given in terms of $\log_{10}(B(A/B))$ but converted to linear scale for easy comparison throughout this thesis.	63
2428	5.1	Reference values of the neutrino oscillation parameters for two different oscillation parameter sets.	92
2430	5.2	Description of the four layers of the Earth invoked within the average constant density approximation of the PREM model [185].	104
2432	5.3	The quadratic polynomial fits to the PREM model for four assumed layers of the PREM model. The fit to calculate the coefficients is given in [190], where $x = R/R_{Earth}$	107